INTEGRATING ION IRRADIATION AND FINITE ELEMENT ANALYSIS TO UNRAVEL SWELLING-INDUCED RISKS IN CR-COATED CLADDING

A Thesis

by

ARTUR SANTOS PAIXAO

Submitted to the Graduate and Professional School of
Texas A&M University
in partial fulfillment of the requirements for the degree of

MASTER OF SCIENCE

Chair of Committee, Lin Shao

Committee Members, Karim Ahmed

Kelvin Xie

Head of Department, Michael Nastasi

June 2025

Major Subject: Nuclear Engineering

ABSTRACT

Chromium-coated Zircaloy claddings have emerged as a promising accident-tolerant fuel (ATF) design to improve the high-temperature oxidation resistance of nuclear fuel rods, particularly under loss-of-coolant accident (LOCA) scenarios. Chromium's ability to form a stable, protective oxide layer and its low neutron absorption cross-section make it an attractive candidate for short-term evolutionary ATF solutions. However, under extended operation and irradiation, chromium exhibits degradation mechanisms such as interdiffusion with Zircaloy, void swelling, and the formation of brittle intermetallic layers, which can compromise mechanical integrity and nuclear safety margins. This thesis integrates ion irradiation experiments and finite element analysis (FEA) to evaluate the impact of irradiation-induced swelling and creep on the structural performance of Cr-coated claddings. Swelling data from ion-irradiated Cr samples at Accelerator Laboratory Texas A&M are used as input for simulations that assess stress evolution under typical reactor operating and refueling conditions. Results show that swelling significantly increases interfacial stress, while irradiation creep partially offsets this buildup during steady-state operation. However, during reactor cooldown, when creep is ineffective, the accumulated misfit strains cause sharp tensile stress surges, raising the likelihood of coating delamination and cracking. These findings highlight critical irradiation effects often overlooked in current safety assessments and demonstrate that ignoring swelling and creep may lead to underpredicted failure risks in ATF designs. The developed methodology can be extended to other coated systems to inform regulatory evaluations and guide safer reactor design.

DEDICATION

This work is dedicated to God for granting life, health, and the strength to carry on each day.

To my beloved mother, my ultimate source of strength, whose constant prayers and love have always supported me.

To family and friends, whose acceptance, encouragement, and belief have been a steady source of motivation.

If this goal was achieved, it was because of them. May it serve as an example to inspire those I love to keep moving forward.

ACKNOWLEDGMENTS

I would like to express my sincere gratitude to those who contributed to the completion of this research. I extend my appreciation to Dr. Lin Shao for his collaborative and excellent guidance on the conduct of this study. Additionally, I acknowledge former and current students from our laboratory, the Accelerator Laboratory at Texas A&M, for their foundational studies, which served as the basis for this work. Special thanks also go to Dr. Frank Garner, who provided critical insights, recommendations, and valuable tutoring throughout the process of this work.

CONTRIBUTORS AND FUNDING SOURCES

Contributors

This work was supported by a thesis committee consisting of Professor Lin Shao (advisor), Professor Karim Ahmed, both from the Department of Nuclear Engineering, and Professor Kelvin Xie of the Department of Materials Science and Engineering.

Funding Sources

The Brazilian Navy fully supported this graduate program, following the terms of the Memorandum of Agreement for Academic and Research Collaboration between the Brazilian Navy and Texas A&M University.

NOMENCLATURE

AOOs	Antecipated Operational Occurrences
APF	Atomic Packing Factor
ATF	Accident-Tolerant Fuel
BCC	Body-centered Cubic
BDBA	Beyond Design Basis Accident
DBA	Design Basis Accident
dpa	Displacements per Atom
ECCS	Emergency Core Cooling System
EOL	End of Life
FCC	Face-Centered Cubic
FEA	Finite Element Analysis
FIB	Focused Ion Beam
HCP	Hexagonal Close-Packed
LOCA	Loss of Coolant Accident
LWR	Light-Water Reactor
MD	Molecular Dynamics
NEA	Nuclear Energy Agency
NRC	Nuclear Regulatory Commission
PAG	Preferential Absorption Glide
PD	Point Defect
PKA	Primary Knock-on Atom
PWR	Pressurized-Water Reactor

SAFDLs	Specified Acceptable Fuel Design Limits
SIA	Self-interstitial Atom
SIPA	Stress-induced Preferential Absorption
SIPN	Stress-induced Preferential Nucleation
SRP	Standard Review Plan
TAMU	Texas A&M University
TBD	To be defined
TEM	Transmission Electron Microscopy

TABLE OF CONTENTS

Page

LIST OF FIGURES

FIGURE Page

LIST OF TABLES

TABLE Page

1. INTRODUCTION ON ACCIDENT-TOLERANT FUELS

1.1 The Fukushima-Daiichi accident

Traditional cladding materials, such as Zircaloy-2 and Zircaloy-4, have been used in light water reactors (LWR) due to their remarkably low neutron absorption cross-section, appropriate thermal conductivity, suitable dimensional stability, and corrosion resistance in the harsh environment of a reactor core [1]. However, at elevated temperatures, Zircaloy undergoes an exothermic reaction with steam, forming zirconium (Zr) dioxide and hydrogen.

$$\mathrm{Zr} + 2\mathrm{H_2O} \rightarrow \mathrm{ZrO_2} + 4\mathrm{H}$$

This reaction presents several safety challenges. Hydrogen absorption into the cladding promotes hydride-induced embrittlement, severely affecting its critical properties [1]; unabsorbed hydrogen accumulates as an explosive gas within the coolant system; and the reaction itself generates additional heat, accelerating the temperature rise of fuel rods.

These issues played a critical role in the Fukushima-Daiichi accident in 2011, where the loss of active cooling due to a station blackout led to high-temperature conditions. The subsequent hydrogen explosions, resulting from accumulated gas escaping containment, highlighted the limitations of Zircaloy under accident scenarios. Consequently, the event catalyzed the development of accident-tolerant fuels (ATFs) and advanced cladding materials with improved high-temperature performance [2].

1.2 The short-term evolutionary ATF solution: coated cladding

The ATF concept encompasses a suite of solutions designed to improve the performance and safety of LWR fuel under severe accident conditions, primarily by developing cladding with enhanced strength, reduced steam reactivity, and lower hydrogen and heat generation [3]. In addition to cladding improvements, efforts also focus on fuel pellet modifications, such as chemically doping UO_2 to enhance thermal conductivity and reduce fragmentation. Over time, the scope of ATF

has expanded to include initiatives aimed at lowering operational costs, including increasing uranium enrichment and extending burnup limits. An overview of current ATF design strategies is presented in Figure 1.1.

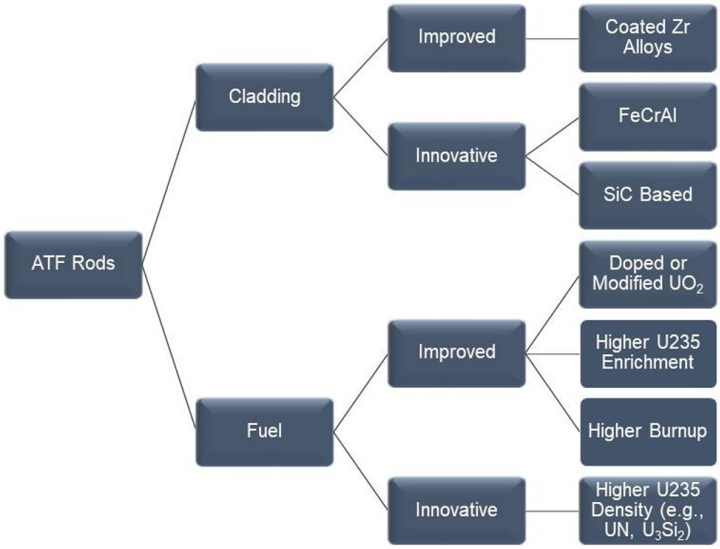

Figure 1.1: Proposed ATF solutions for current LWR fuel rods [3].

The cladding solutions are typically categorized as either (1) evolutionary enhancements to existing designs (improved), or (2) revolutionary new approaches (innovative) [3]. A key objective of ATF cladding is to improve oxidation resistance, thereby mitigating heat generation from oxidation reactions, extending operator response time, and increasing the thermal margins of the Emergency Core Cooling System (ECCS), as shown in Figure 1.2.

In the short term, the ATF development has focused on applying thin protective coatings to conventional cladding. These coatings act as barriers against steam oxidation without altering the underlying cladding structure. To be effective, the coating must exhibit chemical stability in high-temperature steam environments, particularly during loss-of-coolant accidents (LOCA), by limiting oxygen and hydroxide diffusion into the Zircaloy substrate. Additionally, the material must withstand thermal shock from coolant reinjection while maintaining compatibility with ex-

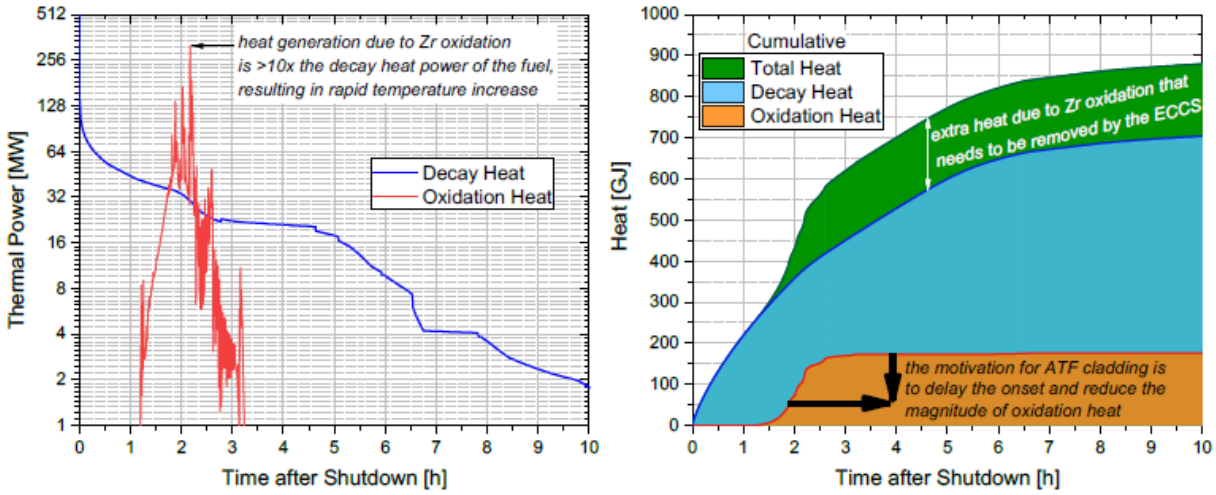

Figure 1.2: Thermal power and cumulative energy due to decay heat of radioactive nuclides and Zr-based cladding oxidation during a station blackout [4].

isting fuel performance, reactor design, and water chemistry.

1.3 Pure Chromium as a coating

Since the Fukushima-Daiichi accident, a variety of materials, including pure metals, carbides, MAX phases, and alloys—have been investigated as protective coatings for cladding under high-temperature oxidizing conditions. A common feature among these candidates is the inclusion of chromium (Cr), silicon (Si), or aluminum (Al), elements known to form stable and protective oxide layers at elevated temperatures. Representative materials include SiC, FeCrAl, CrN, Cr, Cr_2AlC, and Ti_2AlC. However, experimental studies have identified several challenges when using these materials, such as: (1) chemical instability in steam, (2) susceptibility to cracking from thermal shocks and high temperatures, and (3) low eutectic temperatures, which may fall below those encountered during LOCA [5].

Among the proposed materials, Cr has emerged as a leading candidate due to its ability to form a protective barrier that significantly reduces oxidation rates and enhances the mechanical strength and durability of the cladding [5]. Also, Cr has proven to be the most viable solution due to its exceptional stability, adhesion properties, and ability to form a compact protective layer. Addition-

ally, it exhibits a relatively low neutron absorption cross-section, good mechanical properties, and a stable interlayer phase at LOCA temperatures while improving zirconium alloy wettability.

Numerous out-of-pile tests have been conducted to evaluate the performance of Cr-coated cladding as a short-term and evolutionary approach to improving cladding safety. These studies primarily focused on oxidation resistance, interdiffusion, microstructural behavior, and mechanical response [5].

However, there remains a critical need to investigate the irradiation effects on Cr when bonded to a zircaloy substrate, as current understanding of this interface remains limited. As a surrogate for in-pile tests, ion irradiation has been widely used for neutron irradiation due to its lower cost and higher damage rate [6–8]. Results from ion beam studies offer a much faster means of evaluating irradiation damage, and when coupled with computational modeling, can support safety-related conclusions that are essential for both the licensing and deployment phases of Cr as a coating for zircaloy claddings.

1.4 Scope of the present thesis

The central objective of this thesis is to integrate ion irradiation data with finite element modeling to support risk-informed evaluations of Cr-coated Zircaloy fuel cladding performance under realistic LWR operating conditions. In addition, the work provides essential background on safety-related concerns associated with Cr-coated cladding and highlights the role of ion irradiation in accelerating the deployment of ATF designs. The study is structured into three main chapters, each addressing a critical aspect of this integrated approach, as outlined below.

Chapter 2 examines the key degradation mechanisms that may impact the performance of Cr-coated Zircaloy cladding under both normal and accident scenarios in LWRs. It reviews current safety evaluations from the U.S. Nuclear Regulatory Commission (NRC), emphasizing the limited understanding of irradiation effects on Cr-coated systems. The chapter underscores the importance of ion irradiation as a strategic tool to support the accelerated deployment of this advanced fuel cladding technology, which is in line with the NRC's fast-track licensing timeline. Particular attention is given to how irradiation-induced damage could create unfavorable initial conditions

for the coating at the onset of an accident, potentially compromising its protective role.

Chapter three reviews the fundamental concepts governing cavity swelling in irradiated materials and explores its correlation with irradiation creep, emphasizing their synergistic impact on material performance in nuclear environments. It discusses how ion irradiation can replicate key features of neutron-induced damage, offering a reliable and accelerated pathway for evaluating radiation tolerance in structural materials. A systematic procedure for assessing void swelling via ion irradiation is outlined, followed by a detailed presentation of experimental results for pure chromium obtained at the Texas A&M University (TAMU) Accelerator Laboratory. These results are analyzed to understand their implications for Cr coating behavior under reactor operating conditions, particularly regarding dimensional stability and mechanical reliability.

Chapter four presents the development of a finite element analysis (FEA) model of Cr-coated zircaloy cladding under pressurized water reactor (PWR) conditions, incorporating radiation-induced dimensional changes derived from ion irradiation experiments conducted at TAMU's Accelerator Laboratory. The model is employed to simulate stress evolution in the coated system during normal reactor operation, focusing on three primary objectives: assessing the impact of irradiation-driven deformation on the coating–cladding interface, identifying conditions that may lead to interfacial debonding or fracture, and validating the feasibility of integrating experimental irradiation data with FEA simulations for risk-informed performance assessments. This integrated approach aims to provide predictive insights into the structural stability of accident-tolerant fuel coatings under long-term irradiation.

1.5 References

[1] S. Suman, M. K. Khan, M. Pathak, R. N. Singh, and J. K. Chakravartty, "Hydrogen in zircaloy: Mechanism and its impacts," *International Journal of Hydrogen Energy*, vol. 40, pp. 5976–5994, 5 2015.

[2] United States Nuclear Regulatory Commission (NRC), "Origins of accident tolerant fuel," https://www.nrc.gov/reactors/power/atf/roadmap/origins.html, June 13, 2024, accessed: June

28, 2024.

[3] R. B. Rebak, "Improved and innovative accident-tolerant nuclear fuel materials considered for retrofitting light water reactors—a review," *Corrosion and Materials Degradation*, vol. 4, pp. 466–487, 2023. [Online]. Available: https://www.mdpi.com/2624-5558/4/3/24

[4] K. A. Terrani, "Accident tolerant fuel cladding development: Promise, status, and challenges," *Journal of Nuclear Materials*, vol. 501, pp. 13–30, 2018.

[5] J. Yang, M. Steinbrück, C. Tang, M. Große, J. Liu, J. Zhang, D. Yun, and S. Wang, "Review on chromium coated zirconium alloy accident tolerant fuel cladding," *Journal of Alloys and Compounds*, vol. 895, p. 162450, 2022.

[6] S. J. Zinkle and L. L. Snead, "Opportunities and limitations for ion beams in radiation effects studies: Bridging critical gaps between charged particle and neutron irradiations," *Scripta Materialia*, vol. 143, pp. 154–160, 1 2018.

[7] G. S. Was, Z. Jiao, E. Getto, K. Sun, A. M. Monterrosa, S. A. Maloy, O. Anderoglu, B. H. Sencer, and M. Hackett, "Emulation of reactor irradiation damage using ion beams," *Scripta Materialia*, vol. 88, pp. 33–36, 10 2014.

[8] L. Shao, J. Gigax, D. Chen, H. Kim, F. A. Garner, J. Wang, and M. B. Toloczko, "Standardization of accelerator irradiation procedures for simulation of neutron induced damage in reactor structural materials," *Nuclear Instruments and Methods in Physics Research Section B: Beam Interactions with Materials and Atoms*, vol. 409, pp. 251–254, 10 2017.

2. DEGRADATION MECHANISMS AND SAFETY CONSIDERATIONS OF CHROMIUM-COATED CLADDING UNDER EXTREME CONDITIONS

2.1 Introduction

Chromium has demonstrated superior performance compared to other candidate materials proposed for ATF coating applications. However, it is not without limitations. Chromium coatings exhibit various degradation mechanisms and failure modes that can compromise their protective function, particularly in high-temperature steam environments. Despite these challenges, the nuclear industry and the Nuclear Regulatory Commission (NRC) have undertaken assertive efforts to make Cr-coated cladding the first ATF design to achieve regulatory approval. A comprehensive roadmap, currently available on the NRC website [1], outlines the targeted studies and regulatory steps needed to support license amendment approvals by 2027. To meet this goal, the NRC has adopted a structured development strategy for Cr-coated cladding, as illustrated in Figure 2.1.

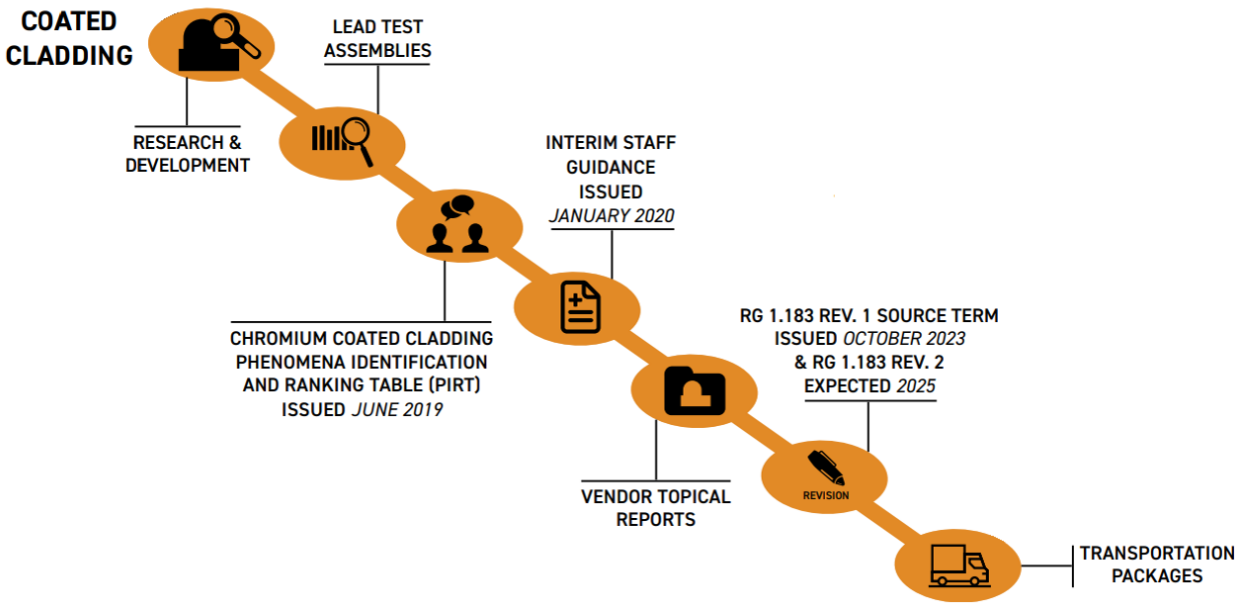

Figure 2.1: Current development process adopted by NRC to accept Cr-coated cladding design employing an amendment in the current LWR license frameworks [1].

Several research and development (R&D) efforts have been conducted to assess the integrity of chromium (Cr) coatings under high-temperature steam conditions [2]. These investigations formed the foundation for two key documents: a Phenomena Identification and Ranking Table (PIRT) report [3] and an Interim Staff Guidance document [4] supplementing the Standard Review Plan (SRP) NUREG-0800 (Figure 2.1). The PIRT identifies potential failure modes of Cr coatings and outlines associated changes to design parameters relative to bare cladding. The Interim Guidance builds upon these findings to update the SRP's SAFDLs and to propose new evaluation criteria or studies where needed.

On the other hand, even before issuing these regulatory documents, fuel vendors and nuclear power plant operators initiated in-reactor testing of Cr-coated fuel assemblies under commercial operating conditions. These efforts culminated in the submission of vendor topical reports that remain under review. It is important to note that, at that time, the effects of irradiation on Cr coating integrity and performance were not yet fully understood. Nevertheless, a recognized need was to evaluate the new design under representative reactor conditions. This reflects the accelerated effort to deploy more accident-tolerant fuel rod designs but also highlights an existing gap in the systematic evaluation of irradiation effects, originated either from the inherent complexity of integrating irradiation tests with non-nuclear qualification methods, or from the long durations required for in-reactor exposure, which the Cr coating development timeline could not afford to wait for.

This chapter provides a comprehensive overview of safety-relevant issues associated with Cr-coated cladding, informed by the regulatory and technical documents previously discussed. It begins by identifying known degradation mechanisms and performance attributes of the coating, with emphasis on their implications for LWR safety requirements and aspects. The chapter concludes by identifying critical irradiation damage effects that remain insufficiently explored but could influence the long-term integrity and safety margins of Cr-coated fuel systems.

2.2 Performance and degradation mechanisms under reactor conditions

2.2.1 The oxidation protective function

According to the review on Cr coatings by Yang et al. [2], chromium exhibits excellent oxidation resistance under typical LWR conditions by forming a protective oxide (Cr_2O_3) layer called chromia. Under high-temperature steam exposure, the initial performance remains robust, following the main reactions below:

$$\mathrm{Cr(s)} + \frac{3}{4}\mathrm{O_2(g)} \rightarrow \frac{1}{2}\mathrm{Cr_2O_3(s)} \tag{2.1}$$

$$2\mathrm{Cr(s)} + 3\mathrm{H_2O(g)} \rightarrow \mathrm{Cr_2O_3(s)} + 3\mathrm{H_2(g)} \tag{2.2}$$

$$\frac{1}{2}\mathrm{Cr_2O_3(s)} + \mathrm{H_2O(g)} + \frac{3}{4}\mathrm{O_2(g)} \rightarrow \mathrm{CrO_2(OH)_2(g)} \tag{2.3}$$

$$\frac{1}{2}\mathrm{Cr_2O_3(s)} + \frac{1}{2}\mathrm{H_2O(g)} + \frac{1}{2}\mathrm{O_2(g)} \rightarrow \mathrm{CrO_2(OH)(g)} \tag{2.4}$$

However, the protective capability of the coating degrades over time due to microstructural changes in the coating–cladding system (Figure 2.2). The primary mechanisms responsible for this degradation include: (1) accelerated Cr diffusion into the substrate, which increases the consumption rate of the Cr layer; (2) growth of a brittle intermetallic $ZrCr_2$ phase at the coating–cladding interface; and (3) enhanced diffusion of oxidizing species through Cr_2O_3 caused by an increase of volatilization reactions (Eqs. 2.3 and 2.4). A representative microstructure of this degraded interface under high-temperature steam conditions is presented in Figure 2.3a.

Additionally, high-temperature steam experiments and electron microscopy have revealed ZrO_2 (zirconia) stringer formation along Cr grain boundaries, driven by inward Zr diffusion and oxidizing species that overcome the chromia layer. A leading explanation for the premature failure of the Cr coating is that these growing stringers coalesce into an intergranular network (Figure 2.2b), facilitating oxygen anion transport and compromising the coating's protective function before complete Cr consumption. Therefore, the coating can lose its protective function even if the residual

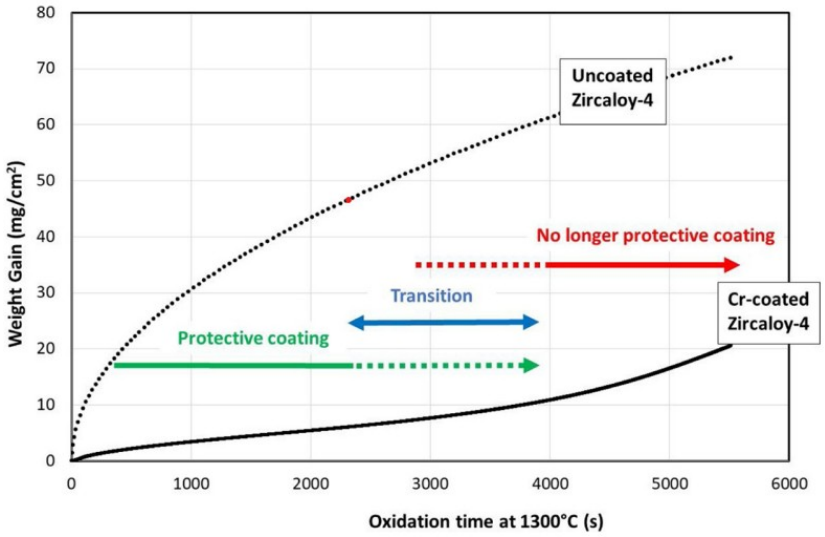

Figure 2.2: Cumulative oxidation (weight gain) for Cr-coated and bare zircalloy claddings during a high-temperature steam test showing the transition to a loss-of-resistance stage [5].

coating remains.

The primary degradation mechanisms of Cr-coated cladding are intrinsically linked to the Cr–Zr binary system. Due to the significant atomic size mismatch between Cr and Zr, the two elements cannot form an isomorphous solid solution. At low temperatures, their mutual solubility is limited. However, at elevated temperatures, such as those encountered during a LOCA, zirconium changes from the α phase, a hexagonal close-packed (HCP) structure, to the β phase with a body-centered cubic (BCC) organization. Then, Cr becomes significantly more soluble in β-Zr, as illustrated in Figure 2.4. During a LOCA event (temperature < 1200 °C), the high interdiffusion rate of Cr into Zircaloy-4, approximately 5.5×10^{-12} m^2/s [6], accelerates the consumption of the Cr layer into the substrate.

As shown in Figure 2.4, the Cr–Zr eutectic temperature is approximately 1332 °C. In a beyond-design-basis accident (BDBA), temperatures may exceed this threshold, initiating the eutectic reaction between chromium and zirconium. This reaction leads to the complete loss of the coating's protective properties, as confirmed by experimental observations [2].

The precise duration for which chromium coatings can reliably maintain their oxidation re-

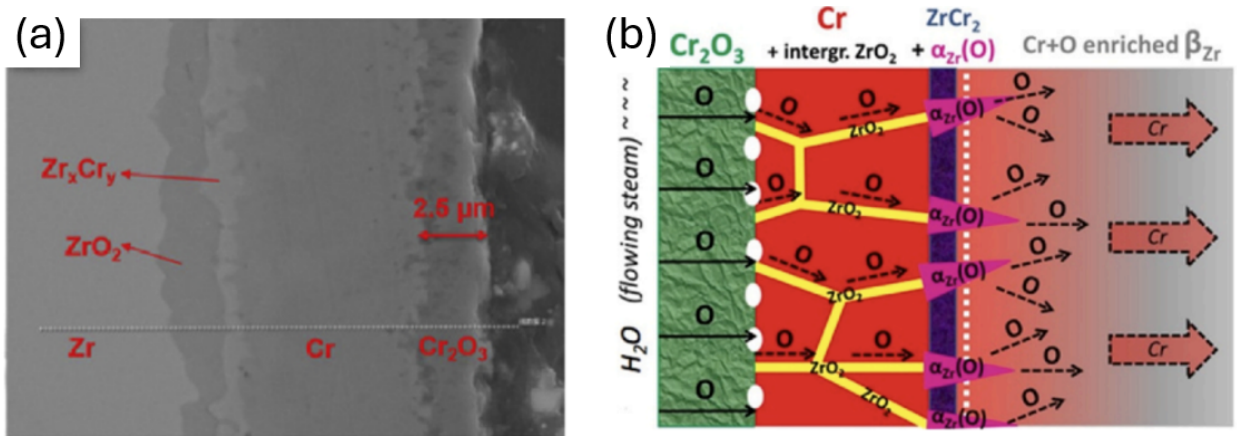

Figure 2.3: (a) Coated cladding microstructure after oxidation at 1200 °C for 30 min with (b) associated illustration of proposed degradation mechanisms. In the micrograph, from left to right, the system is formed by layers of Zr, zirconia (ZrO_2), mixed intermetallic compounds (Zr_xCr_y), Cr, and chromia (Cr_2O_3) [2].

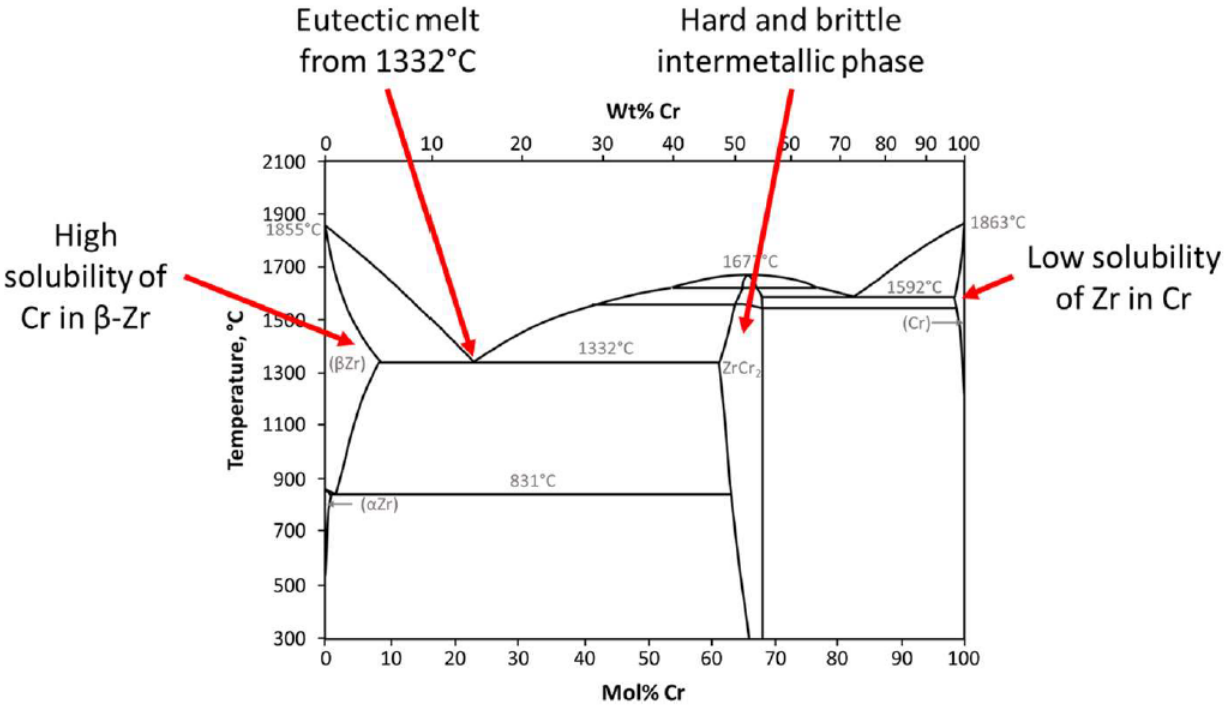

Figure 2.4: Cr-Zr binary phase diagram showing relevant degradation aspects of the system [7].

sistance under accident conditions remains uncertain. Estimations of the associated extension in accident coping time vary widely across studies. In the case of a station blackout, Wu and Shir-

van estimated a marginal improvement of only 1 to 22 minutes [8], while Feng et al. projected a considerably longer extension of 1 to 2 hours [9]. However, both assessments excluded the impact of any coating degradation mode. Some preliminary insights into degradation behavior are provided in [10]. In general, the safety benefit of the Cr coating appears limited and highly dependent on the onset of degradation. Moreover, as outlined below, additional failure modes may further compromise the coating's protective function and considerably reduce its effective survival time.

2.2.2 The mechanical response

Brittle intermetallic compounds—primarily $ZrCr_2$—form in the intermixed region between the chromium coating and the Zircaloy substrate under high-temperature conditions, as shown in Figure 2.4. From a diffusion perspective, this intermetallic layer is beneficial, as it mitigates further Cr interdiffusion into the substrate. However, under accident conditions, the coating is subjected to a harsh environment involving both high-temperature oxidation and elevated tensile stress. In a LOCA scenario, for example, tensile stresses may arise due to a relatively increased internal cladding pressure following coolant loss or thermal shocks during reflooding when cold coolant is rapidly reintroduced, potentially compromising coating integrity.

One anticipated failure mode is the cracking of the intermetallic layer, which exhibits inherently brittle behavior, as illustrated in Figure 2.5a. Existing studies have shown that $ZrCr_2$, due to its brittle nature, can readily act as a pathway for crack initiation and propagation under the combined effects of thermal stress and irradiation [11]. Moreover, the continued growth of this interfacial layer has been associated with a general embrittlement of the coated cladding structure [3].

In addition, the mismatch in volumetric expansion between the coating and substrate materials during oxidation can lead to the formation of bubbles, blisters, or voids at the Zr–Cr interface, particularly during cooldown phases or prolonged accident conditions, as illustrated in Figure 2.5. These morphological defects may result in partial or localized coating delamination, which can create a cold spot that serves as a hydrogen diffusion sink, thereby inducing local cladding embrittlement. In more severe cases, total delamination may occur, compromising the reactor's core cooling capacity and completely eliminating the protective function of the Cr coating [3].

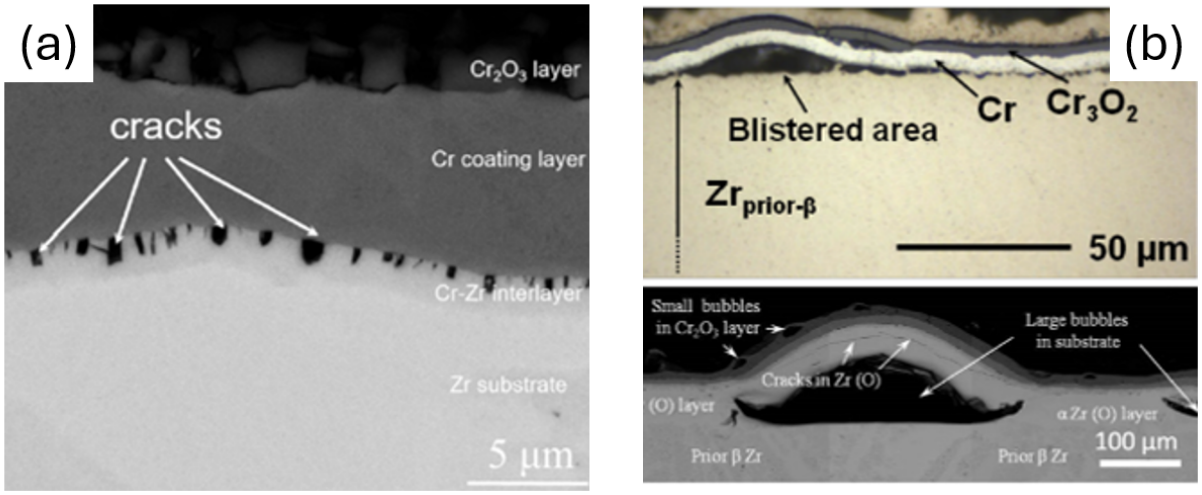

Figure 2.5: Cross-section morphology showing expected coating failure/damage modes during a LOCA and BDBA scenarios [2] during (a) tensile testing with pre-oxidized samples showing the low toughness of the intermetallic layer and (b) blisters (during temperature reversal) and bubbles (after an annealing process at 1200 °C for three hours) in between different layers.

2.2.3 Possible improvements for the Cr coating design

Although chromium (Cr) coatings have demonstrated promising performance within the framework of ATF designs, they are not yet considered the definitive solution for protecting Zircaloy cladding. As previously discussed, several degradation mechanisms highlight the need for further optimization. These include: (1) the relatively low eutectic temperature between Cr and Zircaloy, (2) the rapid consumption of the Cr layer under high-temperature conditions, (3) the brittle thermo-shock response of the intermetallic layer during coolant reinjection phases, and (4) the formation of shortcut diffusion pathways for oxygen due to outward Zr migration along Cr grain boundaries.

A proposed strategy involves the incorporation of a diffusion barrier interlayer between the Cr coating and the Zircaloy substrate, as illustrated in Figure 2.6. Molybdenum (Mo) has been considered for this role [12, 13], but its effectiveness is limited by a relatively high interdiffusion rate with Zircaloy. Alternatively, pure metals such as niobium (Nb), tantalum (Ta), and rhenium (Re) offer more favorable characteristics due to their high melting points and low diffusion coefficients in Zircaloy-4 [14]. However, their relatively high neutron reaction cross-sections present a

potential drawback for use in nuclear fuel applications. In addition to pure metals, more complex material systems—such as alloys, high-entropy alloys, and MAX phases—also warrant investigation. The ultimate objective is to identify a diffusion barrier material that can effectively prolong the integrity of the Cr coating without compromising its mechanical and corrosion resistance or introducing significant neutronic penalties.

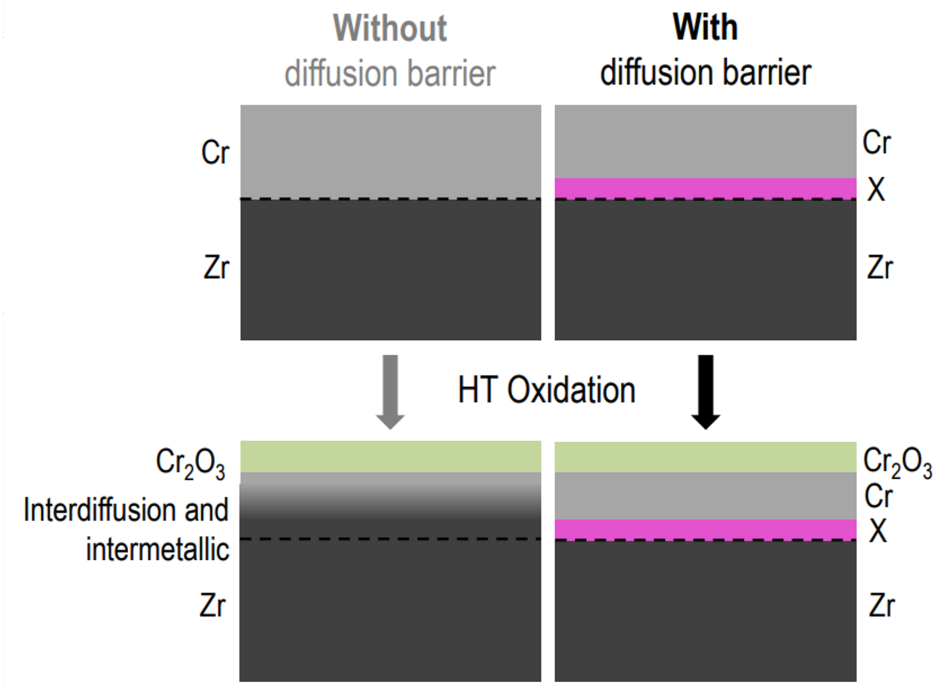

Figure 2.6: Representation of the main functional criteria for a diffusion barrier material X: to slow the coating consumption by diffusion [12].

Another proposed solution is the introduction of dopants into the Cr coating to reduce inward Cr interdiffusion and suppress the formation of intermetallic compounds. An initial investigation by Li et al. demonstrated that the addition of tin (Sn) reduced the formation of $ZrCr_2$ by approximately 10% [11]. Although the improvement is modest, the study provides a foundation for further exploration of alternative dopant elements. It is important to note that the inclusion of dopants may also alter the physical properties and irradiation response of the Cr coating, both of which require

detailed evaluation in future studies.

2.3 Safety-related impacts of Cr-coated cladding

2.3.1 Safety-related fuel limits for coated claddings

SAFDLs are limits and conditions established by the NRC that fuel pellets and cladding must satisfy to prevent fuel failure and ensure core coolability during accident scenarios. As such, they are classified as nuclear safety-related limits. Adherence to SAFDLs also mitigates the risk of fuel rod damage or failure during normal operation and anticipated operational occurrences (AOOs), thereby improving the initial condition of the cladding at the onset of AOOs and postulated accident events [4].

Due to the thin nature of the external chromium coating and its associated performance benefits, many SAFDLs applicable to bare Zircaloy cladding remain unchanged, either because the coating does not alter the original safety limits or improves the safety margins relative to those limits. However, as discussed in the previous section, the unique failure modes and degradation mechanisms associated with Cr-coated cladding are expected to affect certain SAFDLs. In addition, irradiation effects are a particular concern identified in [3] because they can lead to cracking or localized coating delamination. These phenomena should therefore be explicitly considered in the definition and revision of the SAFDL framework.

Based on the recommendations from [3] and [4], Table 2.1 summarizes the key SAFDLs relevant to conventional bare cladding that are potentially impacted by the unique failure modes and material characteristics of Cr-coated cladding. Notably, several of the Cr aspects are influenced by irradiation, as outlined in the subsequent considerations accompanying each item in the table:

- **Fretting**: Irradiation-induced hardening and embrittlement of the chromium coating may increase the risk of fretting. Experimental validation is required to demonstrate that the coating does not exhibit unacceptable fretting behavior.

- **Strain / Ductility**: New strain and ductility limits are to be defined (TBD) through tensile and compressive testing of irradiated Cr-coated fuel cladding [3]. Coating cracking is a po-

tential failure mode under large cladding strain. While experimental observations suggest that cracking in unirradiated coated tubes initiates at approximately 4% clad strain [3], irradiation hardening and the brittle behavior of the intermetallic $ZrCr_2$ layer are expected to reduce this threshold.

- **Fatigue (Strain)**: The strain-based fatigue limit is reached when coating cracking is observed. Thresholds are TBD from irradiated sample testing. Irradiation hardening and the brittle behavior of the intermetallic layer must also be considered to define the new limit.

- **Rod Internal Pressure**: New criteria for fuel–cladding gap closure and potential cladding liftoff must be defined based on TBD irradiation creep characteristics of Cr-coated cladding. As a thin layer, Cr is not expected to change the cladding creep rate considerably, but irradiation creep tests are considered a data gap in the licensing process [3].

- **Fuel Rod Ballooning / Burst**: New rupture stress criteria as a function of temperature and ballooning extent must account for coating delamination and cracking before and after deformation. If cracking occurs post-ballooning, high-temperature oxidation models should be revised to reflect the performance of cladding with a cracked coating [3]. Burst-induced blockage of coolant channels must also be considered.

- **Embrittlement**: Existing limits are intended to prevent excessive cladding ballooning that could lead to embrittlement. However, a chromium coating may alter the ballooning behavior, potentially requiring updates to these criteria. In particular, embrittlement of the coating itself, driven by the formation of a brittle intermetallic layer and irradiation-induced effects, must be considered. Therefore, embrittlement limits should be validated or redefined using unirradiated and irradiated cladding samples [3].

- **Cladding Melting**: This limit is related to loss of coolable geometry. Although the eutectic temperature is 1332°C, its interaction with the Cr coating and potential consequences should be further evaluated.

- **Overheating**: This limit is associated with the boiling crisis. Eutectic formation and the presence of an intermetallic layer may intensify the severity of this regime. Despite being a BDBA condition, its impact on the coating must be assessed.

Table 2.1: Impact of Cr coating failure modes or irradiation aspects on the current zircaloy cladding SAFDLs.

SAFDL	Previous Criterion	Cr failure/aspects
Fuel Assembly		
Fretting	no occurrence	Irradiation hardening, intermetallic layer
Normal operation and AOOs		
Strain / Ductility	$< 1\%$	Cracking, delamination, intermetallic layer, irradiation hardening
Fatigue (Strain)	$\sum_{cycles} < 1\%$	Cracking, intermetallic layer, irradiation hardening
Rod internal pressure	< coolant pressure	Irradiation creep
Accident Conditions		
Fuel rod ballooning / burst	as in NUREG-0630	Cracking, delamination
Embrittllement	$T_{cladding} < 1200°C$, $t_{oxide} < 0.17t_{cladding}$	Cracking, intermetallic layer
Clad melting	$T_{cladding} < 1200°C$	Intermetallic layer, eutectic formation
Overheating	h < CHF or $P_{assembly}$ < CP	Intermetallic layer, eutectic formation

2.3.2 Performances during AOOs and postulated accidents

Specifically for high-temperature steam accident scenarios, such as in a LOCA, the chromium coating is expected to impact the fuel's performance during the accident positively. The coating's main design function is to reduce the oxidation rate during normal and high-temperature scenarios compared to the bare cladding design. Consequently, the cladding might face lower temperatures during the accident progression, reducing the core-wide inventories of liberated hydrogen [4].

2.3.3 Nuclear safety-related aspects of Cr coating

The primary nuclear safety concerns associated with Cr coatings stem from the consequences of their potential failure modes during accident scenarios, particularly under conditions of high tensile stress and elevated temperature. Such conditions are characteristic of LOCA and reactivity-initiated accidents (RIA), which therefore serve as the principal scenarios for evaluating the safety performance of Cr coatings. The severity of the safety implications is directly influenced by the extent of coating failure, which in turn depends on the initial condition of the coating at the onset of the accident, including any pre-existed damage. Figure 2.7 illustrates the main safety-relevant features of Cr coatings, categorized into three interconnected aspects: pre-damage, failure modes, and resulting consequences.

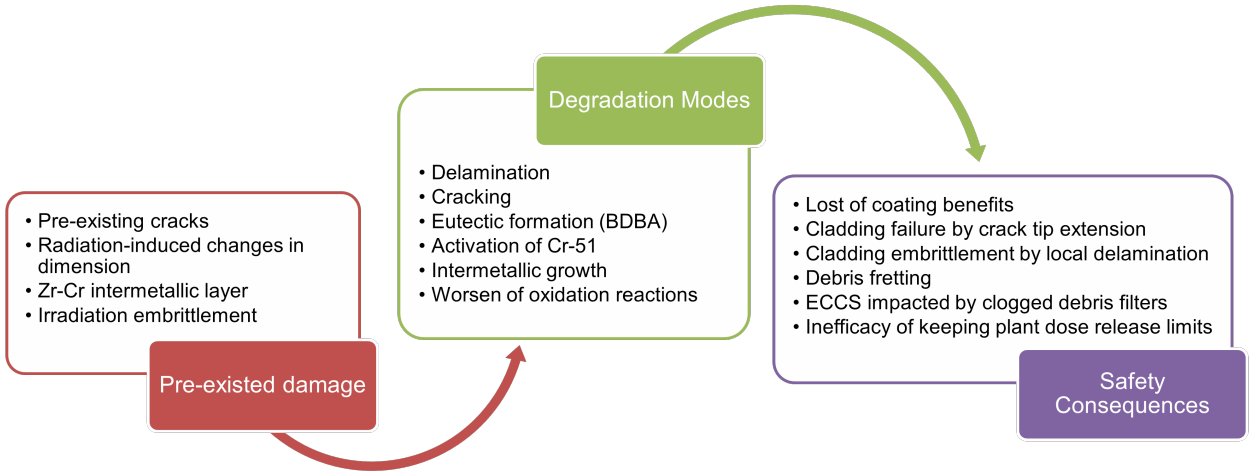

Figure 2.7: Safety-related aspects for Cr-coated claddings before, during, and after design basis accidents (DBA) and BDBA scenarios based on [3].

Coating delamination and cracking are the most probable damage mechanisms under accident conditions [3]. The immediate consequences include the loss of the coating's protective functional-

ity and the generation of debris within the reactor coolant system. In a LOCA scenario, such debris can clog the filters of the ECCS pumps, potentially compromising their operation and endangering core cooling. While the current design of containment sumps in PWRs accounts for a certain level of debris accumulation, an evaluation is needed to assess whether the presence of Cr debris could exceed current design margins. Specifically, further investigation should determine whether Cr debris generation jeopardizes the functionality of sump strainers under accident conditions.

Another safety degradation mechanism that, when combined with coating delamination, can exacerbate nuclear safety concerns is the formation of the radioisotope Cr-51 through neutron activation of the stable isotope Cr-50. If released into the reactor coolant, Cr-51 must be monitored and removed to prevent radioactive plating on reactor components [3]. At present, the amount of Cr-51 release cannot be precisely quantified. However, in the event of significant coating delamination, the release could be substantial, potentially challenging the plant's ability to maintain dose release limits. This coupled risk warrants further investigation. Additionally, irradiation-induced hardening of the Cr coating is anticipated, increasing its brittleness and susceptibility to debris formation from mechanical interactions, such as fretting against other fuel system components. As a result, even in the absence of large-scale delamination, minor quantities of Cr-51 may still be released.

A potential detrimental consequence of coating cracking is the propagation of crack tips into the underlying substrate, which can lead to localized stress concentrations in the cladding and, ultimately, cladding failure. Delamination may also introduce additional risks; partial or localized delamination can result in cold spots that act as sinks for hydrogen diffusion, thereby promoting localized embrittlement and increasing the likelihood of cladding failure. Furthermore, both failure modes—cracking and delamination—are exacerbated by the formation and growth of an intermetallic layer at the coating–substrate interface during high temperature conditions. Their severity is also expected to be amplified in the presence of pre-existing damage.

Pre-existing crack formation during normal transient scenarios is a recognized concern [3]. Initiating an accident scenario with such pre-damage significantly amplifies the consequences of coating cracking. As previously discussed, irradiation-induced embrittlement is expected and is

likely to contribute to crack formation during accident transients. Also, the presence of a brittle intermetallic layer before the onset of a LOCA can potentially jeopardize the entire progression of the accident from its inception.

Although no radiation-induced dimensional changes in the coating were initially flagged as safety concerns in the PIRT [3], a more recent report from the NEA [15] identified swelling and irradiation creep as primary concerns regarding the compatibility between Cr coatings and Zr-based substrates, and called for further investigation. As proposed in the last chapter of this work, pre-cracking may also result from long-term irradiation under steady-state operating conditions, depending on the synergistic effects of all misfit strains from mechanical loads, thermal expansion, irradiation-induced dimensional changes, and creep.

2.4 Insights of irradiation effects

Most evaluations of Cr coating performance presented in the PIRT [3] and in several other studies [2] do not fully account for irradiation effects or their potential synergistic interactions with other degradation mechanisms, such as oxidation behavior, diffusion kinetics, mechanical evolution, and the influence of coating deposition techniques. To address this gap, recent ion irradiation experiments [11, 16–21] have produced valuable data, offering critical insights into the adverse effects of irradiation on Cr-coated systems.

A pre-existed brittle intermetallic compound layer is reported to be stable under irradiation in LWR normal operation condtions. An interlayer with tens of nanometers has been reported to nucleate during the Cr deposition process [17, 22], and grow during normal and transient operation in LWR environments. Li et al. estimated an intermetallic growth of 1μm every 260 days [18] based on the interdiffusion coefficents without considering irradiation. This phase is brittle and is considered the preferential nucleation site for cracking, mainly in not-so-high-temperature conditions [11]. The ideal case would be the irradiation to avoid or reduce the layer nucleation and growth. However, first assessments of this effect showed that the intermetallic layer is stable during irradiation [16].

Also, irradiation effects may enhance interdiffusion at the Cr–Zr interface, increasing the inter-

metallic layer. Ion irradiation at 400°C on bulk Cr has shown a broadening of the interlayer thickness [16, 17]. Conversely, interface sharpening or dissolution was reported in *in-situ* irradiations conducted on very small lamellae under significantly higher dose rates [17]. These contrasting results are attributed to geometrical size effects and different damage rates. However, the conditions for the sharpening results might not be representative of actual reactor environments. Since neutron irradiation more closely resembles the bulk-scale, lower-dose-rate conditions under which broadening was observed, it is more realistic to expect an irradiation-induced growth of the intermetallic layer during normal reactor operation. Nevertheless, further investigation is necessary to validate this hypothesis.

The intermetallic layer at the Cr–Zr interface may undergo irradiation-induced amorphization, a process accompanied by internal volume change, localized plastic deformation, and potential hardening of the affected region. In Zr-based alloys containing chromium, amorphization of precipitates such as $Zr(Fe,Cr)_2$ under moderate temperatures is a well-documented phenomenon [23]. For example, amorphization of $Zr(Fe,Cr)_2$ has been observed to initiate at a fluence of approximately 1×10^{25} n/m^2 at 290°C, equivalent to roughly 120 days in a typical LWR neutron flux. Unlike bare cladding, coated fuel pins feature a continuous intermetallic layer that contributes to the mechanical integrity of the coating–cladding interface. Under reactor conditions, particularly at elevated fluence levels or during power cycling, progressive amorphization and dissolution may occur, potentially compromising the long-term structural stability of the interface.

Recent ion irradiation studies have also reported radiation-induced amorphization in intermetallic compounds [24]. However, because the amorphization process is highly sensitive to the irradiation temperature, dose, and dose rate, a direct correlation between ion and neutron irradiation environments has not yet been conclusively established.

Coating–substrate misfit strain is a critical concern impacting the long-term stability of chromium coatings [25], and irradiation-induced dimensional changes can further exacerbate this issue. Both ion and neutron irradiation studies have confirmed the poor void swelling resistance of Cr [26–28], while Zircaloy has demonstrated strong resistance to swelling under typical LWR dose conditions.

This mismatch in volumetric strain behavior can induce interfacial stresses, particularly at the brittle intermetallic layer formed between the coating and the substrate, increasing the likelihood of crack initiation. Consequently, irradiation-induced dimensional changes represent a key factor affecting the integrity of the coating at the onset of accidental scenarios and must be carefully evaluated in safety assessments.

2.5 Conclusion

Chromium coatings applied to zircaloy cladding have notably improved mechanical strength and oxidation resistance. However, degradation mechanisms and failure modes arising from Cr–Zr interfacial kinetics associated with high-demanding stress and oxidation conditions during an accidental scenario introduce new challenges that will impact nuclear safety in LWR environments. These failure mechanisms primarily affect the ability to meet existing cladding SAFDLs and also give rise to new safety considerations that must be incorporated into the licensing framework and safety design of reactors adopting this advanced cladding technology.

One critical factor that may compromise the oxidation resistance of Cr coatings is the presence of pre-existing damage at the onset of an accident, originating from degradation accumulated during normal reactor operation. While autoclave and mechanical tests have indicated promising stability of Cr coatings in non-irradiated environments, irradiation has shown the potential to exacerbate degradation mechanisms by accelerating interdiffusion, inducing embrittlement, and initiating crack formation. Despite these unresolved challenges, fuel vendors including Framatome and Westinghouse have implemented Cr-coated cladding as a key component of their ATF strategies. Although the Cr coating enhances both oxidation resistance and mechanical durability, their long-term survivability under realistic irradiation conditions remains poorly quantified.

The regulatory qualification of Cr coatings for nuclear applications is progressing rapidly, with approval anticipated by 2027. Despite this momentum, several irradiation-driven degradation mechanisms affecting the coating's protective function remain poorly characterized. To address these knowledge gaps within the accelerated timeline of ATF development, the adoption of fast and dependable surrogate testing methods is essential. As elaborated in the following chapter,

ion irradiation has become an increasingly reliable approach for emulating neutron-induced damage. Its use offers a practical path to expedite safety-related assessments and contributes valuable insights for supporting licensing applications of Cr-coated cladding systems.

2.6 References

[1] U.S. Nuclear Regulatory Commission, "Accident tolerant fuel roadmap to readiness," Version 1.2, Available in: https://www.nrc.gov/reactors/power/atf/roadmap/roadmap-to-readiness.html, March 2025, Accessed on: May 15, 2025.

[2] J. Yang, M. Steinbrück, C. Tang, M. Große, J. Liu, J. Zhang, D. Yun, and S. Wang, "Review on chromium coated zirconium alloy accident tolerant fuel cladding," *Journal of Alloys and Compounds*, vol. 895, p. 162450, 2022.

[3] K. G. Geelhood and W. G. Luscher, *Degradation and Failure Phenomena of Accident Tolerant Fuel Concepts, PNNL-28437 Rev.1*. Pacific Northwest National Laboratory, 6 2019. [Online]. Available: https://www.nrc.gov/docs/ML1917/ML19172A154.pdf

[4] United States Nuclear Regulatory Commission (NRC), "Supplemental guidance regarding the chromium-coated zirconium alloy fuel cladding accident tolerant fuel concept (atf isg-2020-01)," https://www.nrc.gov/docs/ML1934/ML19343A121.pdf, 1.

[5] J. C. Brachet, E. Rouesne, J. Ribis, T. Guilbert, S. Urvoy, G. Nony, C. Toffolon-Masclet, M. L. Saux, N. Chaabane, H. Palancher, A. David, J. Bischoff, J. Augereau, and E. Pouillier, "High temperature steam oxidation of chromium-coated zirconium-based alloys: Kinetics and process," *Corrosion Science*, vol. 167, p. 108537, 5 2020.

[6] L. I. Nicolai and R. H. de Tendier, "Chromium diffusion in zircaloy-4," *Journal of Nuclear Materials*, vol. 82, pp. 439–443, 7 1979. [Online]. Available: https://www.sciencedirect.com/science/article/pii/0022311579900278

[7] M. Steinbrueck, N. Waeckel, and A. Jasiulevicius, "Accident tolerant fuel: an update report 2020-2023 (zirat28/izna 23)," 1 2024.

[8] X. Wu and K. Shirvan, "System code evaluation of near-term accident tolerant claddings during boiling water reactor short-term and long-term station blackout accidents," *Nuclear Engineering and Design*, vol. 356, p. 110362, 1 2020. [Online]. Available: https://www.sciencedirect.com/science/article/pii/S0029549319303942?via%3Dihub

[9] T. Feng, J. Wang, Y. Zhou, P. Song, M. Wang, R. Dailey, W. Tian, and M. L. Corradini, "Quantification of the effect of cr-coated-zircaloy cladding during a short term station black out," *Nuclear Engineering and Design*, vol. 363, p. 110678, 7 2020. [Online]. Available: https://www.sciencedirect.com/science/article/pii/S0029549320301722

[10] J. C. Brachet, T. Guilbert, S. Urvoy, E. Rouesne, M. Peyret, T. Vandenberghe, C. Prou, T. L. Hong, and D. Hamon, "Some practical methodologies to assess the overall high temperature (one-sided) steam oxidation protectiveness of chromium-based coatings on a zirconium-based substrate, as enhanced – accident tolerant (nuclear) fuels (e-atf) claddings," *Journal of Nuclear Materials*, vol. 606, p. 155620, 2 2025. [Online]. Available: https://www.sciencedirect.com/science/article/pii/S0022311525000157

[11] B. Li, T. Davey, H. Yang, J. A. K. Jovellana, S. Kano, Y. Chen, and H. Abe, "Mitigating zrcr2 formation at the cr/zr interface through trace doping of zn, mg and sn into cr coatings: A combined first-principles computational and experimental investigation," *Journal of Nuclear Materials*, vol. 603, p. 155375, 1 2025.

[12] A. Michau, M. Ougier, T. Guilbert, J. Bischoff, E. Pouillier, and H. Maskrot, "Interlayers for Cr-coated nuclear fuel claddings," in *NuMat2020 - The Nuclear Materials Conference*, Ghent, Belgium, Oct. 2020. [Online]. Available: https://cea.hal.science/cea-03345302

[13] J. Yang, Y. Ding, F. Zhao, L. Shang, Y. Cui, S. Wang, D. Yun, and D. Xu, "Microstructure evolution of a cr-cr/mo coated zr alloys in inert gas and steam environment at high temperature," *Journal of Nuclear Materials*, vol. 589, p. 154845, 2 2024. [Online]. Available: https://www.sciencedirect.com/science/article/pii/S0022311523006128

[14] G. H. Mohamed, K. Karuppasamy, M. Alrwashdeh, I. Barsoum, S. Alameri, and A. Alfantazi, "Unveiling the latest progresses in chromium-coated zircaloy cladding atf materials: Fabrication techniques, performance metrics, and beyond," *Alexandria Engineering Journal*, vol. 108, pp. 13–39, 12 2024. [Online]. Available: https://www.sciencedirect.com/science/article/pii/S1110016824007622

[15] N. E. A. (NEA), "Nuclear fuel behavior in loss-of-coolant accident (loca) conditions, isbn 978-92-64-99091-3," p. 123, 2009. [Online]. Available: https://www.oecd-nea.org/upload/docs/application/pdf/2021-03/csni-r2009-15.pdf

[16] A. Wu, J. Ribis, J. C. Brachet, E. Clouet, F. Leprêtre, E. Bordas, and B. Arnal, "Hrtem and chemical study of an ion-irradiated chromium/zircaloy-4 interface," *Journal of Nuclear Materials*, vol. 504, pp. 289–299, 6 2018.

[17] J. Ribis, A. Wu, R. Guillou, J.-C. Brachet, C. Baumier, A. Gentils, and M. Loyer-Prost, "Radiation-induced sharpening in cr-coated zirconium alloy," *Materials*, vol. 15, 2022. [Online]. Available: https://www.mdpi.com/1996-1944/15/6/2322

[18] B. Li, H. Yang, R. Holmes, L. Cui, S. Kano, and H. Abe, "Experimental kinetic study of interdiffusion behavior and intermetallic compound zr(fe,cr)2 formation at the cr/zry4 interface under elevated temperatures," *Journal of Nuclear Materials*, vol. 584, p. 154595, 10 2023.

[19] Y. Zhong, X. Wu, L. Wu, S. Zhao, H. Su, Z. Ning, W. Zhang, N. Liu, and J. Yang, "Microstructural evolution of irradiated cr-coated zr-4 under in situ transmission electron microscopy heating," *Coatings*, vol. 13, p. 1655, 9 2023.

[20] J. Bowman, P. Wang, G. Was, M. Bachhav, and A. Motta, "Ion irradiation induced amorphization of precipitates in zircaloy," *Journal of Nuclear Materials*, vol. 571, p. 153988, 12 2022.

[21] R. Wang, P. Li, B. Li, L. Hu, F. Huang, Q. Huang, and F. Ge, "The oxidation mechanisms of

the xe20+ ion-irradiated cr coatings on zr alloy coupons: Accelerated diffusion and internal oxidation," *Corrosion Science*, vol. 201, p. 110301, 6 2022.

[22] A. Fazi, H. Aboulfadl, A. H. Iyer, M. Sattari, K. M. Stiller, P. Lokhande, M. Thuvander, and H. O. Andren, "Characterization of as-deposited cold sprayed cr-coating on optimized zirlo™ claddings," *Journal of Nuclear Materials*, vol. 549, p. 152892, 6 2021.

[23] R. M. Lobo and A. H. P. Andrade, "Influence of neutron irradiation on the stability of recipitates in zircaloy: a critical review." [Online]. Available: https://inis.iaea.org/search/search.aspx?orig_q=RN:45086072

[24] H. Singh, M. Kumar, and R. Singh, "An overview of various applications of cold spray coating process," *Materials Today: Proceedings*, vol. 56, pp. 2826–2830, 2022, 3rd International Conference on Contemporary Advances in Mechanical Engineering.

[25] Y. Lee, J. I. Lee, and H. C. NO, "Mechanical analysis of surface-coated zircaloy cladding," *Nuclear Engineering and Technology*, vol. 49, pp. 1031–1043, 8 2017.

[26] P. J. Doyle, T. Koyanagi, C. Ang, L. Snead, P. Mouche, Y. Katoh, and S. S. Raiman, "Evaluation of the effects of neutron irradiation on first-generation corrosion mitigation coatings on sic for accident-tolerant fuel cladding," *Journal of Nuclear Materials*, vol. 536, p. 152203, 8 2020. [Online]. Available: https://www.sciencedirect.com/science/article/pii/S0022311520302051?via%3Dihub

[27] L. J. Cui, H. L. Yang, Y. F. Du, Q. Q. Shi, S. Kano, and H. Abe, "Tem characterization of irradiation-induced dislocation loops and voids in ion-irradiated pure chromium," *Journal of Nuclear Materials*, vol. 569, p. 153920, 10 2022. [Online]. Available: https://www.sciencedirect.com/science/article/pii/S0022311522004068?via%3Dihub

[28] A. Gabriel, L. Hawkins, A. French, Y. Li, Z. Hu, L. He, P. Xiu, M. Nastasi, F. A. Garner, and L. Shao, "Effect of dpa rate on the temperature regime of void swelling in ion-irradiated pure chromium," *Journal of Nuclear Materials*, vol. 561, p. 153519, 4 2022.

3. RADIATION-INDUCED EFFECTS IN PURE CHROMIUM: INSIGHTS FROM ION IRRADIATION TECHNIQUES

3.1 Introduction

The degradation behavior of nuclear materials has traditionally been studied using neutron-based irradiation experiments conducted in test reactors [1]. However, with the emergence of advanced reactor designs and novel materials, along with the growing demand to improve nuclear safety and reliability, test reactors have struggled to meet the pace required for timely materials qualification. Existing reactor facilities can typically reach damage rates on the order of a few tens of displacements per atom (dpa) per year, requiring several years to simulate the total damage experienced by proposed nuclear and structural in-core materials, as depicted by Figure 3.1. As an alternative, ion irradiation using particle accelerators offers the advantage of significantly shorter experimental durations due to their substantially higher damage rates.

The use of ion beams to evaluate irradiation damage is not a novel approach, with foundational studies dating back to the 1960s [1]. However, their application as a surrogate to emulate radiation effects under reactor-relevant conditions has gained traction more recently. Despite the main advantage of rapidly achieving high damage doses in short time, ion irradiation offers several other advantages over neutron irradiation, making it a highly promising alternative. These include the absence, or negligible presence, of residual radioactivity in the specimens, the ability , lower operational costs, and greater experimental control over parameters such as dose rate, temperature, and irradiation uniformity.

However, the fundamental differences in the nature of the incident particles and the accelerated damage rate introduce several challenges when using ion irradiation as a surrogate for neutron damage. These challenges include the limited penetration depth of ions, the continuously varying damage rate along the depth profile, and compositional changes due to implanted interstitial atoms. Additionally, ion irradiation is often accompanied by temperature shifts resulting from high dose

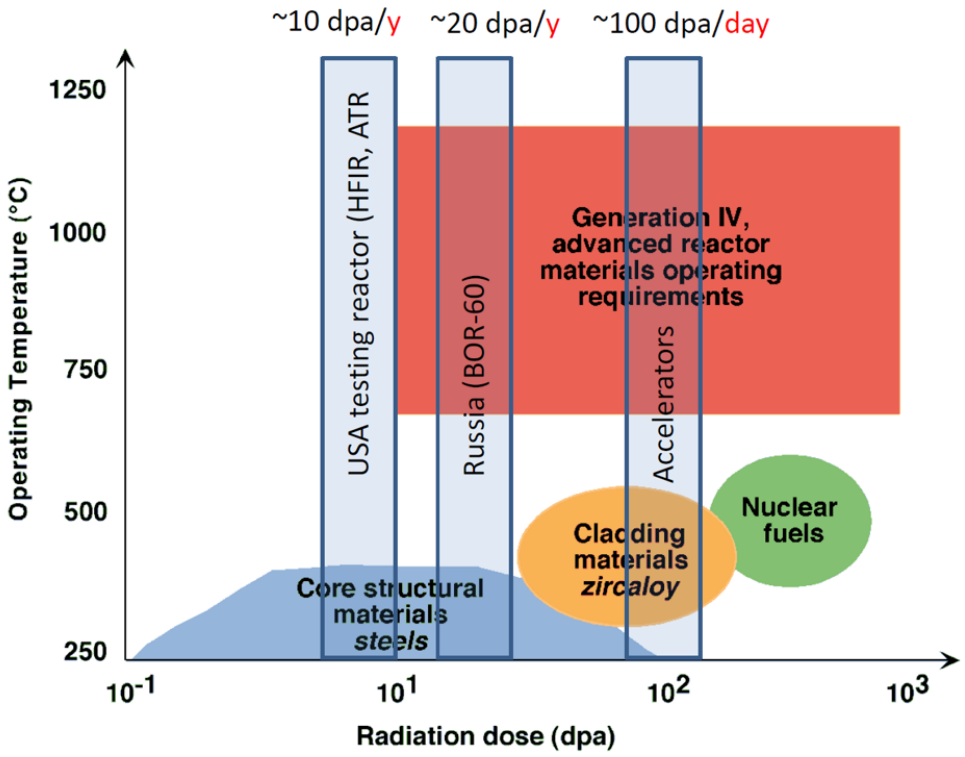

Figure 3.1: Schematic overview of applicable testing methods for different types of nuclear materials with associated operational temperature and damage ranges [2].

rates [3], as well as complex interactions among irradiation time, temperature, and the diffusional redistribution of injected species along the depth of the sample.

Nevertheless, several techniques have been developed to improve the accuracy of ion beam experiments and to better understand the unique effects introduced by ion-beam irradiation [4–6]. As a result, accelerator-based ion irradiation has become increasingly reliable for evaluating the radiation response of materials and been serving as a valuable tool in the design and screening of advanced nuclear materials.

Importantly, ion irradiation is not intended to replace test reactor experiments, but rather to complement them by providing rapid, early-stage insights that can inform material selection, guide system design, and support licensing processes. So, this chapter demonstrates how ion irradiation has been effectively utilized to investigate the performance of Cr coatings applied to zircaloy cladding under irradiation conditions and support licensing next steps.

3.2 Atomic displacements

Neutrons and ions, to a similar extent, induce damage in materials by knocking out atoms from their lattice sites, promoting the so-called damage cascade. These displaced atoms, called primary knock-on atoms (PKA), create a ballistic effect in the crystallographic structure, momentaneously disordering and heating (thermal spike) a certain region in the material that will reorganize again after a short time.

Regardless of the resulting post-cascade defect topology, the damage caused by displacement cascades can be quantified using a standardized approach. For each PKA, the total number of atoms displaced from their original lattice positions during the cascade, denoted as $\nu(T)$, can be estimated based on the PKA energy T. Multiplying $\nu(T)$ by the number of PKAs generated and dividing by the atomic density yields the dpa, which represents the average number of times each atom in the material has been displaced from its lattice site. The calculation of PKA differs between neutron and ion irradiation due to the nature of the incident particles. Neutrons have a broad energy spectrum, whereas ion beams are typically monoenergetic. Nevertheless, once the PKAs' spectrum and the average beam energy absorbed by the target atoms (E_{recoil}) are determined, the resulting dpa can be directly compared between the two irradiation types, as illustrated in Figure 3.2.

For neutron irradiation, the PKA generation—or displacement rate—(R_{PKA}) produces a spectrum of PKA energies, which is integrated with the displacement function ν to determine the total dpa. In contrast, ion irradiation simulations typically rely on binary collision approximation (BCA) Monte Carlo codes, such as SRIM, which provide depth-resolved average PKA energy values per incident ion.

The number of displaced atoms, ν, should be evaluated similarly across both approaches. A commonly accepted formulation is provided by the NRT model [7], as expressed in Eq. 3.1, which is also the recommended standard practice outlined in ASTM E521. In this model, PKA energy must be corrected by subtracting energy losses due to ionization from the resulting recoils (η).

$$\nu(T) = \frac{0.8(T - \eta)}{2E_d} \tag{3.1}$$

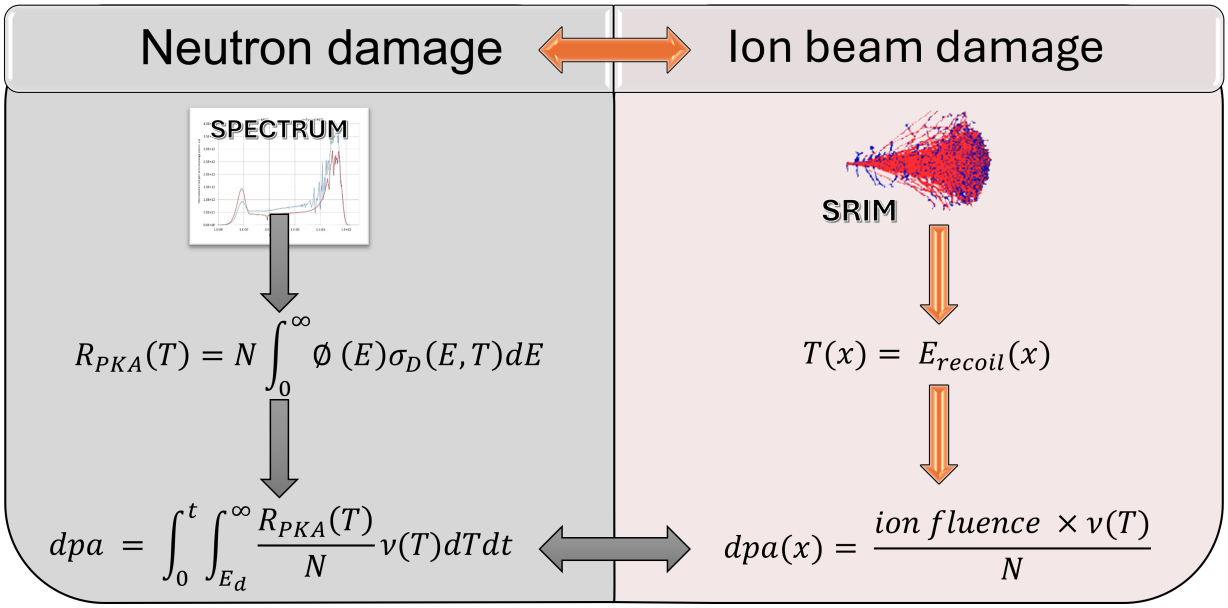

Figure 3.2: Comparison of dpa calculation for neutron and ion beam irradiation, where N is atomic density, E_D is the atom displacement energy, ϕ is the neutron flux, and σ_D is the displacement cross section.

Using dpa as a metric to represent irradiation damage is a simplified approach, as it does not capture the actual configuration of permanent defects following cascade cooldown, nor does it reflect the resulting defect morphology. Nevertheless, this conventional quantity remains a useful means for comparing irradiation-induced changes in materials exposed to different types of incident particles.

It is important to note that the NRT model, while widely adopted, has limitations. It does not account for the complex atomic interactions during the displacement cascade and typically overestimates the number of displacements [8]. Therefore, caution is warranted when comparing data across different studies: the method used to estimate the number of displaced atoms must be consistent to ensure valid and meaningful comparisons.

Accurate calculation of neutron-induced damage is considerably more complex than for ion beam irradiation, primarily due to the broad energy spectrum of neutrons and the diversity of nuclear reactions that contribute to atomic displacements. In addition to elastic scattering, reactions such as (n,xn), (n,γ), (n,p), (n,α), and secondary processes involving energetic daughter isotopes

can also play a significant role in damage production. For ion beam, a standard way to calculate the material damage is given by Stoller et al. [9].

Nevertheless, for specific applications, such as iron-based alloys located within the fueled core region, approximate fluence-to-dpa conversion factors can be satisfactorily employed for neutron damage estimation. Moreover, these factors may be extended to other elements with similar atomic numbers (Z) and comparable displacement threshold energies (E_d), such as cobalt (Co), manganese (Mn), nickel (Ni), and chromium (Cr), provided their displacement cross-sections are comparable and do not significantly alter the damage response function.

These conversion factors, however, must be applied with caution. Neutron damage is always calculated relative to a defined energy threshold, since only fast neutrons, typically with energies exceeding 0.1 MeV, possess sufficient kinetic energy to displace atoms from their lattice positions. Consequently, any fluence-to-dpa conversion factor must be explicitly linked to the energy threshold used in its derivation. For LWRs, standard thresholds are typically E>0.1 MeV or E >1 MeV [10].

3.3 Revelant radiation-induced damage

The net consequence of displacement cascades is the continuous generation of point defects within the material's microstructure. Depending on the energy and frequency of the damaging events, as well as the diffusion kinetics of the defects, which are both temperature and material dependent, these defects can undergo various spatial redistributions. Such processes lead to diverse microstructural evolutions and degradation mechanisms, ultimately altering the material's performance under irradiation.

In addition, the physico-chemical alterations experienced by crystalline materials under ballistic irradiation can be profound, arising from a broad range of irradiation-induced phenomena. These include amorphization, hardening, embrittlement, accelerated phase transformations, corrosion cracking, alloy segregation, and dimensional instabilities such as anisotropic growth, irradiation creep, and cavity swelling [2, 11].

One of the most challenging engineering consequences of neutron irradiation is the develop-

ment of dimensional instability, in which a structural component may undergo volumetric growth or shrinkage, as well as shape distortion, often with both occurring simultaneously [10]. Void swelling is particularly critical due to its potential to cause significant dimensional changes over time.

However, based on the time frame within which each phenomenon manifests during reactor operation, void swelling is considered more detrimental in fast reactor environments. While in PWRs, a type of LWR, it is regarded as the second most critical materials issue, following irradiation-assisted stress corrosion cracking (IASCC).

Typical PWR components susceptible to void swelling are structural elements fabricated from austenitic stainless steels, which are commonly employed in reactor vessel internals. Historically, void swelling was not considered a significant concern in LWRs, primarily due to the relatively low operating temperatures and neutron doses experienced by these materials. However, under extended irradiation exposure, such as operation beyond the standard 40-year licensing period, even modest swelling may accumulate to levels that compromise the mechanical integrity and dimensional stability of these components [11].

In contrast, in-core components at the fuel region are generally fabricated from swelling-resistant materials with well-controlled growth and irradiation creep behavior. Zirconium (Zr) has been used as material for fuel rods and space grids because its dimensional stability is predictable and does not jeopardize the fuel assemblies. The zircalloy swelling amount is negligible during LWR operational conditions and lifetime.

This difference in swelling-resistance between components arises because the damage rate in in fuel regions is typically orders of magnitude higher than outside. As illustrated in Figure 3.3, fast neutrons generated during fission are highest in the core middle region, getting progressively moderated to lower energies towards the boundaries, with a fraction also escaping the fuel region. Therefore, the selection of any new in-core material, such as for coated-cladding, must ensure adequate resistance to irradiation-induced degradation to preserve dimensional and mechanical integrity under normal operation, AOOs, and accident scenarios.

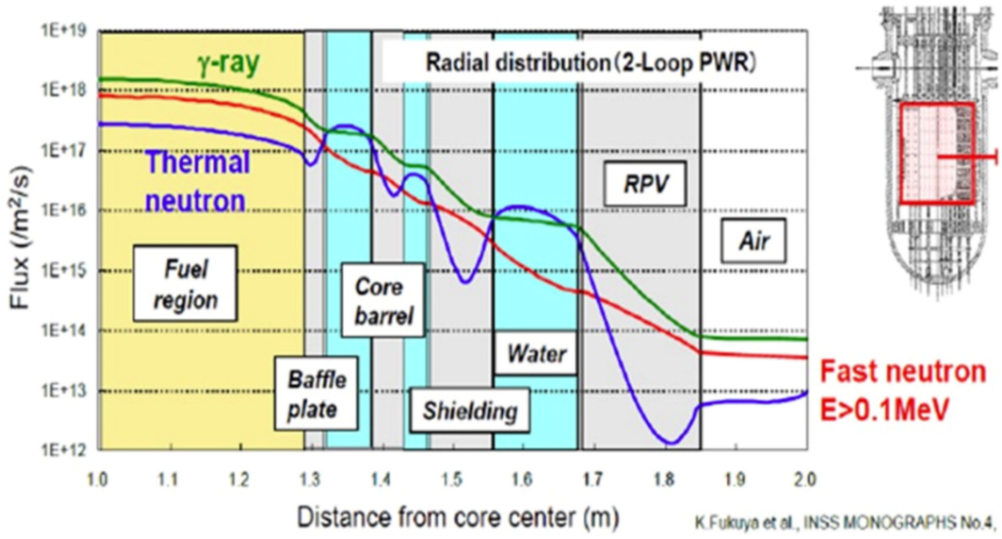

Figure 3.3: In-core radial profiles of gamma-ray (green), fast neutron (red), and thermal neutron (blue) fluxes of a two-loop PWR [10]. Fast neutron flux (also damage) in the core region is three orders of magnitude higher than at the RPV.

3.3.1 Void Swelling

Void swelling is a dislocation-driven mass redistribution process induced by radiation, characterized by vacancy clustering that results in a macroscopic increase in the material volume (V), which is generally isotropic [10]. It was first observed in the late 1960s in fast reactor environments. Since its discovery, it has become one of the most extensively studied irradiation effects [10, 11]. Continued research has led to the development of a widely accepted rate theory model [12], which captures the essential mechanisms governing cavity growth.

As with any phase transformation or microstructural evolution, void swelling undergoes a characteristic progression that includes a nucleation threshold, a transient regime, and eventually a steady-state condition. The steady-state stage is typically characterized by a prolonged and constant swelling rate ($\Delta V/V \propto$ dose) driven by the continuous generation of point defects under irradiation. However, at sufficiently high doses, swelling may approach saturation. This occurs when cavities themselves evolve into dominant defect sinks, surpassing dislocations in their ability to absorb point defects. The rate theory parameter that captures this competitive behavior is the

sink strength ratio between dislocations and cavities, denoted as Q, and defined by:

$$Q = \frac{z_{i,\nu}^{d} L}{z_{i,\nu}^{c} \, 4\pi \bar{r}_c N_c} \tag{3.2}$$

where $z_{i,v}^{d}$, $z_{i,v}^{v}$ are the bias factors of the dislocations and cavities for trapping point defects, L is the total dislocation length, $\bar{r}_c N_c$ is the average cavity size times the cavity density.

Figure 3.4 illustrates the characteristic evolution of swelling across different irradiation doses, emphasizing how key variables influence transitions between swelling regimes. In the initial transient regime, swelling progresses slowly due to the limited cavity radius and density (Q > 1) and the dominance of point defect (PD) recombination. As the dislocation density stabilizes near a quasi-equilibrium value of $\sim 3 \times 10^{10}$ cm^{-2} [10], and under appropriate irradiation temperatures, cavities grow until reaching a critical radius r_c^*, at which point their sink strength rivals that of dislocations (Q $\sim$ 1). Although cavities begin absorbing more PDs at this stage, dislocations still attract a greater flux of self-interstitials (SIAs) due to the dislocation bias—the preferential absorption of interstitials over vacancies. Consequently, even when sink strengths are balanced, vacancy supersaturation persists, enabling continued cavity growth through a net flux of vacancies.

This regime of quasi-static equilibrium between defect production and selective absorption characterizes the steady-state swelling, which is primarily governed by the material's intrinsic properties, such as crystallographic structure and defect energetics. On the other hand, the transient regime is influenced by both intrinsic factors, such as temperature and dpa rate, and extrinsic parameters, including phase distribution, chemical composition, degree of cold work, and microstructural heterogeneity. In the next sections, a brief explanation of the swelling mechanisms and the intrinsic features that affect the swelling growth is given.

3.3.1.1 Nanostructural mechanisms

Void swelling is driven by the non-equilibrium distribution of point defects generated during displacement cascades, wherein the preferential trapping of interstitials over vacancies at dislocations, known as dislocation bias, reduces the likelihood of vacancy-interstitial recombination,

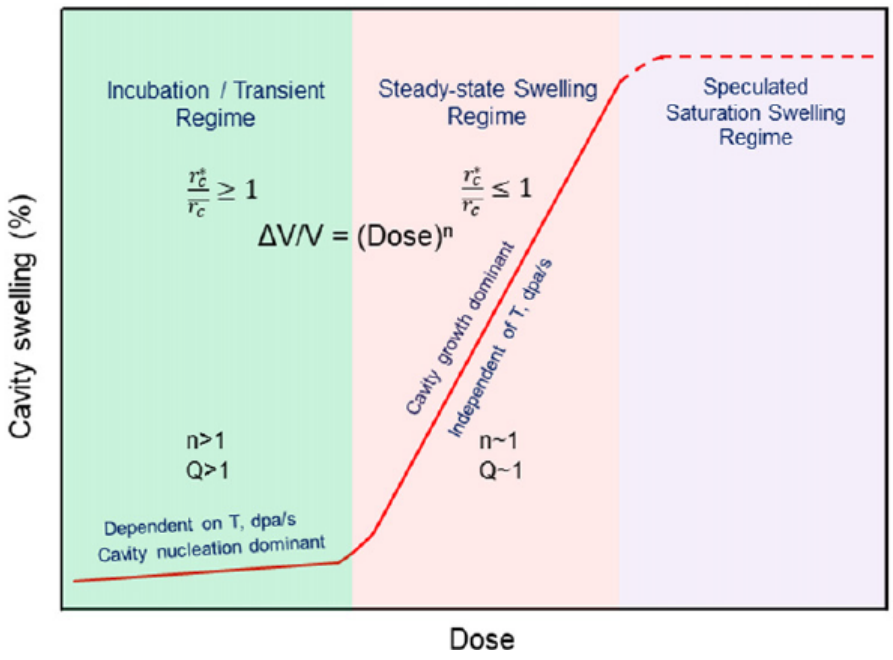

Figure 3.4: Illustrations of swelling phases as a function of dpa, showing different features that affect each regimen. [11]

.

thereby generating a local gap between vacancy and SIAs concentrations. Figure 3.5 illustrates the dislocation bias effect.

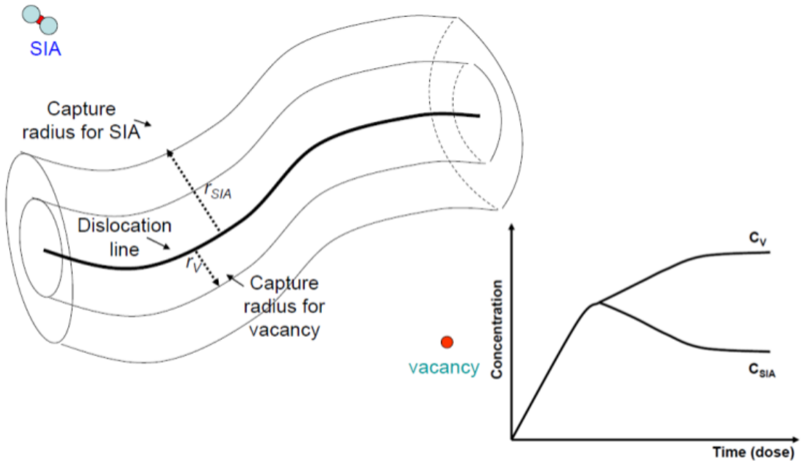

Figure 3.5: Effect of dislocation bias for trapping self-interstitials, creating a concentration gap between defects [13]

.

The existence of dislocation bias for interstitials can be verified by examining a simplified form of the cavity growth rate equation, under the assumption that only mono-vacancies and mono-interstitials are generated during irradiation [11, 14]:

$$\frac{dr_c}{dt} = \frac{\Omega}{r_c}\left[Z_v^c D_v \left(C_v - C_v^{eq}(r_c)\right) - Z_i^c D_i C_i\right] \tag{3.3}$$

where Ω is the atomic volume, r_c is the cavity radius, D_v, D_i are the vacancy and interstitial diffusion coefficients, Z_v^c, Z_v^i are the bias factors of the cavity for absorbing vacancies and interstitials, C_v, C_i are the physical point defect concentrations, and C_v^{eq} is the thermal concentration of point defects at a cavity of radius r_c. Eq. 3.3 can be further simplified with C_v - $C_v^{eq} \approx C_v$ because in typical irradiation conditions, where vacancies are mobile, the vacancy supersaturation created by the irradiation is much higher than C_v^{eq} [11]. Also, Z_v^c, Z_v^i can be taken as unity since cavities are considered neutral (non-biased) sinks.

Assuming that the leakage of point defects due to diffusion is negligible compared to their loss via recombination and absorption at sinks, the rate equations for point defect concentrations can be simplified as:

$$\frac{dC}{dt} = \text{production rate} - \text{recombination rate} - \text{loss rate at sinks}$$

$$\frac{dC_v}{dt} = G - \alpha C_v C_i - K_v D_v C_v \tag{3.4}$$

$$\frac{dC_i}{dt} = G - \alpha C_v C_i - K_i D_i C_i \tag{3.5}$$

where G is the defect production rate, α is the strength of the recombination rate, and K_v,K_i represent the sink strengths (biased and neutral) for vacancy and interstitial absorption, respectively. These sink strengths incorporate bias effects from various microstructural features, including dislocations, dislocation loops, and cavities.

At steady state, $\frac{dC_v}{dt} = \frac{dC_i}{dt} = 0$, yielding the relation:

$$D_i C_i = \frac{K_v}{K_i} D_v C_v \tag{3.6}$$

Substituting this expression into Eq. 3.3, we obtain:

$$\frac{dr_c}{dt} = \frac{\Omega}{r_c} D_v C_v \left[1 - \frac{K_v}{K_i}\right] \tag{3.7}$$

If all sinks were neutral, then total strength to absorb vacancies or SIAs would be the same ($K_v = K_i$), meaning the cavity radius would remain constant under steady-state conditions. However, experimental observations confirm the continuous growth of cavities, necessitating the presence of a bias, specifically, a stronger trapping tendency for interstitials at dislocations and other sinks. This asymmetry in sink strengths leads to a net accumulation of vacancies and thus drives void swelling.

The preferential absorption of interstitials at dislocations is primarily attributed to the longer-range strain fields of SIAs compared to vacancies. The larger formation volume of an SIA, which is approximately twice the atomic volume of a vacancy, generates a large positive strain center, while a vacancy has a weak negative strain field [11]. The asymmetry in strain interactions with dislocations establishes the bias.

While the simplified bias-based explanation clarifies the mechanism driving cavity growth, it does not encompass the full range of factors influencing void swelling. Most notably, the swelling rate is intrinsically dependent on the spatial and temporal distribution of point defects following the displacement cascade. This distribution is primarily governed by the intrinsic properties of the defects, including their formation energies, mobilities, and binding energies [11]. These defect characteristics are strongly affected by the material's crystallographic structure, making void swelling highly structure-dependent. For instance, Figure 3.6 illustrates that a 25 keV PKA in copper, which has a face-centered cubic (FCC) structure, generates a compact defect distribution characterized by well-defined vacancy and interstitial clusters. In contrast, the same PKA energy in BCC iron leads to a more dispersed and less ordered defect configuration.

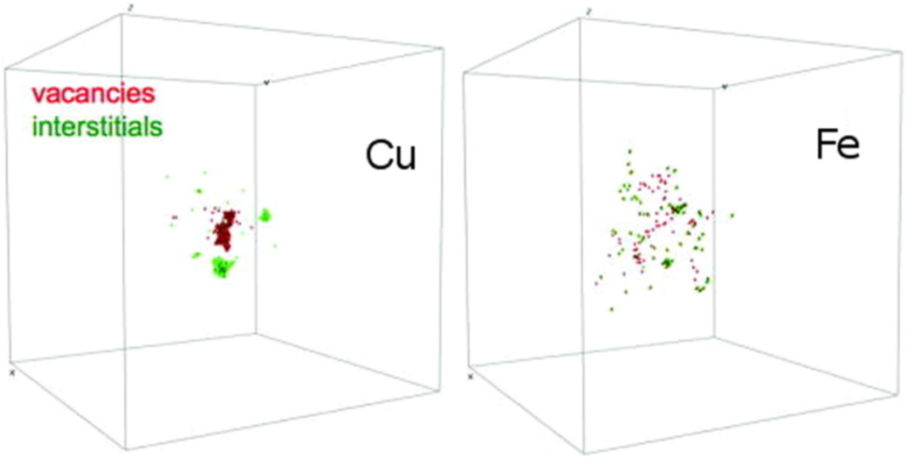

Figure 3.6: Molecular dynamics (MD) results of the defects spatial distribution after a 25-keV PKA cascade transient peak (> 2 picoseconds) in BCC iron and FCC copper. [11]

These differences in defect configurations can be understood by considering the atomic packing factor (APF) of the underlying crystal structures. FCC lattices are more densely packed than BCC lattices, with APF values of 0.74 and 0.64, respectively. The lower packing density in BCC inherently enhances the mobility of defects and promotes a more effective defect dispersion.

This trend is further supported by the higher-energy barriers for interstitial formation and migration, for instance, in iron-based FCC alloys about twice those in BCC alloys. As a result, these intrinsic structural differences give rise to correlated characteristic swelling behaviors where austenitic alloys (FCC) steady-state swelling is usually two times the ferritic rates [15]. Overall, the general influence of crystal structure on void swelling can be summarized as FCC < BCC < HCP [11].

3.3.1.2 Temperature dependence

Temperature exhibits a non-monotonic, bell-shaped effect on void swelling. At low temperatures, vacancy mobility is limited, hindering their ability to migrate and cluster, thereby suppressing void nucleation and growth. Conversely, at high temperatures, although vacancy mobility is enhanced, the increased rate of vacancy emission from cavities can exceed the absorption rate, leading to cavity growth reduction or shrinkage. As a result, there exists an intermediate tem-

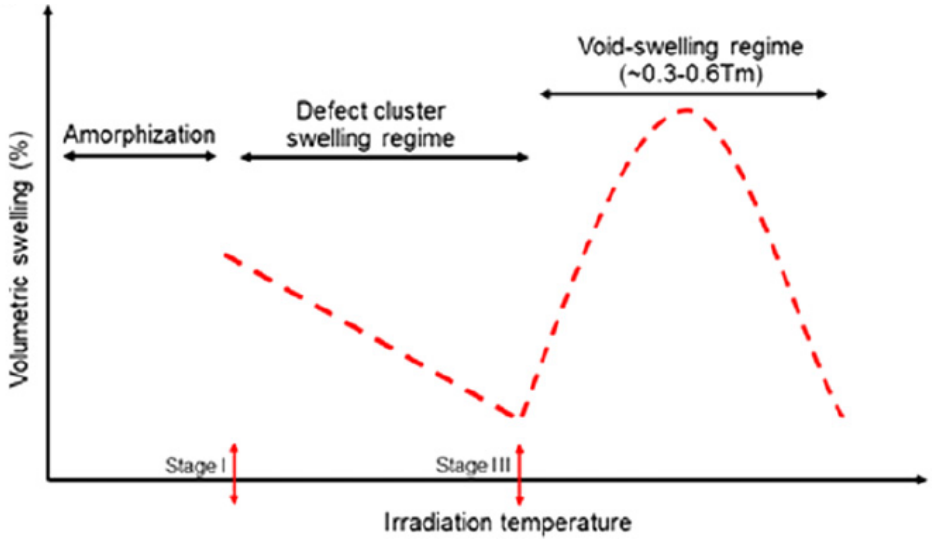

Figure 3.7: Representation of the three main swelling regimens induced by irradiation in most materials. [11]

perature range where the conditions for vacancy accumulation and clustering are optimal, and steady-state void swelling reaches its maximum. At this point, the temperature is known as the peak swelling temperature (T_{peak}).

Void swelling occurs in most metals and alloys within the temperature range of 0.3 to 0.6 T_m, where T_m is the melting temperature. Therefore, the T_{peak} inside this range is also characteristic of each material. This temperature range overlaps with the operational regimes of several nuclear reactor systems, including liquid metal fast breeder reactors, molten salt reactors, and LWRs. Thus, the correct selection of nuclear materials shall carefully consider the characteristic temperatures for swelling. Below this range, PD mobility becomes limited, leading to the emergence of alternative swelling types that are more important for ceramics, though. These are known as amorphization, when PD mobility is negligible, causing the accumulation of unrecombined defects, and defect cluster swelling, when only SIAs and small interstitial clusters are mobile, but they promote a general increase in the lattice parameter. All these three regimens are illustrated by Figure 3.7.

The onset of swelling begins at the temperature at which vacancies acquire sufficient mobility to migrate and cluster. In FCC metals, the tendency for pronounced vacancy clustering during the

displacement cascade (Figure 3.6) requires higher thermal energy to dissolve the initially formed vacancy aggregates. Consequently, the swelling onset temperature in FCC materials is typically higher ($\sim 0.3\ T_m$) than in BCC structures ($\sim 0.2\ T_m$), where vacancy clustering is less prominent. As the temperature increases, the critical cavity radius also increases, leading to a reduction in the overall cavity density and an increase in the average cavity volume. This behavior, known as the Ostwald ripening effect, reflects a dissociation process in which smaller cavities dissolve and contribute to the growth of larger ones, favoring the coarsening of the cavity population.

Despite the total amount of swelling varying with temperature, for a given dose and dose rate, temperature has a relatively small effect on the characteristic steady-state swelling rate. Instead, it plays a more significant role during the initial nucleation and transient swelling stages. When the dose rate changes, it interacts synergistically with temperature in complex ways to influence void swelling behavior. For instance, increasing the dose rate can shift the peak swelling temperature to different values, as discussed in the next section.

3.3.1.3 Dose and dose rate dependence

The dose dependence of swelling gives rise to distinct swelling phases, as illustrated in Figure 3.4. The general features of swelling behavior as a function of dose are preserved regardless of the type of bombarding particle—whether neutrons or charged particles, particularly self-ions in the 3–5 MeV [10]. For example, the characteristic post-transient swelling behavior observed under ion irradiation closely resembles that induced by neutron damage, as illustrated in Figure3.8. This similarity arises because the primary driving force for microstructural evolution in both cases is the damage cascade generated by the PKA. Both energetic neutrons and heavy ions are capable of producing comparable in-cascade recombination and clustering [10]. Neglecting, for the moment, the neutron-atypical aspects of ion irradiation (e.g., injection of implanted species), the most significant difference between neutron and ion irradiation lies in the damage rate. In neutron irradiation environments, dose rates typically range from 10^{-8}, to 10^{-7} dpa/s in thermal reactors and from 10^{-7} to 10^{-6} dpa/s in fast reactors. In contrast, ion irradiation experiments are generally conducted at much higher dose rates, in the range of 10^{-3} to 10^{-4} dpa/s.

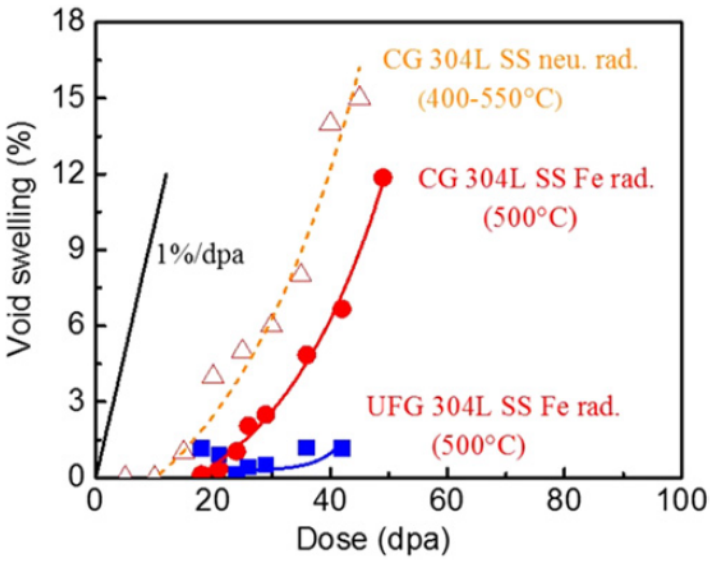

Figure 3.8: Swelling profile as a function of dose of AISI 304 with different pre-treatment bombarded with 3.5 MeV Fe compared to neutron irradiation data, showing preserved swelling features, such as similar steady-state swelling rate of 1%/dpa. [10]

Notably, the dose rate strongly affects two primary aspects of swelling: the corresponding temperature regime and the duration of the transient regime [10, 11]. The first expected consequence of a dose rate variation is a change in PD concentrations, which in turn alters the recombination rate. Higher dose rates lead to elevated PD concentrations and enhanced recombination, thereby reducing the net flux of vacancies toward cavities. Consequently, higher temperatures are required to facilitate more efficient PD removal via sink absorption, in order to balance the increased recombination. The overall effect is a shift of the swelling temperature range toward higher values as the dose rate increases to replicate equivalent swelling conditions. On the same side of the coin, higher recombination rates also extend the transient regime, as the evolution of cavities and dislocation lines or loops requires more time to fully develop their sink strength when PDs are being rapidly consumed by the recombination process.

Temperature shift models [12, 14] can be employed to estimate the corresponding temperature at typical reactor dose rates that would replicate equivalent swelling observed in accelerator-based experiments. A generic formula to calculate the peak-swelling temperature—under the assumption

of unchanged dislocation densities, neutral defects, and strengths—has the form of [16]:

$$\frac{1}{T_{\text{peak}}} \approx a \times \log_{10} K + c \tag{3.8}$$

where a is a function of activation energy of self-diffusion and vacancy migration energy, c is determined by various microstructural parameters including dislocation density, dislocation loop density, and their defect trapping efficiencies, and K is the damage rate in dpa/s.

The parametrization introduced by Eq. 3.8 should be used with caution, as variations in irradiation temperature can alter dislocation densities and the effective strengths of defect sinks. Nevertheless, it provides a useful approximation for identifying the peak-swelling temperature region across different damage rates, making it particularly valuable for correlating accelerator-based experimental data with conditions in nuclear reactor environments. Furthermore, the dose rate dependence predicted by classical rate theory modeling has shown good agreement with experimental observations [11], supporting the applicability of this approach across a range of irradiation scenarios.

Experimental data shown in Figure 3.9 illustrate an approximately linear dependence of peak-swelling temperature on the logarithm of the dose rate. For structural metals relevant to nuclear energy systems, such as iron and its alloys (e.g., ferritic–martensitic and austenitic steels), copper (Cu) alloys, and nickel (Ni), the peak-swelling temperature typically ranges from 300 to 550°C at reactor-relevant dose rates. However, when subjected to accelerator-based irradiation with substantially higher dose rates, this peak shifts to a higher interval of approximately 400–650°C [11].

3.3.1.4 Stress dependence

Stress states, mainly its deviatoric components, assist the evolution of the dislocation network, accelerating the onset of swelling. However, different from the irradiation temperature, dose and dose rate, the dependence of void swelling on stress state is considered a second-order effect. If the material has a good swelling resistance, meaning a large incubation period, the effect of stress, either tensile or compressive, can shorten the transient regimen significantly. On the other hand, if

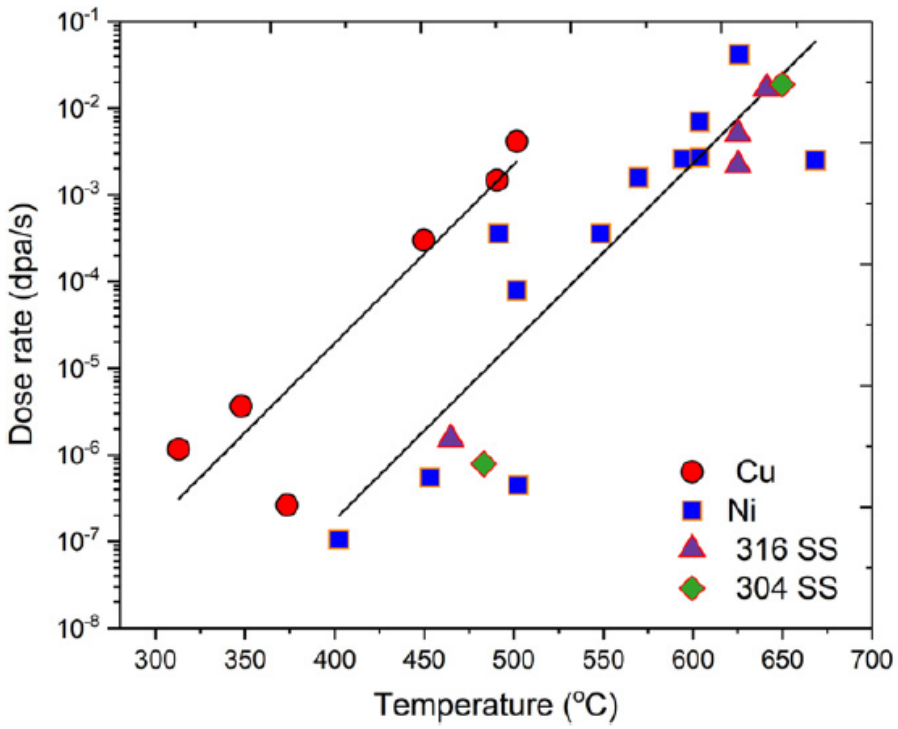

Figure 3.9: Peak swelling temperatures as a function of dose rate in various FCC materials (Cu, Ni, 304 and 316 stainless steels) [11]

the material swells easily, this effect is negligible [10].

Swelling isotropic behavior in irradiated materials is independent of the applied stress state, as evidenced by the work of Gilbert and Garner on AISI 316 stainless steel irradiated in a fast reactor. In contrast, irradiation creep is anisotropic, responding preferentially to the direction of the applied shear stress. This fundamental difference is particularly important because, as discussed in subsequent sections, the onset of swelling marks the beginning of a coupled interaction between swelling and creep, where the two phenomena become interdependent and collectively influence the material's deformation behavior.

3.3.1.5 Impacts on reactor operation

In unrestrained configurations, swelling can lead to distortion or the loss of dimensional tolerances, particularly under non-uniform irradiation conditions involving spatial gradients in temperature and dose rate. In constrained components, such as those found in structural assemblies,

the misfit strains induce stresses within the component itself and exert additional mechanical loads on neighboring materials. This stress transfer is believed to contribute to failures such as cracking in baffle–former bolts observed in LWRs [18]. The induced internal stresses activate irradiation creep, which facilitates stress relaxation by redistributing deformation in unrestrained directions [10].

Importantly, void swelling and irradiation creep are interrelated phenomena. Although irradiation creep can occur in the absence of swelling when stress is present, the onset of swelling enhances the creep response, accelerating creep deformation and stress relief. When the resulting creep strain is excessive, it can introduce spatial mismatches and mechanical instabilities between interacting components.

Void swelling can influence several physical properties of structural materials, including elastic modulus, electrical resistivity, and thermal conductivity [10]. While these changes are generally modest at low swelling levels, they become more significant as swelling increases. For example, reductions in Young's modulus of approximately 1–3% per 1% swelling have been reported for standard reactor alloys. Although thermal conductivity is also expected to decline with swelling, available data are scarce due to the inherent difficulty of such measurements. Notably, the coefficient of thermal expansion remains largely unaffected by void swelling [10].

Beyond these physical properties, void swelling may lead to loss of fracture strength through the degradation of grain boundary cohesion, driven by the accumulation of voids at these boundaries—an type of sink not considered by classical rate theory models [19]. Another mechanism by which void swelling undermines fracture toughness is through the development of stress concentration zones between adjacent voids. When the void volume fraction exceeds a critical limit, these localized stresses can trigger severe embrittlement. In austenitic stainless steels irradiated at 400°C, such embrittlement has been observed at swelling levels approaching 10% [20], reflecting a state of pronounced microstructural deterioration.

Cavity swelling encompasses both void and bubble swelling, each driven by different mechanisms and conditions. While void swelling is primarily associated with point defect dynamics,

bubble swelling is strongly influenced by the presence of noble gases such as helium (He), krypton (Kr), and xenon (Xe). In fission environments, He is predominantly generated through (n,α) reactions, while Kr and Xe are common gases of the fission product. Bubble swelling is particularly relevant in fusion first-wall components and fast and thermal reactor fuel elements, with limited relevance in structural components of thermal reactors. In the context of this study, which evaluates chromium (Cr) as a protective coating for Zircaloy cladding in a thermal reactor, bubble swelling is not considered significant and is therefore excluded from further discussion. Readers interested in detailed mechanisms involving helium and its role in cavity evolution are referred to [10, 11].

3.3.2 Irradiation Creep

In environments where thermal creep is negligible by low temperatures, irradiation serves as a dominant driver of creep deformation. This irradiation-enhanced creep results from the interplay between radiation-induced defect generation and stress-assisted mechanisms that promote directional dislocation formation and motion, particularly via climb and climb-assisted glide.

When stress is present, loops nucleate preferentially on planes oriented with respect to the shear stress—parallel for interstitial loops and perpendicular for vacancy loops—through a mechanism termed stress-induced preferential nucleation (SIPN). SIPN causes the solid to increase in length in the direction of the applied tensile stress. Moreover, the stress field induces anisotropic absorption of SIAs by dislocations, adding atoms to the extra half-planes of the aligned dislocations (stress and Burgers vector alignment) and removing atoms from non-aligned dislocations (preferred vacancy absorption). The net effect is the climbing of the aligned dislocations. This process is known as stress-induced preferential absorption (SIPA). If the stress state allows gliding of the dislocation following each climb step, additional deformation is accumulated through climb and glide, referred to as preferential absorption glide (PAG). The consequences of these underlying mechanisms are schematically depicted in Figure 3.10.

Even without external stress, irradiation inherently drives the formation of loops and promotes PD absorption. This process underlies the same dislocation-driven mass redistribution that contributes to swelling, where material is isotropically shifted from void sites to the grain boundaries

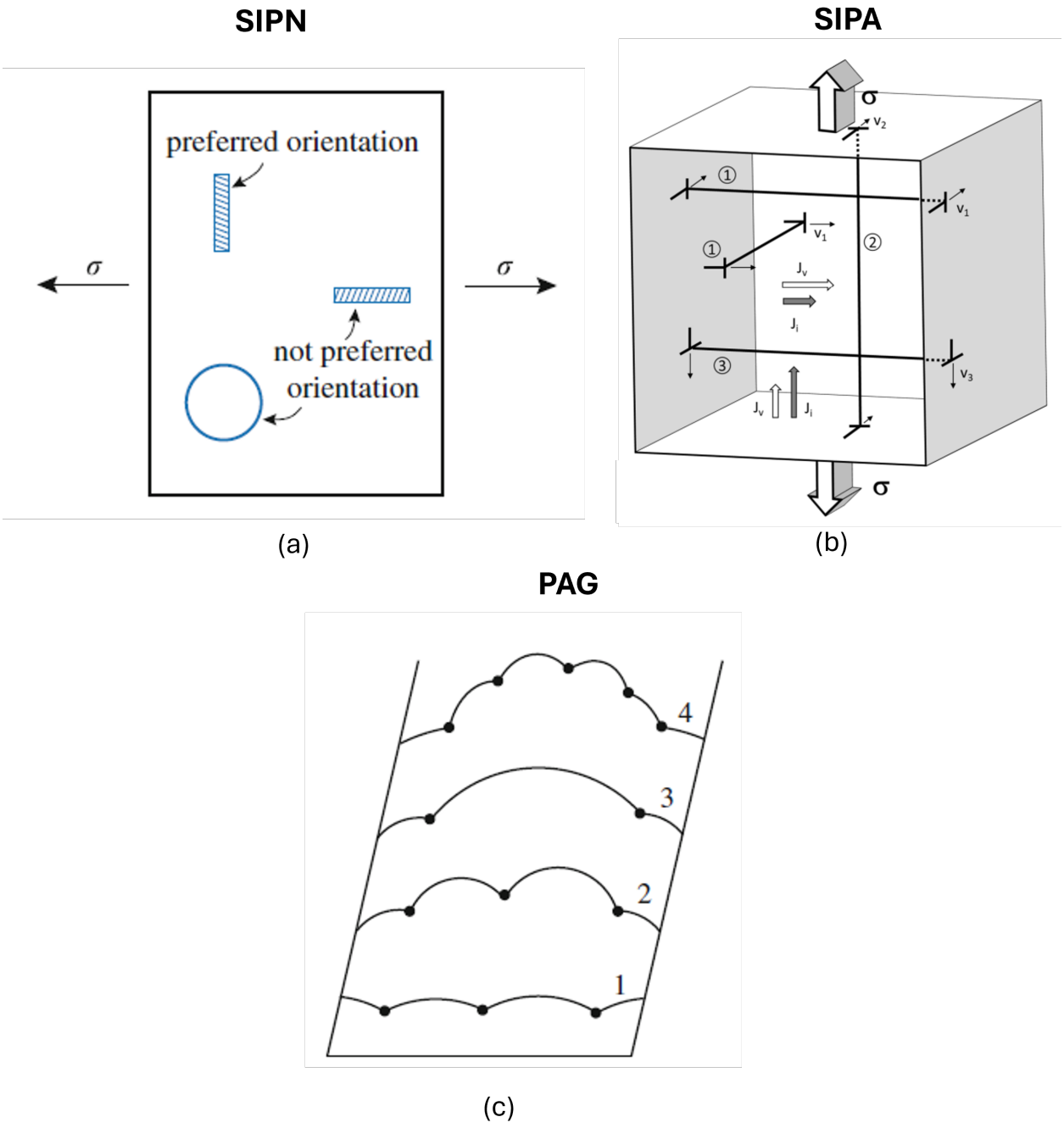

Figure 3.10: Schematics of irradiation-stress-assisted mechanisms that promote creep through dislocation network anisotropic formation (a), dislocation climb promoted by net flux of interstitial (b), and climb-assisted glide by dislocation bowing (c). The illustrations were combined from [8] and [21].

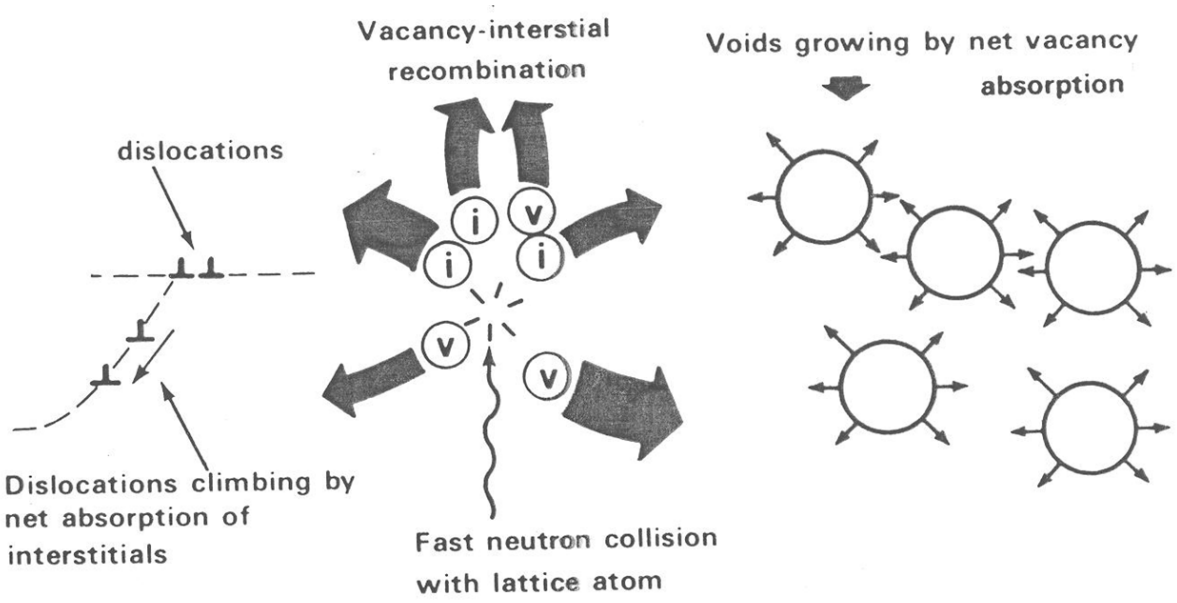

Figure 3.11: Illustration of the dislocation-driven motion of mass enhanced by void swelling.

[10].

Importantly, mechanisms such as SIPN, SIPA, and PAG are already active at early stages, well before voids begin to nucleate and grow, accounting for the presence of irradiation creep in the pre-swelling regime. As the irradiation dose accumulates and recombination becomes less effective, vacancy sink strength increases, resulting in a net vacancy flux toward cavities. This, in turn, drives an opposing flux of SIAs toward dislocations, amplifying dislocation climb, as depicted in Figure 3.11. Thus, in the presence of applied stress, swelling synergistically enhances SIPA and PAG, culminating in a compound mechanism referred to as climb and glide driven by dislocation bias. At this stage, irradiation creep becomes largely governed by the swelling process, with creep strain rates strongly correlated to the swelling rate. This behavior is validated by experimental results shown in Figure 3.12, which clearly demonstrate the dominance of swelling onset in accelerating irradiation creep.

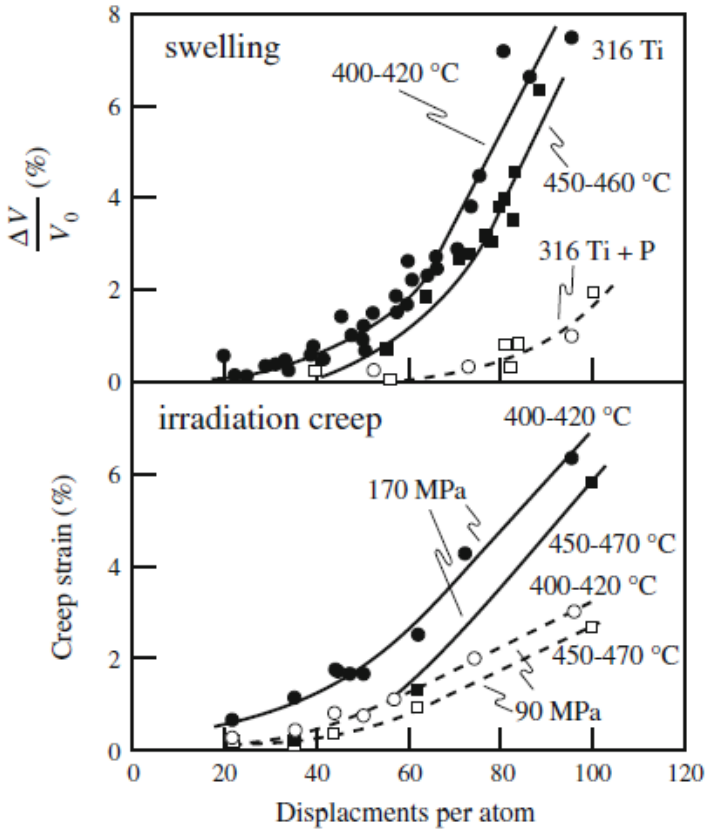

Figure 3.12: Swelling and creep strain in irradiated steels as pressurized tubes [8].

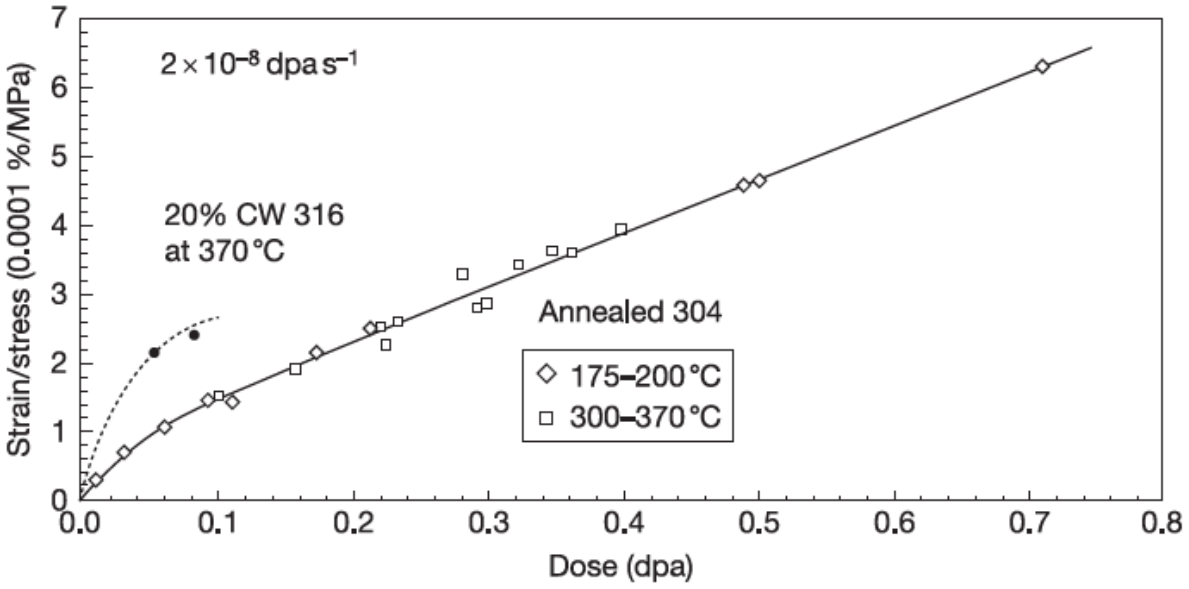

Figure 3.13: Irradiation creep results in a reactor test when swelling is either zero or just beginning [10], showing the features of Eq. 3.9.

3.3.2.1 Creep stages

Consistent experimental data show four distinct stages for irradiation creep. These are the transient regime, the creep regime in the absence of swelling, swelling-enhanced creep, and creep disappearance [10]. When swelling is negligible (S $\sim$ 0), the creep strain has a transient and steady-state term, as depicted in Figure 3.13, which can be fitted as:

$$\varepsilon_{cr}^{S\sim 0} = A\left[1 - \exp\left(-\frac{dpa}{\tau}\right)\right]\bar{\sigma} + B_0\bar{\sigma}^n\phi^m t \tag{3.9}$$

where the time dependence is given by the amount of damage in dpa, A and τ are material-specific constants determined experimentally, m and n are fitting parameters, $\bar{\sigma}$ is the effective stress, and B_0 is the creep compliance term.

SIPN and several other mechanisms have been proposed to govern the transient regime of irradiation creep and swelling [8]. However, in practical terms, the duration of the transient phase can be interpreted as the time required to establish a quasi-equilibrium dislocation density. This balance may be achieved either through recombination–annihilation mechanisms that reduce dislocation density or through irradiation-induced dislocation formation that increases it, particularly in pre-annealed materials. In applications involving high irradiation doses and long exposure times, the transient phase is typically short and often negligible [10].

In the steady-state regime, particularly for iron-based alloys, the coefficient B_0 is considered a material-specific constant primarily governed by the crystallographic structure. This parallels the behavior of the steady-state swelling rate, as detailed in Section 3.3.1.1. Notably, B_0 has been observed to remain invariant with respect to dpa rate and temperature across a broad range of reactor-relevant conditions [10]. Additionally, experimental observations suggest that the empirical exponents m and n generally take values close to unity [8].

When void swelling initiates, the steady-state creep strain rate is augmented by an additional term proportional to the swelling rate ($\dot{S}$), as described by Eq. 3.10. This relationship captures the linear coupling between swelling and irradiation creep, particularly through dislocation climb and

glide mechanisms activated by dislocation bias [8]. The coefficient D, known as the creep-swelling coupling factor, quantifies this contribution and has been found to exhibit a near-universal value of $\sim 0.6 \times 10^{-2}$ MPa^{-1} in iron-based alloys. This near-universal behavior is attributed to the fact that both swelling and creep reach steady-state values, characterized by B_0 and $\dot{S}$ respectively, that are intrinsically tied to the crystallographic structure, making the coupling between them largely invariant across different materials.

$$\dot{\epsilon}_{cr} = \bar{\sigma}(B_0 + D\dot{S}) \tag{3.10}$$

The final phase of the irradiation creep response is marked by a decline or disappearance of creep, which does not necessarily align with the saturation of swelling, as depicted in Figure 3.4. In fact, significant swelling can induce fluctuations in material response and lead to a sharp decrease in creep rate. This behavior has been documented in multiple experiments involving austenitic stainless steel fuel pins, as illustrated by Figure 3.14, where a noticeable reduction in creep occurs once the steady-state swelling rate of approximately 1%/dpa is reached [10]. Despite these observations, the mechanisms driving this phenomenon remain inconclusive [10]. Therefore, the onset of creep reduction must be interpreted with caution and evaluated based on each case's specific material and irradiation conditions.

3.3.2.2 Practical effects of irradiation-enhanced creep

The expected creep effect is to relax any stress state during an operational scenario inside a reactor. The major consequences are [10]:

- Preload stresses—such as those from bolt preloading or residual stress in as-deposited coatings—are almost entirely relaxed after a certain damage threshold. A rule of thumb for austenitic stainless steels is that less than 10% of the initial stress remains after 10 dpa.
- Swelling-gradient-induced stress, arising from spatial variations in dose rate and temperature, is significantly mitigated by corresponding gradients in irradiation creep strain across the material.

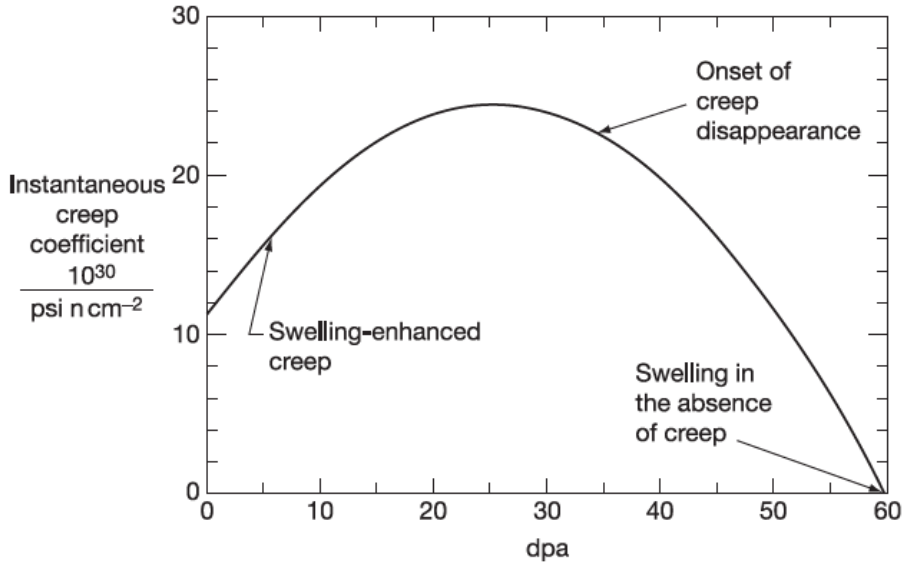

Figure 3.14: Instantaneous creep coefficient (B_0 + D) calculated for high swelling conditions of stainless steel irradiated in a fast reactor [10]

.

- D^{-1} defines the operating stress (in MPa) under swelling-driven conditions, indicating that the internal stress induced solely by restrained swelling cannot exceed $\sim$ 160 MPa.

- Reduction of stress concentrations caused by internal and external sources and, consequently, reduction of potential failures or damages caused by a high stress state condition, such as IASCC, fracture, and cracking.

- Significant stress levels acting continuously on a component will induce a continuous permanent deformation process. The accumulated strain may compromise the component's dimensional stability if the exposure time is sufficiently long.

- If two bonded components exhibit differential swelling and creep behavior, their combined response can lead to structural distortions. While swelling is mechanically restrained at the interface, irradiation creep accommodates the internal stress by redirecting mass flow toward the unconstrained directions.

Unlike thermal creep, irradiation creep does not cause microstructural damage that promotes

material failure, such as triple-point cracks, grain boundary voids, plastic deformation, or martensite formation [10]. Therefore, it reduces stress concentrations by promoting a non-damaging reallocation of internal mass. Also, in higher temperatures where thermal creep is active, irradiation is expected to reduce its harmful effects.

3.4 Ion irradiation as a surrogate for neutron damage

Ion irradiation can be considered a valid surrogate for neutron irradiation if it yields comparable post-irradiation effects to those observed under neutron exposure [8]. The equivalence lies in the ability of ion irradiation to generate qualitatively and quantitatively similar damage, regardless of the irradiation method. When this condition is satisfied, ion irradiation experiments may serve as a direct substitute for neutron irradiation in materials testing and evaluation.

On one hand, several inherent limitations of accelerator-based testing prevent ion irradiation from fully replicating all neutron-induced effects. These include the absence of transmutation gases, the inability to simulate long-term phase transformations, and the micron-scale of ion-irradiated volumes, which may not accurately represent bulk mechanical behavior. Some of these limitations can be mitigated by implementing dual-beam irradiation techniques, such as co-injection of helium (He), or by using neutron pre-conditioned samples. However, dimensional constraints related to small sample volumes remain a significant gap.

On the other hand, ion irradiation has demonstrated excellent agreement with neutron irradiation for certain phenomena, particularly void swelling. Steady-state swelling rates observed in ion-irradiated materials have matched those found in reactor environments, and the temperature shift with varying dpa rates has also translated well to neutron irradiation data. Therefore, although complete equivalence between the two methods is not universally achieved, ion irradiation remains a reliable surrogate in cases where strong correlation is observed.

The establishment of rigorous and accurate accelerator testing protocols is critical to ensuring the reliability of ion beam experimental results. Findings from the TAMU Accelerator Laboratory [4, 5] revealed that swelling data could be significantly suppressed under certain experimental conditions, such as beam rastering or inadequate filtering of carbon contamination. These results

underscore the importance of carefully controlled experimental conditions and the development of standardized ion irradiation procedures tailored to the specific radiation effects under investigation.

Another important procedure that has improved the fidelity of void swelling measurements in ion irradiation studies is the definition of a safe analysis zone [6]. This approach helps mitigate the combined effects of surface artifacts, injected interstitials, and local compositional changes that can distort swelling behavior. As ions penetrate the material, they create a non-uniform damage profile along the depth, illustrated by the white curve in Figure 3.15. However, not all regions in this profile yield reliable swelling data. Near the surface, defect-denuded and surface-affected zones form due to enhanced sink behavior and irradiation-induced artifacts, which suppress void formation. Deeper in the material, excess injected interstitials elevate recombination rates, limiting vacancy availability for void growth. Between these regions lies the safe analysis zone, where swelling behavior more closely reflects that observed under neutron irradiation. This region is critical for extracting meaningful and representative swelling data.

The correspondence between neutron and ion irradiation is not inherently straightforward due to the coupled effects of temperature and damage rate. As a result, the appropriate equivalence conditions must be established individually for each damage mechanism and material system. However, conducting a comprehensive comparison with neutron data is not always necessary. For example, in the evaluation of a new candidate alloy, a practical and confident approach involves irradiating the new material side-by-side with a well-characterized reference alloy whose irradiation response under neutron exposure has already been validated [10]. In such cases, even though specific microchemical and microstructural features must still be assessed, ion irradiation can provide a rapid initial evaluation of the candidate material's improved radiation tolerance. This strategy enables faster screening and integration of new materials into nuclear design, while detailed optimization studies can proceed in parallel.

3.5 Assessing radiation response through accelerator testing

Ion irradiation experiments follow a simplified sequence of steps: atoms are ionized, accelerated, and directed toward a target material. The process begins with an ion source generating the

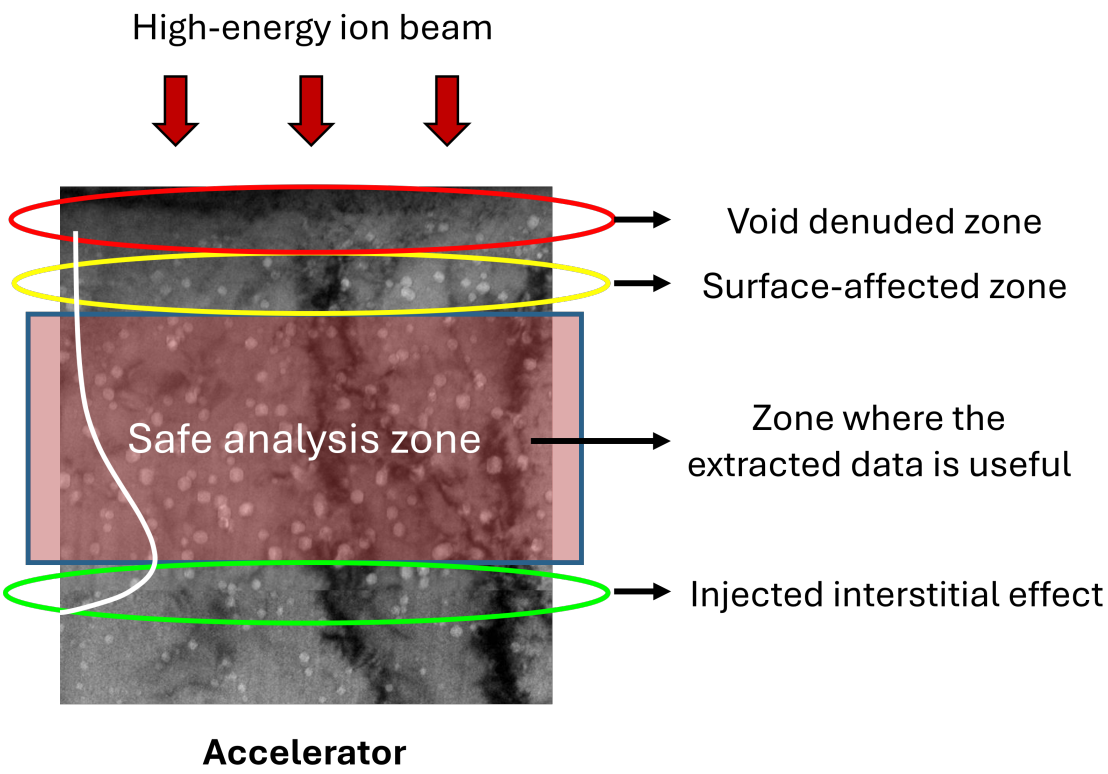

Figure 3.15: TEM micrograph showing the ion-affected zones along the damage profile created by the ions when penetrating the material.

desired ion species, which are then accelerated to high energies—typically in the range of a few mega-electronvolts (MeV), and selectively conducted to ensure beam purity and energy consistency. Upon impacting the target, these ions penetrate the material and transfer their energy to the atomic lattice, initiating displacement cascades and producing radiation damage. Once the desired damage dose is achieved, the sample is removed for microstructural characterization, typically using electron-based microscopy techniques.

Several electron-based microscopy techniques support the detailed characterization of materials' microstructure. Among the primary features examined are dislocation loops, precipitates, and voids, which are typically identified using transmission electron microscopy (TEM) through distinct imaging modes. For instance, for the case of voids, they best revealed using bright-field through-focus or high-angle annular dark-field (HAADF) imaging [1]. To prepare samples for this

analysis, a focused ion beam (FIB) is used to mill a very thin lamella from the irradiated material, oriented along the cross-sectional plane of irradiation to capture the full depth of the damage profile. This precise milling approach enables accurate correlation between the damage gradient and the observed microstructural features.

One of the key advantages of ion irradiation is the precise control it offers over experimental parameters such as dose rate and temperature, enabling systematic investigation of swelling behavior under a wide range of irradiation scenarios. These controlled conditions are essential for generating reliable input data for applications such as risk-informed structural assessments. For each irradiation condition studied, the density and spatial distribution of voids are quantified through a combination of FIB sample preparation and TEM imaging. Post-acquisition image analysis is then conducted to count and measure individual voids, enabling the calculation of void volume fractions.

This systematic workflow, illustrated in Figure 3.16, provides a procedural approach for mapping the swelling behavior of new materials or those with previously uncharacterized irradiation responses. The complete evaluation is structured into three primary stages: a temperature-dependent study, a dose-dependent study, and a dose-rate-dependent study. By compiling the results from all three stages, it becomes possible to estimate the swelling behavior under reactor-relevant operational conditions. These estimations can subsequently be integrated into FEA frameworks to support nuclear safety-related assessments and decision-making processes.

A step-by-step of the three stages to quantify a material swelling behavior is given in the section below.

3.5.1 Void swelling acquisition

Mapping the swelling behavior of materials using ion irradiation can be conducted systematically. For new materials, this can be done in three stages.

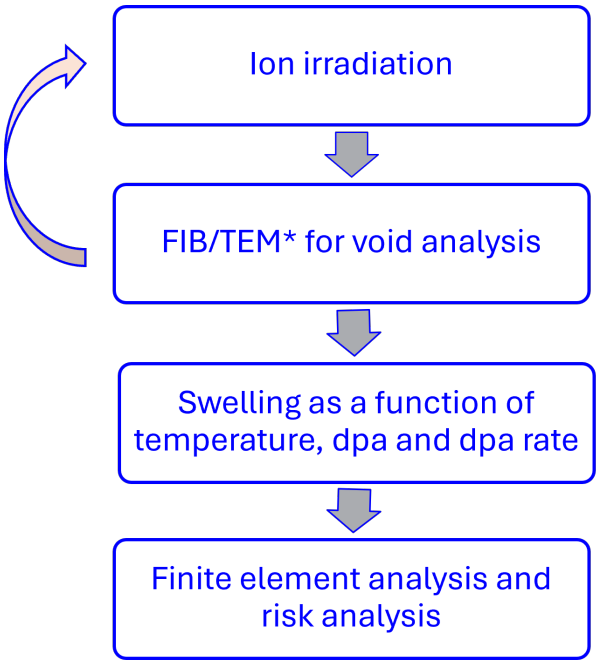

Figure 3.16: Flowchart illustrating the steps of combining ion irradiation testing and finite element analysis for risk assessment.

3.5.1.1 Stage 1: Temperature-dependent Study

The objective of this study is to identify the peak-swelling temperature for a given dose and dpa rate. The steps for this study should follow the suggested ones below:

1. **Define the irradiation experiment matrix**

    - Dose: select a high total dose sufficient to surpass a possible transient swelling phase and reach steady-state conditions.
    - Dose rate: use a high dpa rate to accelerate the experiment.
    - Temperature: base the several temperatures to be investigated, for instance five conditions, on the material's melting temperature T_m:
        - General range: 0.3 - 0.6 T_m
        - BCC materials: usually between 0.3 - 0.4 T_m, with typically swelling starting at $\sim$ 0.2 T_m [11]

- FCC materials: usually between 0.4 - 0.5 T_m, with typically swelling starting at $\sim$ 0.3 T_m [11]

2. **Conduct ion irradiation**

   - Irradiate samples at the defined matrix.

3. **Analyze swelling response**

   - Lift out FIB samples far from the free surface and injected interstitial zone.
   - Characterize microstructure using TEM.
   - Calculate the depth profile void diameter and density for different temperatures.
   - Calculate void swelling and determine the temperature corresponding to maximum swelling.

3.5.1.2 Stage 2: Dose-dependent study

Here, the investigation should focus on identifying the transition between swelling phases and characteristic steady-state swelling rate. The steps are:

1. **Fix the irradiation temperature and dose rate**

   - Use the same dose rate and the peak-swelling temperature identified in Stage 1.

2. **Vary the dose**

   - Irradiate multiple samples over a range of doses, covering transient and steady-state regimes.
   - Dose selection should also be guided by the anticipated irradiation exposure relevant to the material's intended nuclear application.

3. **Conduct irradiation and swelling evaluation**

   - Repeat the steps 2 and 3 of stage 1.

- Identify where swelling linearly varies with dose.
- Make a linear trend to estimate the steady-state swelling rate.

3.5.1.3 Stage 3: Dose rate-dependent study

The swelling at different dose-rate should be investigated to construct a swelling map and estimate swelling for low-dose-rate applications out of possible accelerator dose rate ranges. The steps are:

1. **Design the dpa rate matrix**
   - Include the dpa rate used in earlier stages.
   - Expand the range to cover very high to low dpa rates (within experimental feasibility).
2. **Set irradiation temperatures**
   - For each dpa rate, select a range of temperatures points convering the shift of the peak-swelling temperatures to lower values.
   - Prioritize temperatures around the expected peak. At this point, slightly deviations of the 0.3–$0.6\,T_m$ range might occur.
3. **Conduct irradiation and swelling evaluation**
   - Repeat the steps 2 and 3 of stage 1.
4. **Construct the swelling map**
   - Compile data into a 2D swelling matrix (dose rate vs. temperature).
   - Plot swelling vs. temperature for each dose rate.
   - Identify/estimate the peak-swelling temperatures for each dpa rate.
5. **Fit and Extrapolate**
   - Apply a fitting model based on the Eq. 3.8 to determine trends.
   - Extrapolate the behavior to lower dpa rates not accessible by ion irradiation.

3.5.2 Irradiation creep acquisition

Irradiation creep is a highly complex phenomenon, making creep testing particularly challenging. Numerous published experimental studies on irradiation effects report ambiguous or even contradictory results. This inconsistency arises because dimensional changes during irradiation are governed by several concurrent processes, including void formation, radiation-stimulated phase transformations, and densification. These mechanisms are often interdependent, complicating the interpretation of experimental data. In many cases, it is difficult to decouple their individual contributions, and highly accurate data processing and analysis are required.

For *in situ* ion irradiation experiments, the complexity increases further. The extremely small thickness of the specimens and the significant temperature gradients induced by the ion beam make it difficult to maintain uniform and stable thermal conditions. Despite these challenges, advancements in experimental techniques are underway to overcome these limitations. Ongoing research has been proposing designs to make irradiation creep measurements more reliable and interpretable [22–24].

3.6 Current results for irradiation damage on Chromium

A key concern in the irradiation performance of Cr for nuclear applications is its short swelling incubation period, particularly under conditions relevant to LWRs. Initial studies conducted in the 1990s using high-dose-rate experiments revealed that Cr exhibits a brief incubation phase of approximately 1–2 dpa at elevated temperatures between 550 and 800°C [16]. More recent evaluations of Cr as a coating material for ATF applications, such as the study by Doyle et al. in a research reactor, showed that Cr begins to swell at much lower doses, around 0.5 dpa, under LWR-relevant temperatures. This poor swelling resistance shows a deviation from the typical BCC crystal structure's behavior, characterized by good swelling resistance. Consequently, it poses several risks for coated cladding systems, as it may: (1) the induction of detrimental stress at the substrate–coating interface, (2) geometric instability of the protective layer, (3) increased likelihood of coating cracking or delamination, and (4) the early onset of property degradation such as irradiation hardening

and embrittlement.

To advance the characterization of chromium swelling behavior, two ion irradiation studies were systematically conducted at TAMU [16, 26], aiming to map the effects of temperature and dose on Cr swelling. The first study, performed by Ryabikovskaya et al. [26], corresponded to the stages 1 and 2 described in Section 3.5.1. Five irradiation temperatures were explored, 450, 500, 550, 600, and 650°C, with the peak swelling temperature identified at 550°C.

The dose-dependent investigation included samples irradiated to peak doses of 50, 100, and 150 dpa. Swelling measurements were performed across different depth intervals but were considered valid only within a defined safe analysis zone, ranging from 200 to 600nm in depth. This region was selected according to the best ion irradiation practices to ensure measurement reliability. Within this zone, the dose rate was approximately 3.5×10^{-3} dpa/s, providing a uniform damage distribution and minimizing the influence of near-surface effects and ion end-of-range artifacts.

At the highest dose levels, a well-defined void superlattice was observed, aligned along the $\langle 111 \rangle$ crystallographic direction, consistent with the known tendency of BCC materials to form ordered void arrays under irradiation [11].

The steady-state swelling rate ranged between 0.03 and 0.04 %/dpa, approximately an order of magnitude lower than the typical values observed for other BCC metals, generally between 0.1 and 0.5 %/dpa. A more recent ion irradiation study conducted by Cui et al. [27] at the same irradiation temperature but under a slightly lower dose rate further explored this behavior. The study identified the formation of nested vacancy and interstitial loops and proposed this microstructural feature as a key factor contributing to the reduced swelling rate in Cr. These nested loops are believed to enhance local defect recombination and annihilation processes, thereby suppressing the overall swelling rate.

The second study was carried out by Gabriel et al. [16], focusing on the dose-rate-dependent analysis (stage 3) to evaluate swelling behavior and determine applicable swelling rates for in-reactor dose conditions. Compared to the previous work, this study expanded the irradiation matrix by incorporating two additional lower dose rates and a reduced irradiation temperature of 350°C.

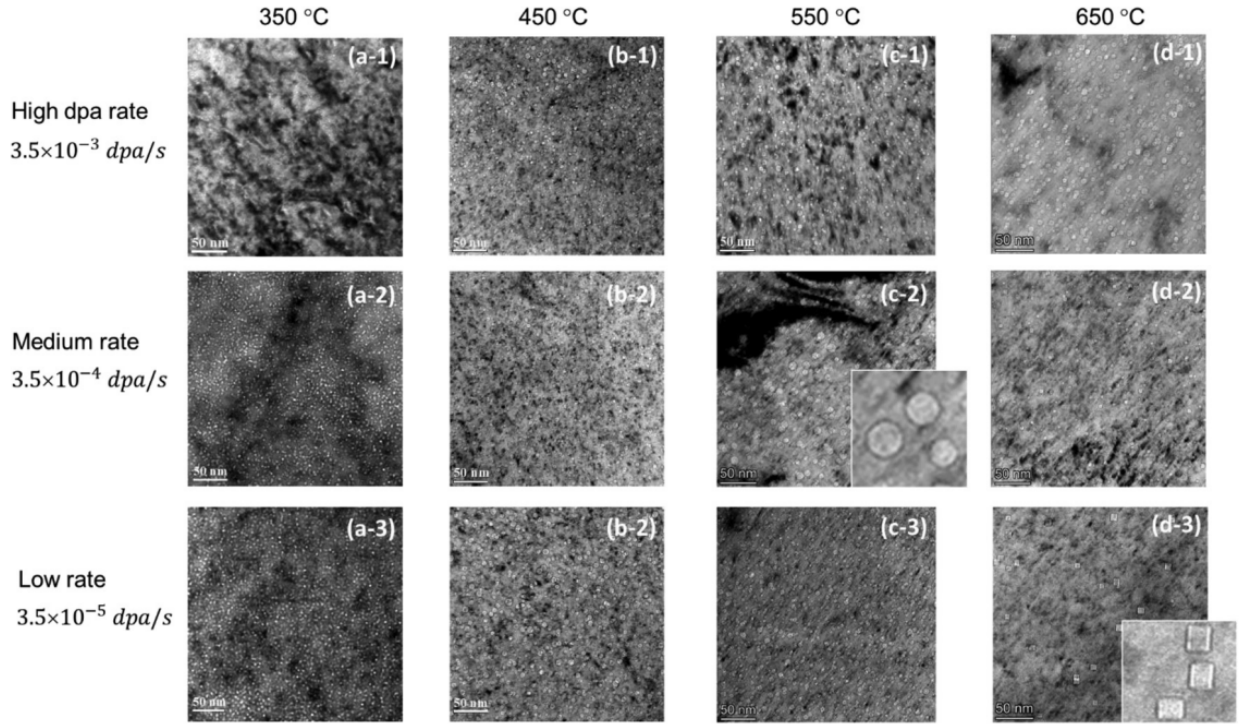

Figure 3.17: TEM image of Cr irradiated by 5 MeV Fe ions at (a-1) 350 °C using a high dpa rate of 3.5 x 10^{-3} dpa/s, (a-2) 350 °C using a medium dpa rate of 3.5 x 10^{-4} dpa/s, (a-3) 350 °C using a low dpa rate of 3.5 x 10^{-5} dpa/s, (b1-b3) 450 °C using three different dpa rates, (c1-c3) 550 °C using three different dpa rates, and (d1-d3) irradiation at 650 °C using three different dpa rates [16].

The experimental matrix thus comprised three dose rates, $3.5\times\ 10^{-3}$, $3.5\times\ 10^{-4}$, and $3.5\times\ 10^{-5}$ dpa/s, combined with six different temperatures.

The two orders of magnitude variation in dose rate was considered sufficient to capture the temperature shift associated with peak swelling behavior. A maximum irradiation dose of 15 dpa was selected to encompass the full range of swelling levels relevant to LWR fuel rod applications. One limitation of this methodology was the extended irradiation duration required for the lowest dose rate; at 3.5×10^{-5}dpa/s, the exposure lasted approximately 120 hours. Figures 3.17 and 3.18 summarize the swelling behavior of Cr as a function of dose rate and temperature, with all reported values obtained from the safe analysis zone defined in [16].

The bright field TEM images in Figure 3.17 gives a general idea of the voids distribution. For lower temperatures, the voids density is higher but with smaller diameters, as illustrated by Figure

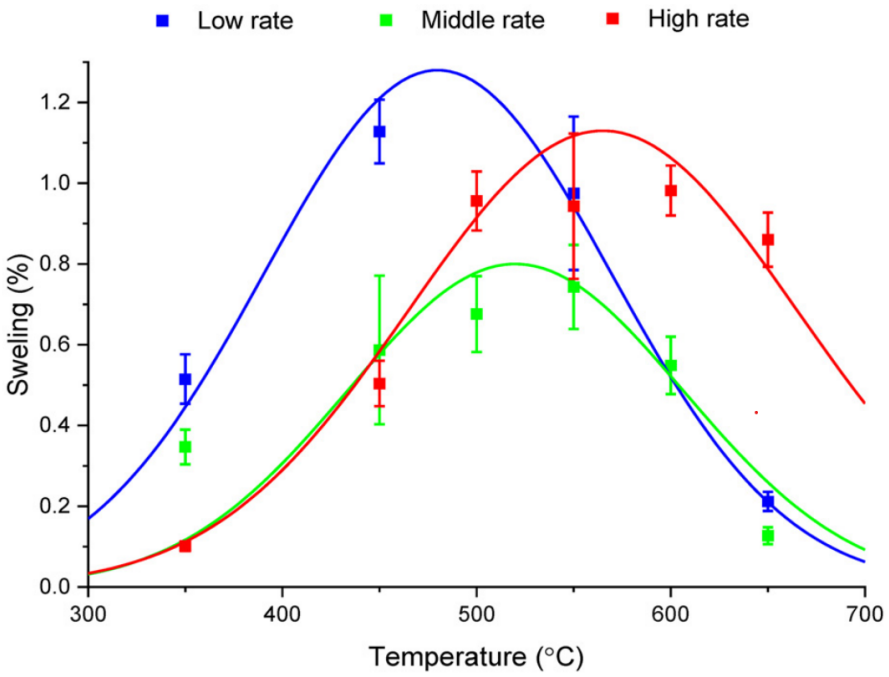

Figure 3.18: Swelling as a function of irradiation temperature for three dpa rates (3.5 x 10^{-3} dpa/s, 3.5 x 10^{-4} dpa/s, 3.5 x 10^{-5} dpa/s). Swelling data is averaged in the safe analysis region [16].

3.17a-2 and a-3. For higher temperature, for instance in Figure 3.17c-2 and c-3, the opposite trend occurs with lower density and large voids, showing the coarsening effect explained in Section 3.3.1.2.

Another notable observation is the transformation in void morphology from near-spherical to faceted, "tetragonal" shapes of voids at lower dpa rates and higher irradiation temperatures. This shape evolution is attributed to sustained atomic mobility at the void surface, which enables the system to minimize surface energy. In crystalline materials, the equilibrium shape of a particle typically conforms to specific crystallographic planes, resulting in faceted particles with directionally dependent morphology. Due to their atomic arrangement, these preferred orientations correspond to planes with lower surface energy.

Under irradiation, however, the continuous production of point defects introduces a non-equilibrium reaction term that drives voids toward a more spherical geometry, counteracting the crystallographically faceted form. As the influence of this irradiation-driven reaction diminishes, such as at lower

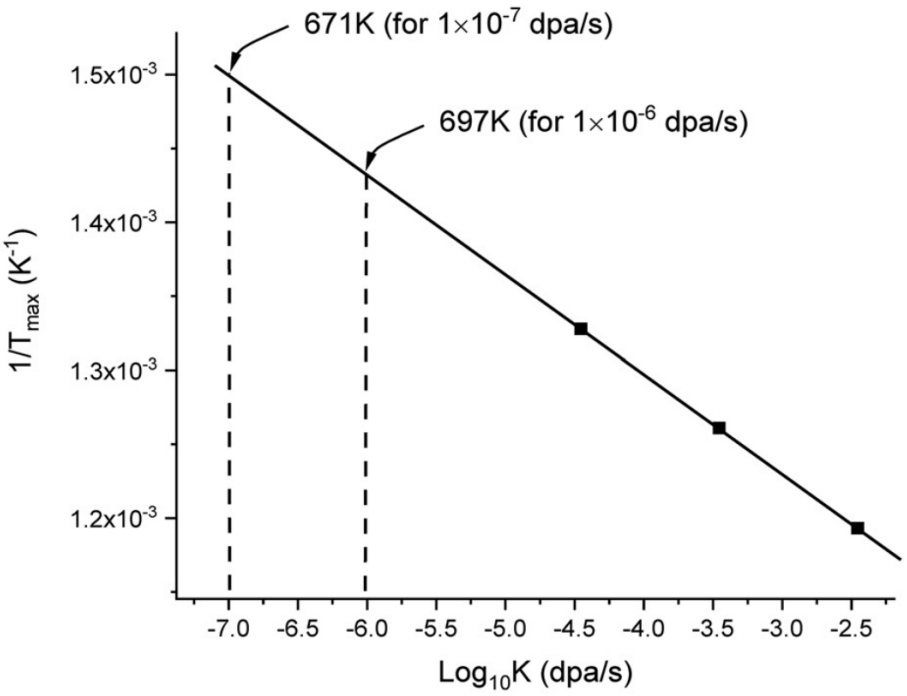

Figure 3.19: The plot of the reciprocal of the maximum swelling temperatures as a function of peak dpa rates in log scale. The solid line is a linear fitting [16].

dose rates or higher temperatures, thermal diffusion becomes sufficient to reorganize vacancy distribution at the void surface. This facilitates reestablishing a surface-energy-minimizing morphology aligned with the underlying crystal structure.

The average swelling within the valid range of the safe analysis zone is presented in Figure 3.18 for all datasets acquired. As the dose rate decreases, a clear temperature shift in the swelling peak is observed toward lower temperatures. Based on Gaussian fits applied to the swelling data, the peak-swelling temperatures are approximately 565, 520, and 480°C for the highest, medium, and lowest dose rates, respectively. In the high and low dose rate cases, the peak swelling values are close to 1%. Notably, the reduced peak height observed for the intermediate dose rate appears to be an experimental artifact. This is likely the result of a trade-off between vacancy diffusivity and irradiation time. At this dose rate, the irradiation duration may have allowed increased diffusion toward the free surface, leading to enhanced vacancy loss and an apparent reduction in measured swelling.

By applying the logarithmic fitting equation (Eq. 3.8) to the peak-swelling temperatures obtained at each dose rate, a linear trend is observed, as shown in Figure 3.19. Extrapolating this trend to typical in-reactor dose rates, ranging from 10^{-8} to 10^{-7}dpa/s, yields projected peak-swelling temperatures between approximately 364°C (637K, not shown in Figure 3.19) and 398°C (671 K). This estimated range aligns closely with the expected operational temperature of Cr-coated cladding in conventional LWRs, suggesting that peak swelling conditions may be active during normal steady-state operation.

Figure 4.5 summarizes the Cr swelling data obtained by both Ryabikovskaya et al. [26] and Gabriel et al. [16] studies (at 550°C and a peak dpa rate of 10^{-3} dpa/second). As explained above, the swelling curve observed is assumed to be close to what would be expected in a PWR environment. The solid line in Figure 4.5 represents the best fit for the dataset, showing a swelling rate trend of 0.05%/dpa. The lowest acquired local dpa value is $\approx$ 5.9 dpa (dashed line). Since the solid line does not pass through the origin, this suggests the existence of a transient swelling region for dpa < 5.9 dpa with higher swelling rates. If one assumed an average rate from the origin to the lowest dpa data point, it would be $\approx$ 0.14%/dpa.

The investigated Cr swelling behavior was done for a bulk material with grains of an average size between 200 and 600 μm, much larger than grains characteristic of coatings structures. Additionally, for some coating deposition methods, like physical vapor deposition (PVD), an elongation of the coating grains towards the out-of-plane direction is expected. These two conditions might change the equilibrium swelling rate magnitude to lower values but not affect the transient regimen much, which is already too short. Therefore, the reported swelling behavior herein might represent the maximum swelling the Cr coating can develop under irradiation.

Cr exhibits a swelling behavior characterized by higher swelling rates during the transient regime than in the steady-state, a reversal of the typical swelling progression outlined in Section 3.3.1.

Table 3.1 summarizes recent findings, showing that average transient swelling rates ($\bar{\dot{S}}$) for Cr exceed the established steady-state value of 0.05 %/dpa by factors ranging from 3 to 8. This

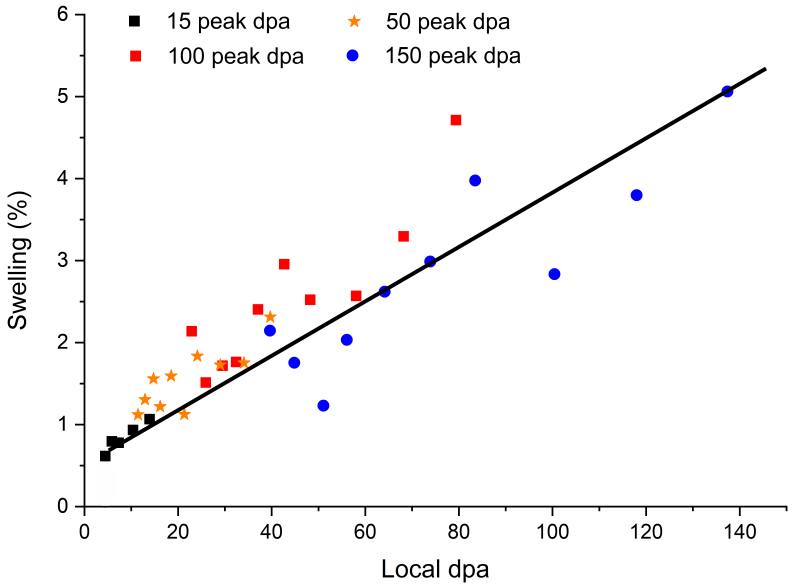

Figure 3.20: Cr swelling as a function of local dpa for irradiation at 550°C, for peak doses of 15, 50, 100, and 150 peak dpa. Linear trend shows a swelling rate of $\sim$ 0.05 %/dpa with the lowest-swelling data point at $\sim$ 5.9 dpa [16].

atypical behavior will induce elevated irradiation creep rates at the beginning of irradiation and accelerated stress relaxation.

Type	Material	Temp.	Dose rate	Dose	S	$\dot{\bar{S}}$	Reference
Neutron	Coating	340 °C	8.8×10^{-8} dpa.s^{-1}	0.5 dpa	0.2 %	0.4 %.dpa^{-1}	[25]
2.8 MeV Fe^{2+}	Bulk	550 °C	2.1×10^{-3} dpa.s^{-1}	3 dpa	0.9 %	0.3 %.dpa^{-1}	[28]
5 MeV Fe^{2+}	Bulk	550 °C	3.5×10^{-3} dpa.s^{-1}	5.9 dpa	0.8 %	0.14 %.dpa^{-1}	[16]

Table 3.1: Cr irradiation data for different experiments showing high swelling rates for low doses.

3.7 Expected Cr coating response

The very short incubation period and elevated transient swelling rates of Cr are expected to generate significant volumetric misfit strain at the onset of normal LWR operation. Given that the substrate constrains the volumetric expansion of the coating, the compressive swelling-induced

stress will enhance irradiation creep mechanisms, thereby promoting substantial relaxation of both swelling-induced and any pre-existing residual stresses. This behavior was experimentally observed by Ribis et al., who reported that the initial residual compressive stress of approximately 410 MPa in as-deposited Cr-coated Zircaloy samples was reversed to a tensile stress of roughly 310 MPa following ion irradiation [29]. This reversal is attributed to stress relaxation occurring at elevated temperatures relative to the temperature at which final stress was measured, indicating that the phenomenon was thermally induced.

The final stress-relaxed state of the coating is inherently time-dependent and cannot be readily calculated due to the simultaneous influence of other stress-generating phenomena, such as swelling, irradiation creep, thermal gradients, and substrate constraints. As a result, drawing reliable conclusions requires the development of a representative numerical model capable of resolving the coupled thermo-mechanical response over time. Such a model should incorporate material-specific properties, swelling, creep behavior, and thermal boundary conditions to simulate the stress evolution with adequate fidelity.

The stress relaxation process occurring in the coating promotes permanent, directional deformation by redistributing mass from the in-plane directions toward the non-constrained out-of-plane direction. If the accumulated strain becomes significant, it may lead to mechanical or geometrical instabilities within the coating. This risk is particularly pronounced for thin coatings, which typically exhibit low strain thresholds for the onset of such instabilities.

The current Cr coating design and proposed evolutionary modifications presented in Chapter 2, such as incorporating a diffusion barrier or alloying with dopants, must be systematically evaluated under irradiation conditions. While interdiffusion is a primary concern at high temperatures, long-term irradiation effects at normal reactor operating temperatures also warrant attention. These include swelling, irradiation-induced creep, and radiation-enhanced diffusion phenomena such as segregation and accelerated interdiffusion. Proton irradiation is a valuable approach for evaluating these combined effects on multi-layered samples, because it has a relatively uniform and deeper damage profile along the irradiation depth profile. This would enable the assessment

of the irradiation-driven interactions among the layers in a fast and reliable way.

3.8 Conclusion

Among the various irradiation-induced damage mechanisms, void swelling poses a particularly detrimental challenge for the Cr-coated cladding design due to notable differences in irradiation response between the coating and the substrate, promoting misfit strains at the interface.

Swelling leads to a non-conservative volumetric expansion, which not only degrades the intrinsic properties of the material but also induces mechanical incompatibilities when the swelling material is externally bonded to another with a dissimilar dimensional response. Over time, the combined effects of swelling and irradiation creep can accumulate significant strains and interfacial stresses, potentially becoming a major source of mechanical degradation. This highlights the critical importance of thoroughly investigating these phenomena.

Ion irradiation has gained increasing reliability through the standardization of accelerator-based procedures and methodologies. Key improvements include: (1) defining a safe analysis zone to minimize surface effects and excess injected interstitials; (2) employing a static, defocused, and non-rastered beam to ensure uniform damage distribution; and (3) reducing carbon contamination by implementing multiple beam deflection techniques. These advances have made ion irradiation a more widely accepted and effective surrogate for emulating neutron-induced damage.

While the irradiation response of Zircaloy is well established within the nuclear materials community, the same cannot yet be said for chromium. Recent systematic ion irradiation studies conducted at TAMU have characterized the swelling behavior of pure chromium, revealing a steady-state swelling rate of approximately 0.05%/dpa, a short transient regime marked by higher swelling rates and a notably short incubation period.

3.9 References

[1] G. S. Was, Z. Jiao, E. Getto, K. Sun, A. M. Monterrosa, S. A. Maloy, O. Anderoglu, B. H. Sencer, and M. Hackett, "Emulation of reactor irradiation damage using ion beams," *Scripta Materialia*, vol. 88, pp. 33–36, 10 2014.

[2] L. Shao, F. A. Garner, A. French, Y. Li, and Z. Hu, "Using ion irradiation for fast simulation of reactor neutron damage: Credibility, issues, and mitigation," Lecture notes for *Fundaments of Ion-Solid Interactions* (Spring 2024), 2024, class material.

[3] G. S. Was and R. S. Averback, "Radiation damage using ion beams," *Comprehensive Nuclear Materials: Volume 1-5*, vol. 1-5, pp. 195–221, 1 2012. [Online]. Available: https://www.sciencedirect.com/science/article/abs/pii/B9780080560335000070?via%3Dihub

[4] J. G. Gigax, E. Aydogan, T. Chen, D. Chen, L. Shao, Y. Wu, W. Y. Lo, Y. Yang, and F. A. Garner, "The influence of ion beam rastering on the swelling of self-ion irradiated pure iron at 450 °C," *Journal of Nuclear Materials*, vol. 465, pp. 343–348, 10 2015.

[5] J. G. Gigax, H. Kim, E. Aydogan, F. A. Garner, S. Maloy, and L. Shao, "Beam-contamination-induced compositional alteration and its neutron-atypical consequences in ion simulation of neutron-induced void swelling," *Materials Research Letters*, vol. 5, pp. 478–485, 11 2017.

[6] Y. Li, A. French, Z. Hu, A. Gabriel, L. R. Hawkins, F. A. Garner, and L. Shao, "A quantitative method to determine the region not influenced by injected interstitial and surface effects during void swelling in ion-irradiated metals," *Journal of Nuclear Materials*, vol. 573, p. 154140, 1 2023.

[7] M. J. Norgett, M. T. Robinson, and I. M. Torrens, "A proposed method of calculating displacement dose rates," *Nuclear Engineering and Design*, vol. 33, pp. 50–54, 8 1975. [Online]. Available: https://www.sciencedirect.com/science/article/pii/0029549375900357

[8] G. WAS, *Fundamentals of Radiation Materials Science: Metals and Alloys*. Springer New York, 2018. [Online]. Available: https://books.google.com/books?id=DM24ugEACAAJ

[9] R. E. Stoller, M. B. Toloczko, G. S. Was, A. G. Certain, S. Dwaraknath, and F. A. Garner, "On the use of srim for computing radiation damage exposure," *Nuclear Instruments and Methods in Physics Research Section B: Beam Interactions*

with Materials and Atoms, vol. 310, pp. 75–80, 9 2013. [Online]. Available: https://www.sciencedirect.com/science/article/pii/S0168583X13005053

[10] F. A. Garner, "Radiation-induced damage in austenitic structural steels used in nuclear reactors," *Comprehensive Nuclear Materials: Second Edition*, pp. 57–168, 1 2020.

[11] A. Bhattacharya and S. J. Zinkle, "Cavity swelling in irradiated materials," *Comprehensive Nuclear Materials: Second Edition*, pp. 406–455, 1 2020.

[12] A. D. Brailsford and R. Bullough, "The rate theory of swelling due to void growth in irradiated metals," *Journal of Nuclear Materials*, vol. 44, pp. 121–135, 8 1972. [Online]. Available: https://www.sciencedirect.com/science/article/pii/0022311572900918

[13] M. Chiapetto, "Modelling of nanostructure evolution under irradiation in iron alloys," Master's thesis, Politecnico di Torino and Grenoble-INP, Italy and France, 2013. [Online]. Available: https://roma.sckcen.be/ws/portalfiles/portal/4559770/Modelling_of_nanostructure_evolution_under_irradiation_in_iron_alloys.pdf

[14] L. K. Mansur, "Theory and experimental background on dimensional changes in irradiated alloys," *Journal of Nuclear Materials*, vol. 216, pp. 97–123, 10 1994. [Online]. Available: https://www.sciencedirect.com/science/article/pii/0022311594900094?via=ihub

[15] F. A. Garner, M. B. Toloczko, and B. H. Sencer, "Comparison of swelling and irradiation creep behavior of fcc-austenitic and bcc-ferritic/martensitic alloys at high neutron exposure," *Journal of Nuclear Materials*, vol. 276, pp. 123–142, 1 2000.

[16] A. Gabriel, L. Hawkins, A. French, Y. Li, Z. Hu, L. He, P. Xiu, M. Nastasi, F. A. Garner, and L. Shao, "Effect of dpa rate on the temperature regime of void swelling in ion-irradiated pure chromium," *Journal of Nuclear Materials*, vol. 561, p. 153519, 4 2022.

[17] E. R. Gilbert and F. A. Garner, "The influence of cold-work level on the irradiation creep and swelling of aisi 316 stainless steel irradiated as pressurized tubes in the ebr-ii fast reactor,"

Journal of Nuclear Materials, vol. 367-370, pp. 954–959, 8 2007. [Online]. Available: https://www.sciencedirect.com/science/article/pii/S002231150700517X

[18] S. J. Zinkle and G. S. Was, "Materials challenges in nuclear energy," *Acta Materialia*, vol. 61, pp. 735–758, 2 2013. [Online]. Available: https://www.sciencedirect.com/science/article/pii/S1359645412007987

[19] S. M. Bruemmer, E. P. Simonen, P. M. Scott, P. L. Andresen, G. S. Was, and J. L. Nelson, "Radiation-induced material changes and susceptibility to intergranular failure of light-water-reactor core internals," *Journal of Nuclear Materials*, vol. 274, pp. 299–314, 9 1999. [Online]. Available: https://www.sciencedirect.com/science/article/pii/S0022311599000756

[20] O. K. Chopra and A. S. Rao, "A review of irradiation effects on lwr core internal materials – neutron embrittlement," *Journal of Nuclear Materials*, vol. 412, pp. 195–208, 5 2011.

[21] F. Onimus, T. Jourdan, C. Xu, A. A. Campbell, and M. Griffiths, "Irradiation creep in materials," *Comprehensive Nuclear Materials: Second Edition*, pp. 310–366, 1 2020. [Online]. Available: https://www.sciencedirect.com/science/article/abs/pii/B9780128035818116455?via%3Dihub

[22] C. Xu and G. S. Was, "In situ proton irradiation creep of ferritic–martensitic steel t91," *Journal of Nuclear Materials*, vol. 441, pp. 681–687, 10 2013. [Online]. Available: https://www.sciencedirect.com/science/article/pii/S0022311513005497

[23] S. A. Briggs, M. Steckbeck, N. M. Heckman, T. A. Furnish, D. C. Bufford, D. Buller, B. L. Boyce, and K. Hattar, "A combined thermomechanical and radiation testing platform for a 6 mv tandem accelerator," *Nuclear Instruments and Methods in Physics Research Section B: Beam Interactions with Materials and Atoms*, vol. 509, pp. 39–47, 12 2021. [Online]. Available: https://www.sciencedirect.com/science/article/pii/S0168583X2100344X

[24] B. Moore, M. Topping, R. Guo, T. Feuerstake, C. McDonald, and M. R. Daymond, "The design and implementation of an in-situ mechanical loading apparatus used during

proton-irradiations," *Journal of Nuclear Materials*, vol. 583, p. 154529, 9 2023. [Online]. Available: https://www.sciencedirect.com/science/article/pii/S0022311523002969

[25] P. J. Doyle, T. Koyanagi, C. Ang, L. Snead, P. Mouche, Y. Katoh, and S. S. Raiman, "Evaluation of the effects of neutron irradiation on first-generation corrosion mitigation coatings on sic for accident-tolerant fuel cladding," *Journal of Nuclear Materials*, vol. 536, p. 152203, 8 2020. [Online]. Available: https://www.sciencedirect.com/science/article/pii/S0022311520302051?via%3Dihub

[26] E. Ryabikovskaya, A. French, A. Gabriel, H. Kim, T. Wang, K. Shirvan, F. A. Garner, and L. Shao, "Irradiation-induced swelling of pure chromium with 5 MeV Fe ions in the temperature range 450–650 °C," *Journal of Nuclear Materials*, vol. 543, p. 152585, 1 2021.

[27] L. Cui, Y. Du, H. Yang, R. E. Schäublin, Y. Zongda, S. Kano, X. Hu, and H. Abe, "Nested loops explain low irradiation-induced swelling rate," *Acta Materialia*, vol. 267, p. 119700, 4 2024. [Online]. Available: https://www.sciencedirect.com/science/article/pii/S1359645424000533

[28] L. J. Cui, H. L. Yang, Y. F. Du, Q. Q. Shi, S. Kano, and H. Abe, "Tem characterization of irradiation-induced dislocation loops and voids in ion-irradiated pure chromium," *Journal of Nuclear Materials*, vol. 569, p. 153920, 10 2022. [Online]. Available: https://www.sciencedirect.com/science/article/pii/S0022311522004068?via%3Dihub

[29] J. Ribis, A. Wu, R. Guillou, J.-C. Brachet, C. Baumier, A. Gentils, and M. Loyer-Prost, "Radiation-induced sharpening in cr-coated zirconium alloy," *Materials*, vol. 15, 2022. [Online]. Available: https://www.mdpi.com/1996-1944/15/6/2322

4. MULTISCALE MODELING: COMBINING ION IRRADIATION AND FINITE ELEMENT ANALYSIS TO ASSESS THE EFFECT OF SWELLING ON CR-COATED CLADDING[1]

4.1 Introduction

Cr experiences void swelling under neutron irradiation, which can lead to stress buildup when bonded to Zircaloy, a material resistant to swelling at LWR-relevant temperatures. This stress arises primarily from the mismatch in the swelling behavior of Cr and Zircaloy. Another significant contribution to interfacial stress comes from differences in their thermal expansion. Moreover, irradiation creep plays an important role in relieving these stresses during reactor operation at elevated temperatures, reducing the likelihood of immediate failure. However, at lower temperatures, such as during refueling, a sudden reversal in interfacial stress is expected, arising from differences in thermal expansion. This corresponds to a situation where both swelling and creep-related dimensional changes exist, while thermal expansion-induced dimensional changes are reduced, potentially leading to interface failure.

Ion irradiation has been widely used as a surrogate for neutron irradiation due to its lower cost and higher damage introduction rate [1–3]. Although various neutron-atypical factors can be introduced during ion irradiation, such as surface effects and injected interstitial effects, methods have been developed to quantitatively predict the safe analysis zones where swelling data are reliable and self-consistent [4]. For the injected interstitial effect, the safe zone is slightly deeper than half of the projected range, as derived from an empirical observation in self-ion-irradiated Fe.

Applying ion irradiation, the swelling behavior of Cr during Fe ion irradiation has been previously investigated by our group. In one study by Ryabikovskaya et al. [5], the following observations were made: (1) swelling of Cr has a very small incubation period at negligible dose; (2)

[1]Part of the data reported in this chapter is reprinted or modified with permission from "Ion irradiation and finite element analysis to assess the effect of swelling on Cr-coated cladding" by Artur Santos Paixao, Rijul Chauhan, Zhihan Hu, Frank A. Garner, Michael Nastasi, and Lin Shao, in *Nuclear Instruments and Methods in Physics Research Section B*, 563 (2025) 165702 by Elsevier B.V.

voids in Cr exhibit self-organization producing a superlattice structure; and (3) the swelling rate peaks at 550°C.

In another study by Gabriel et al. [6], swelling obtained at peak dpa rates ranging from 3.5 x 10^{-5} to 3.5 x 10^{-3} dpa/sec exhibited a shift of the maximum swelling temperature as a function of the dpa rate. The maximum swelling temperature shifts downward from 565°C at 3.5 x 10^{-3} dpa/sec to 480°C at 3.5 x 10^{-5} dpa/sec. Extrapolation of the peak temperature curve suggests that the maximum swelling temperature at LWR-relevant dpa rates is around 400°C. Therefore, swelling data obtained at high dpa rates typical of ion irradiation are assumed to be a good simulation of the swelling behavior to be expected in LWR environments.

The swelling data needs to be combined with mechanical property data for safety analysis of coating concepts. In the present study, the swelling data were first compiled after reviewing the experimental procedure used in its derivation. The dpa-dependent swelling curve was then used as input in the FEA to predict the dimensional change of Cr coating as a function of reactor service time. For the study, the FEA was performed using the commercial software Ansys 2023-R2 [7]. The analysis further considered thermal expansion and creep. To accurately represent reactor conditions, the modeling included the pressure buildup in the Zircaloy fuel cladding arising from fission gas release, as published in reactor literature sources [8]. To link the model to fuel performance, this study used published Zircaloy-4 fuel cladding data for a pressurized water reactor. The simulated time period spanned two years, including reactor shutdown for refueling at the end of every 12-month fuel life cycle.

4.2 Experimental Procedure

As discussed in references [5] and [6], Cr of 99.95% purity was cut and polished into pieces with dimensions of 5mm x 5mm x 1mm. Cr samples were first finely polished mechanically using SiC paper and then electropolished with a Tenupol 5 twin-jet electropolisher. The solution contained 5% perchloric acid in methanol and was cooled down to -20 °C during polishing. The polished samples were irradiated with 5 MeV Fe^{+2} ions using a 3 MV NEC tandem accelerator at Texas A&M University. The irradiation temperatures chosen ranged from 450 to 650°C, and

the dose levels ranged from 15 to 150 peak dpa. The 2013 version of the Stopping and Range of Ions in Matter (SRIM) code was used to calculate damage vs. depth profiles [9]. The Kinchin-Pease (KP) mode was used, and the displacement energy of Cr was 40 eV [10]. Fe ions, instead of Cr ions, were used for irradiation since Cr beam currents are not very stable, due to their strong oxygen affinity. The Fe beam passed through multiple beam deflectors to filter out contaminants, especially C, N, and O [11]. To avoid the beam pulsing effect, a static non-focused beam with a spot size of about 6mm x 6mm was used [12]. A liquid nitrogen trap was used to improve the vacuum. The vacuum of the target chamber during the entire irradiation was always 6×10^{-8} torr or better. After ion irradiation, the FIB technique was used to prepare specimens for TEM characterization using a FEI Tecnai F20 STEM with an operating voltage of 200 kV. The void images were analyzed using ImageJ software [13]. Local swelling was calculated using Swelling % = V%/(1-V%), where V% is the volume percentage fraction of voids.

4.3 Modeling Procedure

4.3.1 Swelling

It is feasible to introduce a modified thermal expansion coefficient that accounts for both swelling and thermal expansion effects. One such formula, previously proposed by Lee and Kazimi [14], is given by:

$$\alpha_{modified} = \alpha + \frac{S}{3(T - T_{ref})} \tag{4.1}$$

where α is the thermal expansion coefficient, S is the accumulated swelling level, T is the current temperature, T_{ref} is the reference temperature at which thermal expansion is zero.

This formula effectively links swelling and thermal expansion into a unified model, useful for predicting dimensional changes exposed to arbitrary radiation damage and heated at high temperatures. The 1/3 factor in the second term accounts for the fact that swelling is a three-dimensional phenomenon, while α is a one-dimensional measurement. The term 1/(T - T_{ref}) removes the temperature dependence of swelling, treating it as an athermal dimensional change when applying α

for calculating volume changes.

For the swelling rate $\dot{S}$, two distinct rates were observed: a transient rate of 0.14% per dpa for damage levels $\leq$ 5.9 dpa, and 0.05% per dpa for damage levels $>$ 5.9 dpa. The detailed behavior at the early stages of swelling, such as whether Cr has a swelling incubation period, has only a small effect on the final stress value. This is because the results are 1) more sensitive to the accumulated swelling at high dpa levels and 2) because relaxation of swelling-driven stresses by irradiation creep is proportional to the swelling rate. As a consequence, swelling-driven stresses cannot increase indefinitely and will saturate at a level well below the yield stress, no matter what the swelling rate [15].

Swelling is known to be sensitive to imposed stress states for various alloys and irradiation conditions, usually shortening the incubation period [15], but no information is available for Cr, which has essentially no incubation period, and therefore potential stress effects on swelling will not be considered in this paper.

4.3.2 Irradiation creep

The formulation for a steady-state creep regime has two primary components, one is independent of swelling (B_0), designated as the creep compliance. The second component is much more significant and is directly proportional to the swelling rate. Together, these two components relax the swelling-induced stress state. The creep rate is therefore described by:

$$\dot{\epsilon}_{cr} = \sigma_{eq}(B_0 + D\dot{S}) \tag{4.2}$$

where σ_{eq} is the equivalent stress [15] and D^{-1} defines the operating stress in MPa for a swelling-driven stress state.

For irradiation creep of pure chromium, there is currently no available data from any irradiation environment. However, we can utilize certain universal features observed in other metals during neutron irradiation to develop a reasonable creep formulation. First, the B_0 coefficient appears to scale with the swelling rate in Fe-based alloys, including both face-centered cubic (FCC) and

BCC structures. For example, $B_0 = 1 \times 10^{-6}$ $(MPa.dpa)^{-1}$ is a consistent value observed in several experiments conducted in PWR temperature ranges for austenitic steels [15]. The swelling rate for chromium in the TAMU ion studies is approximately 10 times lower than that of BCC iron alloys and 20 times lower than that of FCC iron alloys. Additionally, the D coefficient, called swelling–creep coupling coefficient, appears to be independent of both metal type and crystal structure, at least in Fe-based alloys [15]. Our estimated coefficients for Cr irradiation creep are provided in Table 4.1.

Zircaloy-4 has a zero swelling rate, which means that its deformation under irradiation primarily results from creep rather than swelling. Thus, the creep compliance term dominates. A different but equivalent empirical formulation for the creep rate of Zircaloy-4 under fast neutron flux and effective stress is given by Equation 4.3 [16]:

$$\dot{\epsilon}_{cr,Zr4} = C_0 \Phi^{C_1} \sigma_{eq}^{C_2} \tag{4.3}$$

where Φ is the fast neutron flux ($n/m^2.s$). The adopted material constants are shown in Table 4.1.

Irradiation creep is orders of magnitude greater than thermal creep at temperatures typically found in the normal operational range of nuclear reactors. Therefore, thermal creep strain rates are negligible in this analysis.

Irradiation creep material constant	Value
Stress Relief Anneal (SRA) Zircaloy-4	
C_0	9.881×10^{-28}
C_1	0.85
C_2	1
Chromium	
B_0	0.05×10^{-6} MPa^{-1} dpa^{-1}
D	0.6×10^{-2} MPa^{-1}

Table 4.1: Irradiation creep constants for Zircaloy-4 and pure Cr.

4.3.3 Irradiation growth

Irradiation growth is a volume-conserving strain process that comes from the inherent anisotropy crystallographic structure (zircaloy); therefore, isotropic structures, such as Cr, do not undergo irradiation growth [17]. However, irradiation growth is strongly affected by cold work (Burgers vectors distribution) and texture, both consequences primarily of tube production. Therefore, it is possible to assume that no dimensional changes on the zircaloy cladding arise from irradiation growth since the strain behavior can vary considerably from heat to heat.

4.3.4 Other Properties of Zircaloy-4

The mechanical properties of Zircaloy-4 undergo significant changes due to neutron irradiation, resulting in increased strength and hardness, along with reduced ductility. The main structural changes behind the hardening are the increase in <a> type dislocation loop density in the early irradiation stage and continuous increase in <c> type loop density without saturation [18]. The strength increases to 600 MPa for the neutron fluence analyzed [18]. The thermal conductivity of Zircaloy-4 is strongly dependent on the temperature, but no dependence on accumulated neutron exposure was observed [19]. Thermal conductivity (W/mK), within the temperature range between 285 and 1770 Kelvin (K), is calculated by [19]:

$$k(T) = 7.51 + 2.09 \times 10^{-2}T - 1.45 \times 10^{-5}T^2 + 7.67 \times 10^{-9}T^3 \tag{4.4}$$

Elastic modulus (Pa), within the temperature range between 293 and 1474 K and considering the effect from accumulated exposure, is calculated by [19]:

$$\begin{aligned} E(T,\Phi) = \quad & \frac{1.088 \times 10^{11} - 5.475 \times 10^{7}T}{c_2} \\ \text{with} \quad & c_2 = 0.88 + 0.12 \times e^{\left(-\frac{\Phi}{10^{25}}\right)} \end{aligned} \tag{4.5}$$

Poisson's ratio is considered nearly temperature independent (ν = 0.41 for Zircaloy-4) [20]. Thermal expansion, within the temperature range between 280 and 1073.15 K is described by

[19]:

$$\epsilon_{axial}(T) = -2.506 \times 10^{-5} + 4.441 \times 10^{-6} \times (T - 273.15) \tag{4.6}$$

$$\epsilon_{circumferential}(T) = -2.373 \times 10^{-4} + 6.721 \times 10^{-6} \times (T - 273.15) \tag{4.7}$$

4.3.5 Other Properties of Cr

The thermal conductivity of Cr (in W/mK) within the temperature range of 300 to 1300 K can be calculated using the formula provided by [21]:

$$k(T) = -2.07 \times 10^{-8}T^3 + 4.85 \times 10^{-5}T^2 - 0.06 \times T + 101.75 \tag{4.8}$$

Elastic modulus (GPa), within the temperature range between 300 and 1300 K, is calculated by [22]:

$$E(T) = -2.5 \times 10^{-5}T^2 - 0.01 \times T + 264.11 \tag{4.9}$$

The Poisson ratio is 0.22 [21], assumed temperature-independent. The thermal expansion coefficient (K^{-1}) for the temperature range between 300 and 2130 K is calculated by [23]:

$$\alpha(T) = 1.22 \times 10^{-5}T - 1.415 \times 10^{-8}T + 1.132 \times 10^{-11}T^2 - 0.507/T^2 \tag{4.10}$$

4.3.6 Finite Element Analysis Simulations

The model simulated the stress evolution of the coated cladding system over a two-year reactor service period, with a time step of one month and refueling life cycles of 12 months. At the end of the simulation, the model accounted for the time involved for reactor refueling at low temperatures. Figure 4.1 illustrates the flowchart of the analysis. A key aspect of the model is incorporating neutron fluence-dependent swelling, alongside thermal expansion effects, to calculate the stress in both the cladding and the Cr coating. This stress triggers creep relaxation, which is factored into the next iteration step of the simulation.

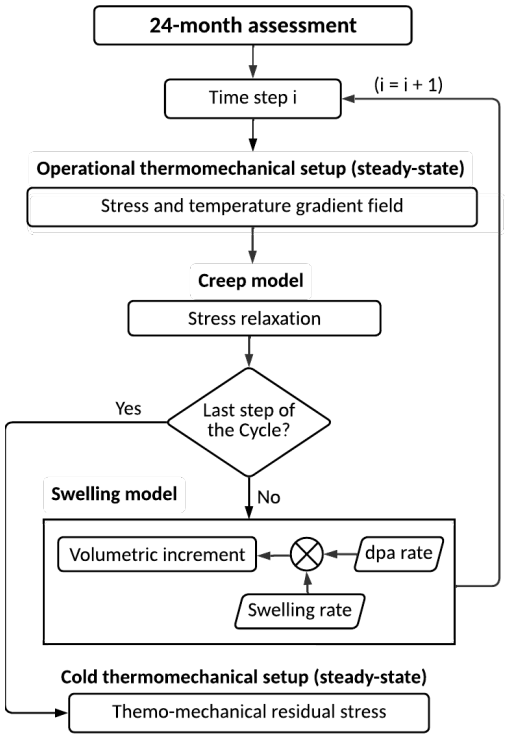

Figure 4.1: Simplified FEA analysis flowchart.

Figure 4.2 shows the schematic of Cr-coated fuel cladding. The vertical dashed line represents the fuel rod and fuel pellet centerline. Fuel-cladding interactions were not modeled in this analysis. The cladding has a through-thickness temperature gradient due to the heat generated by the fuel and the coolant effect on the outside of the fuel pin. This temperature gradient was used to simulate the buildup of thermal stresses. Additionally, the model includes pressure effects from helium cover gas and developing fission gases on the fuel side and from the highly pressurized water on the coolant side. The fuel cladding in this simulation is allowed to expand freely in the vertical direction. The dimensions of the cladding are 5 mm in height and 0.6 mm for the cylindrical wall thickness. The outer diameter of the fuel cladding is 5.27 mm, and the Cr coating thickness is 20 micrometers.

Note that the tube is under an overall compressive state in a “pressurized” water reactor, a stress condition that will be modified somewhat during irradiation cycles but will not be reversed in sign.

The total strain (ϵ_t) in a given position r is the sum of contributions of elastic (ϵ_e) and permanent

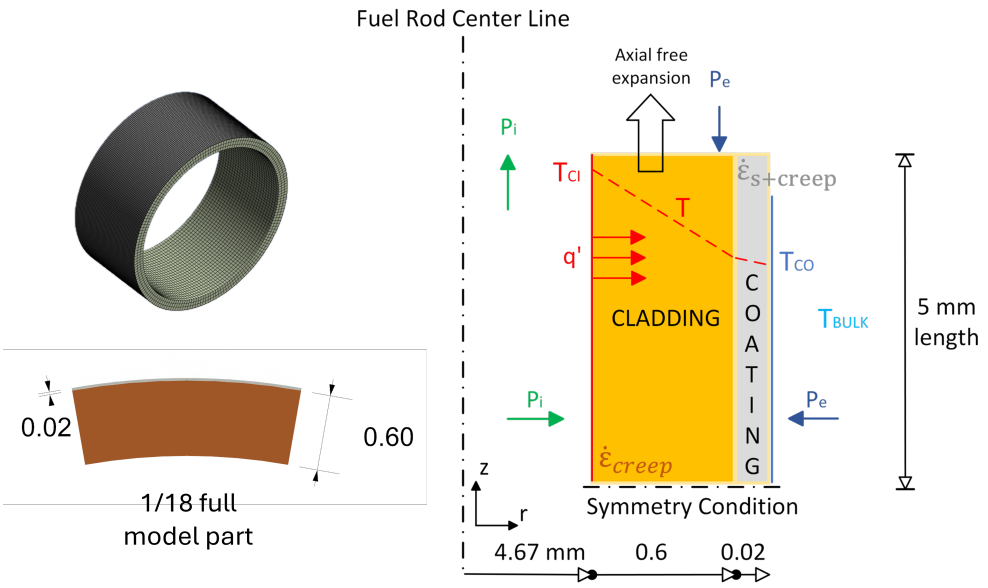

Figure 4.2: Schematics of Cr-coated Zircaloy-4 tubes for the simulations.

(ϵ_p) strain components (as described by Equation 4.11). The elastic deformation comes from the thermal (ϵ_{th}) and mechanical (ϵ_m) loads (as described by Equation 4.12). The permanent strain arises from the irradiation-induced swelling (ϵ_s) and irradiation creep (ϵ_c). (as decribed by Equation 4.13). Previous studies have shown that both FEA and analytical solutions were in good agreement for predicting these strain components [14, 24].

$$\epsilon_t(r) = \epsilon_e(r) + \epsilon_p(r) \tag{4.11}$$

$$\epsilon_e(r) = \epsilon_{th}(r) + \epsilon_m(r) \tag{4.12}$$

$$\epsilon_p(r) = \epsilon_s(r) + \epsilon_c(r) \tag{4.13}$$

Regarding the reactor conditions, both the operational and refueling conditions are based on literature data available for a typical PWR [8, 25–28], as listed in Table 2. The assumed damage rate of $\sim$ 5 dpa/yr for the modeled fuel pin, leading to total neutron damage of 10 dpa after a 2-year operation, is within typical damage rates for in-core components. The damage conversion factor used for LWRs is $\sim$14 dpa per 10^{26} n/m^2 (E $>$ 1.0 MeV) [15], leading to $\sim$ 4.4 dpa/yr, with an

acceptable variation of up to 15% due to spatial variations across the core. Current cases of in-core damage level at the last refueling outage (after two cycles) can reach up to 20 dpa at a burnup of 40 GWd/tU, considering that newer generations of LWR reactors have been increasing their burnup levels up to 60 GWd/tU at end of life (EOL) [29].

Our simulation does not consider any residual stress from the coating process, assuming that the Cr layer is relaxed at the very beginning. In reality, residual stress exists and varies depending on the coating method. Therefore, the present modeling assumes ideal deposition coating conditions.

Parameter	Value	Reference
Linear heat generation (Uniform)	200 W/cm	[8]
Fast neutron flux (E $>$ 1 MeV)	9.5×10^{17} n/m^{2}s	[8], [25]
Dpa rate	1.61×10^{-7} dpa/s	-
Operating cooling pressure	15.5 MPa	[8]
Operating cooling temperature	307 °C	-
Operating convection coefficient	30 kW/m^{2}K	[26]
Refueling coolant pressure	0.1 MPa	-
Refueling cooling temperature	75 °C	[27]
Refueling convection coefficient	0.5 kW/m^{2}K	[28]
Rod fill gas	Helium	[8]
Fill gas initial pressure	2.0 MPa	[8]
Fill gas operational pressure range	4-6.85	[8]
Clad emissivity	0.8	[8]

Table 4.2: Assumed operating and refueling conditions (FEA analysis input data).

4.4 Results and Discussion

Figure 4.3 shows a typical cross-sectional bright field TEM image of Cr irradiated to a peak dose of 15 dpa at 550°C. Void sizes range from 2 to 10 nm. Figure 4.4 plots the swelling as a function of depth, with the solid line representing the SRIM-obtained dpa profile. The dpa values peak at a depth of approximately 1.2 microns. Overall, swelling shows a strong correlation with local dpa values, increasing as dpa increases. Due to the combined effects of compositional changes and injected interstitials from Fe implants, swelling data around the peak damage region

cannot be used [4]. Only the data from the region between 0.3 microns and 0.9 microns was considered to be valid to reactor irradiation.

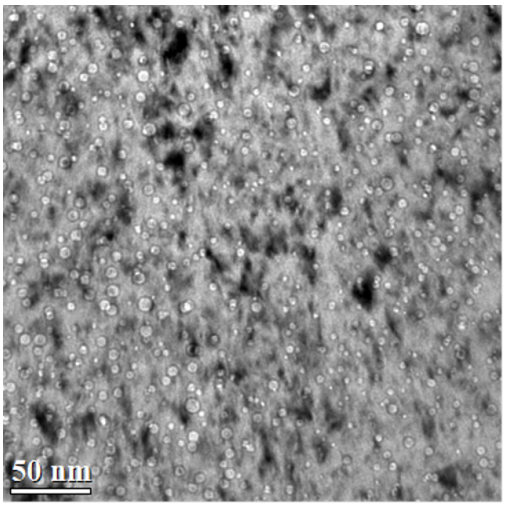

Figure 4.3: Cross-sectional TEM image of Cr irradiated to 15 peak dpa at 550°C, showing a high density of voids.

Void swelling is affected by the injected Fe implants, both due to local composition changes and the injected interstitial effect. The Fe projected range is about 1.4 microns. To avoid suppressed swelling near the Fe projected range, the extraction of swelling data is limited to depths shallower than 1.1 microns.

Figure 4.5 summarizes the swelling data obtained at 550°C and a peak dpa rate of 10^{-3} dpa/second. Both the irradiation temperature and the dpa rate are much higher than those typically found in light water reactors. However, as mentioned in the introduction, these two parameters introduce compensating effects. According to the temperature-shift model [30], reducing the dpa rate would shift the swelling profile to a lower temperature. Consequently, the swelling curve observed here is assumed to be close to what would be expected in a PWR environment. The solid line in Figure 4.5 represents the best fit for the data set, showing a swelling rate trend of 0.05%/dpa. The lowest acquired local dpa value is $\approx$ 5.9 dpa. Since the solid line does not pass through the origin, it suggests the existence of a transient swelling region for dpa $<$ 5.9 dpa with higher swelling rates. If

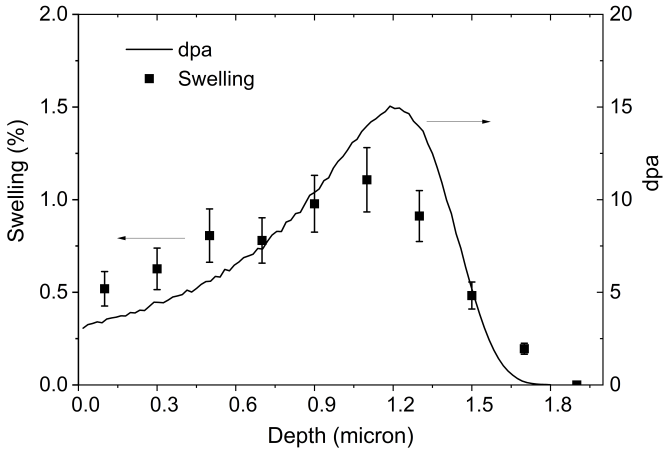

Figure 4.4: Void swelling profile in Cr irradiated to 15 peak dpa at 550°C. The solid line is the SRIM predicted dpa profile for 5 MeV Fe^{+2} ions incident on pure Cr.

one assumed an average rate from the origin to the lowest dpa data point, it would be $\approx 0.14\%$/dpa.

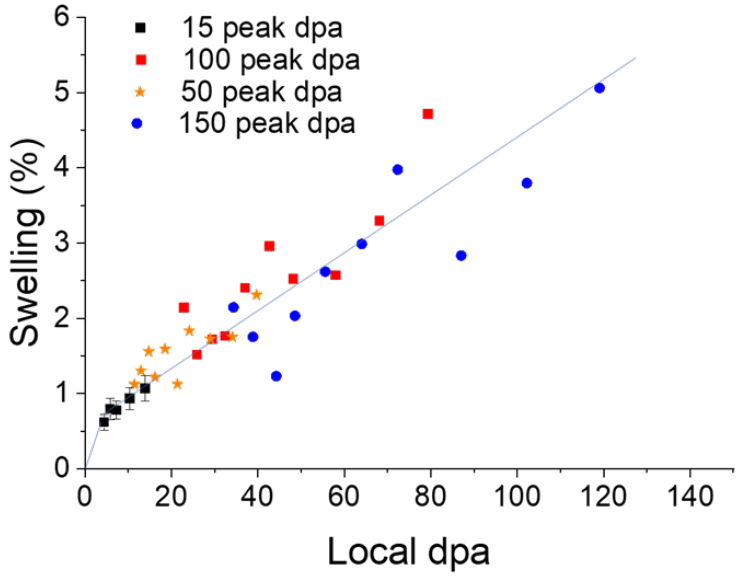

Figure 4.5: Swelling as a function of local dpa for irradiation at 550°C, for four irradiations with peak doses of 15, 50, 100, and 150 peak dpa.

Figures 4.6 and 4.7 compare the hoop and longitudinal stress components across the cladding at the beginning of reactor operation, at operating temperature but at zero dpa, for two conditions

(no coating vs. coated). The black dot line is the calculated temperature profile. The thermal stress arises from a combination of the temperature gradient and the thermal expansion difference between the Cr coating and the Zircaloy-4 substrate, both of which are dependent on local temperatures. The simulation corresponds to the beginning of the operation with P_i = 4.5 MPa (pressure from the fuel side) and P_e = 15.5 MPa (pressure from the coolant side, as marked in Figure 4.2).

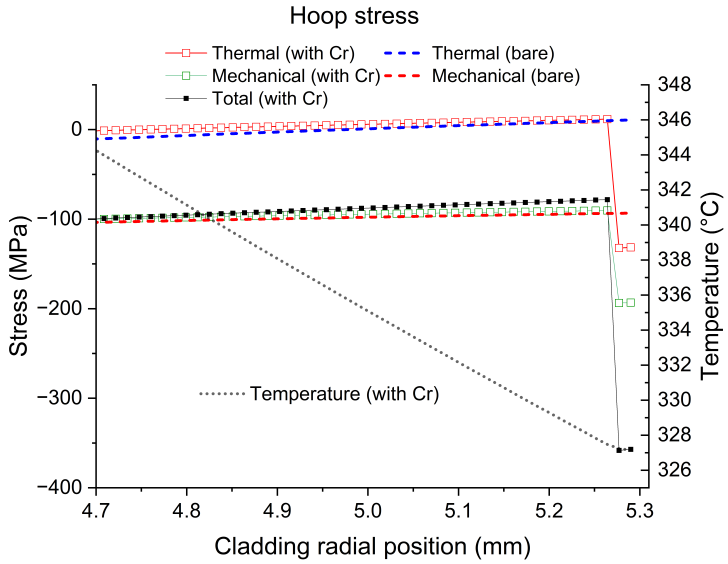

Figure 4.6: Hoop stress as a function of position in Zircaloy cladding with or without Cr coating. The black dot line represents the temperature profile. The thermal stress arises from both the temperature gradient and the thermal expansion difference (for the coated system). The mechanical stress arises from the boundary conditions (from the fuel pellet side and the coolant side). The black squares represent the combined total stress.

The comparison between the red square (coated system) and the blue dashed line (non-coated system) indicates an increase in stress due to the thermal expansion difference between Cr coating and Zircaloy-4. In both Figures 4.6 and 4.7, the Cr coating experiences compressive stress, whereas the Zircaloy-4 tube near the interface experiences a small tensile stress. Note that the coated system and the non-coated system are set to have the same thickness. Hence, the last two points in Figs. 4.6 and 4.7 for the coated system correspond to the stress in the Cr coating. Additionally, the

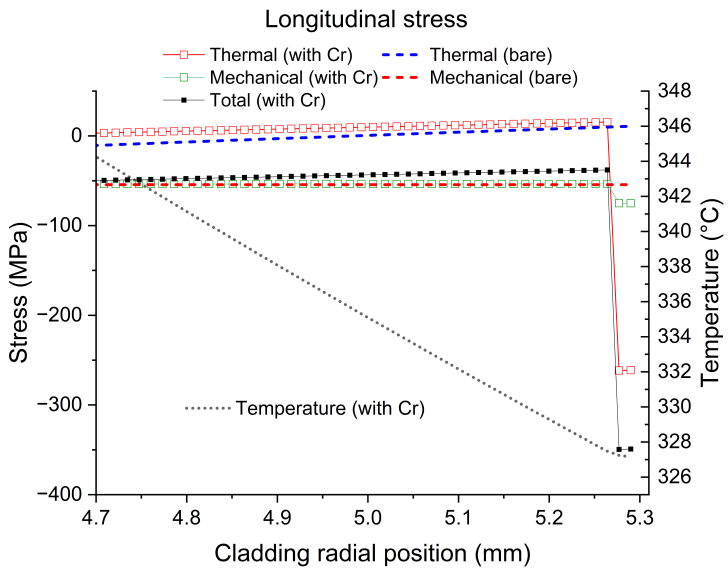

Figure 4.7: Longitudinal stress as a function of position in Zircaloy cladding with or without Cr coating. The black dot line represents the temperature profile. The black squares represent the combined total stress.

anisotropic thermal expansion of Zircaloy-4 produces higher stress in the axial direction. Radial stresses are not shown because they are negligibly small compared to the axial and circumferential stresses.

Regarding the mechanical stress due to pressure boundary conditions, the coated system shows slightly lower stress compared to the non-coated system in hoop stress and almost no difference in longitudinal stress. The cladding temperature at the outer boundary is about 327°C, while the inner temperature is around 346°C. Overall, the temperature gradient is small, and the thermal stress is minor. However, the stress induced by the thermal expansion coefficient difference is significant, as indicated by the large compressive stress in the Cr coating.

here

Figures 4.8 and 4.9 compare the time-dependent stress evolution in the Cr coating under different modeling conditions. Note that the simulated time period for both figures spans two years, ending with shutdown for reactor refueling after 12 and 24 months. The black squares represent the hoop stress, and the red circles represent the longitudinal stress when both swelling and creep

are considered. Figure 4.8a compares the cases with and without swelling included. Figure 4.8b is the enlarged figure showing details close to the end of the reactor shutdown for refueling after 12 months. Figure 4.9a compares the cases with and without creep included, with the same enlarged details at the end of the reactor shutdown shown in Figure 4.9b.

Initially, without irradiation damage, the Cr coating starts with compressive stress due to thermal expansion and elastic modulus mismatch with Zircaloy-4. The stress gradually reduces with irradiation creep but remains compressive until the end. At 14 months, corresponding to 5.9 dpa, the swelling rate reduces to the steady-state value. This change affects the relaxed stress levels, causing them to stabilize at different values. The maintenance of these stress states is a balance between the buildup of stress due to swelling and the process of irradiation creep. While the increase in stress is proportional to the swelling rate, the creep rate depends on both the level of stress and the swelling rate. Therefore, as the swelling rate decreases, the significance of creep relaxation becomes less pronounced. At every shutdown, the Cr film suddenly exhibits a pronounced spike in tensile interfacial stress due to the temperature change, dropping to 76.5°C. The hoop and longitudinal stress spikes shown in Figures 4.8a and 4.9a are for shutdowns after 12 and 24-month operational times, respectively. The highest level of stress spike is expected to occur during the first recycling outage, $\approx$200 MPa for both hoop and longitudinal stresses. The abrupt change in interfacial stress, combined with accumulated irradiation damage defects and associated hardening in both metals, could trigger failures, such as transverse cracks or interfacial delamination [31].

One interesting observation in Figure 4.8 is the comparison of stress with and without swelling. If swelling is not considered, and therefore the Cr creep rate is constituted only by the low rate of the creep compliance term in Equation 2, the stress is much more compressive. Lee *et al.* obtained similar results showing the stress build-up at the interface due to differences in the cladding and coating creep rates [24]. The effect of swelling is complex. While the volumetric expansion caused by swelling exacerbates the dimensional mismatch between the Cr coating and the substrate, as shown in Equation 1, it also increases the creep rate, as shown in Equation 2, thereby accelerating the creep relaxation of the Cr coating. These combined (or competing) effects ultimately result in

a reduction of compressive stress when swelling is considered. Thus, swelling is, to some extent, beneficial in reducing the possibility of delamination.

As for the role of creep, Figure 4.9 a shows that creep plays a significant role in stress relaxation, as expected. Without creep, both hoop and longitudinal stresses drop significantly into negative values. Similarly, these stress levels, represented by the blue and green triangle curves in Figure 4.9a, have a slight change in slope at around 14 months caused by the change in the swelling rate. Throughout the operation period, the compressive stress in the Cr coating begins to decrease as creep is activated, indicating that power operation itself is not a significant concern in terms of material failure (e.g., buckling or delamination). The final interfacial stress is primarily determined by the cladding thermo-mechanical condition at the end of the cooldown and is insensitive to the cooling rate (within the range typical of realistic reactor operation). This is because creep relaxation during the cooling process is negligible due to the relatively short cooldown period. The simulations consider realistic cooling rates, assuming the cooling process is completed in approximately one day.

The in-plane stress distributions in the coating–cladding system at the beginning and at the end of the cool-down process during the first refueling outage are depicted in Figure 4.10. Figures 4.10a and c represent the stress state under operational thermo-mechanical conditions, while Figures 4.10b and d correspond to typical outage conditions—ambient pressure and reduced temperatures—as detailed in Table 4.1. Within the coating, no significant stress gradient is observed, primarily due to its thin geometry. A similar condition is found at the beginning of operation, as shown in Figures 4.6 and 4.7. In contrast, the cladding exhibits noticeable stress gradients as a result of the imposed thermo-mechanical conditions. After 12 months of operation (Figures 4.10a and c), the stress levels in the cladding are not significantly reduced from their initial values, indicating limited stress relaxation due to the relatively low stress environment during operation. Conversely, the coating undergoes more substantial relaxation, driven by the complex interaction between differential creep and swelling behaviors, which results in higher stress magnitudes and enhanced creep deformation capacity.

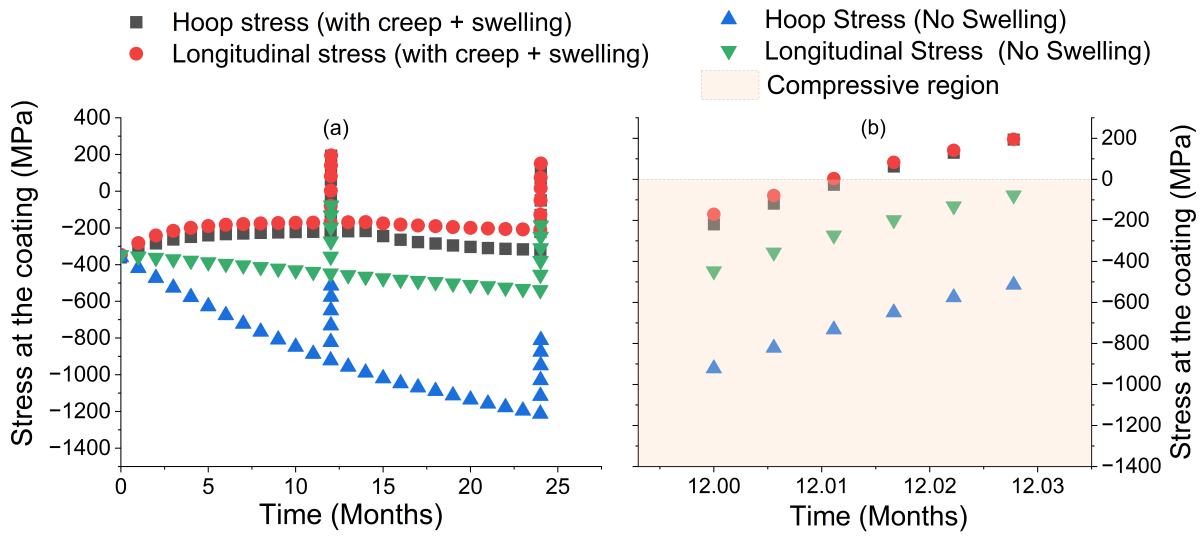

Figure 4.8: (a) Stress evolution as a function of reactor operation time (total irradiation damage of 10 dpa) in Cr coating, with or without swelling considered. P_e = 15.5 MPa for the 24-month steady-state operation with two refueling outages. P_e = 0.1 MPa and $T_{coating}$ = 76.5°C for the refueling condition. (b) Same as (a), but corresponding to the end of the first fuel cycle (12 months), enlarged to show details.

The differential stress resulting from mismatched material properties has a more pronounced effect on the coating than on the cladding. Due to the significantly lower mass of the coating, interfacial stresses have a minimal impact on the cladding's stress gradient. This condition is also illustrated in Figures 4.6 and 4.7, where the thermal and mechanical stress distributions of the coated cladding are compared to those of the bare cladding. During normal operation, the high compressive stress in the coating induces a corresponding tensile stress in the cladding near the coating–cladding interface. The opposite behavior is observed under refueling outage conditions (Figures 4.10b and d), where the tensile stress developed in the coating results in a compressive response in the adjacent cladding region. This stress-counterbalancing effect becomes more pronounced during refueling, when the overall thermo-mechanical stresses are relatively lower than those experienced during reactor operation.

Similar to all BCC metals, Cr is expected to exhibit a propensity for ductile-to-brittle transition at low temperatures, especially for low levels of common impurities, a problem that is further ex-

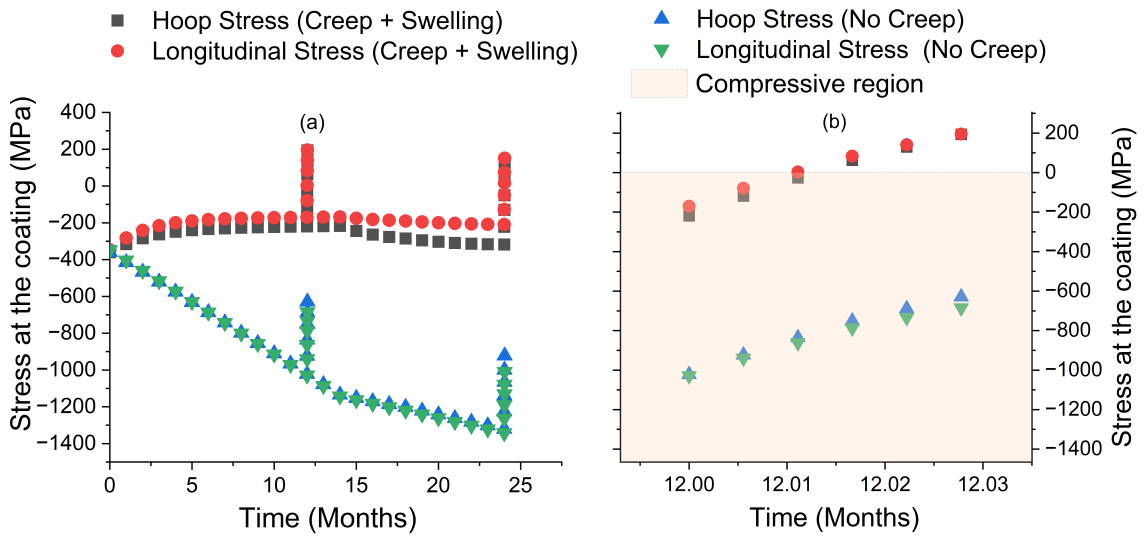

Figure 4.9: (a) Stress evolution as a function of reactor operation time (total irradiation damage of 10 dpa) in Cr coating, with or without creep considered. P_e = 15.5 MPa for the 24-month steady-state operation with two refueling outages. P_e = 0.1 MPa and $T_{coating}$ = 76.5°C for the refueling condition. (b) Same as (a), but corresponding to the end of the first fuel cycle (12 months), enlarged to show details.

acerbated by irradiation hardening/embrittlement and neutron-induced transmutation [32–34]. Although the material should withstand the tensile stresses (≈200 MPa in both hoop and longitudinal directions) during refueling, there is a risk of multiple crack formation. Furthermore, void-induced weakening at grain boundaries near the cladding interface, as well as the growth of the brittle Cr-Zn intermetallic layer [35], could increase the likelihood of debonding. Other factors, such as cyclic thermal loads and residual stresses from the coating deposition process, will also contribute to the evolution of the stress profile, potentially affecting crack formation and propagation.

While brittle fracture models for bulk BCC metals are available in the literature, they are not entirely representative of thin coatings under irradiation conditions. Even though stress limits for crack formation and propagation in Cr-coated Zircaloy tubes at low temperatures (around room temperature) were reported by Cheikh et al. [36] to be approximately 1 GPa, these results did not account for irradiation effects. Thus, potential cracking propagation or coating delamination during refueling outages should not be disregarded. A thorough risk assessment of coating failure

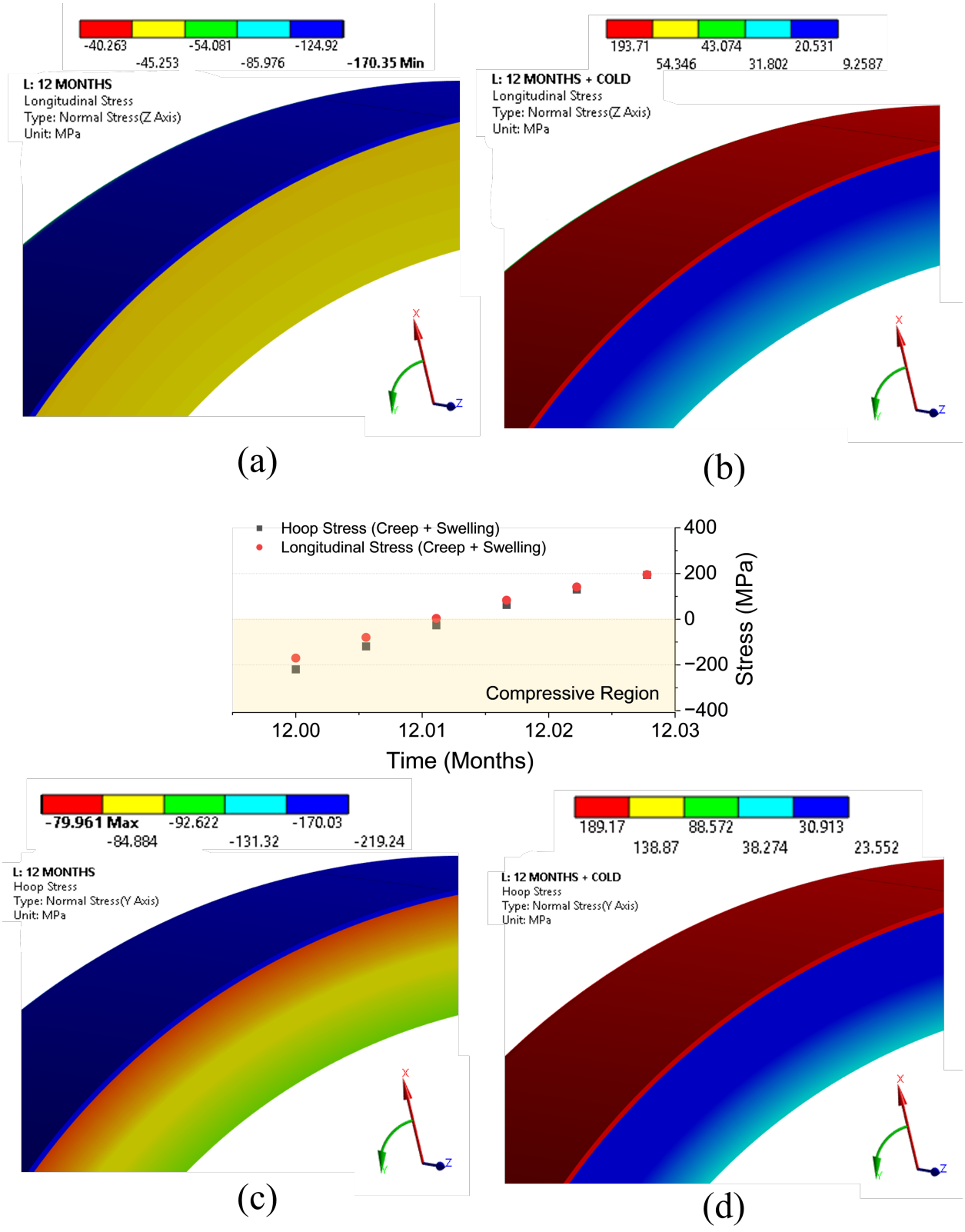

Figure 4.10: Isometric view of the in-plane, longitudinal and hoop, stress distributions in the coated cladding after (a,c) 12-month operation and (b,d) subsequent cool-down state with a graph showing associated stress levels in the coating.

should consider the combined swelling-creep effect on the coating integrity, identifying the consequences of the foregoing accumulated damage/fracture when engaging in accident conditions. This assessment should guide the design of accident-tolerant fuel cladding systems, ensuring their reliability over extended operation periods. To reduce these risks, future studies should explore the inclusion of an intermediate layer with suitable thermal, mechanical, and chemical properties to minimize stress buildup between the Cr coating and the Zircaloy substrate.

Another critical concern is the amount of creep deformation driven by the stress relaxation process. Since stress levels within the coating do not diminish to zero, creep deformation continues to accumulate throughout reactor operation. As illustrated by the orange curve in Figure 4.11, the equivalent permanent creep strain at the coating may reach up to 1.5% after 24 months. While irradiation creep occurs without introducing internal microstructural damage [15], its effects can still be detrimental for two primary reasons. First, thin coating layers typically have low strain thresholds for the onset of mechanical instabilities. Second, imperfections at the coating–substrate interface can lead to localized distortions, exacerbating stress concentrations. Both factors reduce the coating's resistance to buckling, increasing the risk of delamination during steep thermal gradients, particularly in the early stages of a loss-of-coolant accident. Given that strain accumulates over time, this issue becomes especially significant in the later fuel cycles, distinguishing it from initial cracking concerns that may emerge earlier in the cladding's service life.

4.5 Future Work

The incorporation of residual stress and Zircaloy irradiation-induced growth effects represents an important area for future development. Cold spray deposition typically produces compressive residual stresses of approximately 200 MPa in the hoop direction and 100 MPa longitudinally [37]. In contrast, physical vapor deposition (PVD) methods introduce substantially higher hoop stresses, often exceeding 400 MPa, with minimal longitudinal stress components [37, 38]. Moreover, irradiation growth in Zircaloy has been identified as a source of continuous strain mismatch in coated cladding systems [24]. Although not considered in this study, it should be included in future modeling efforts, as it imposes a sustained tensile stress on the coating. This process will reduce the

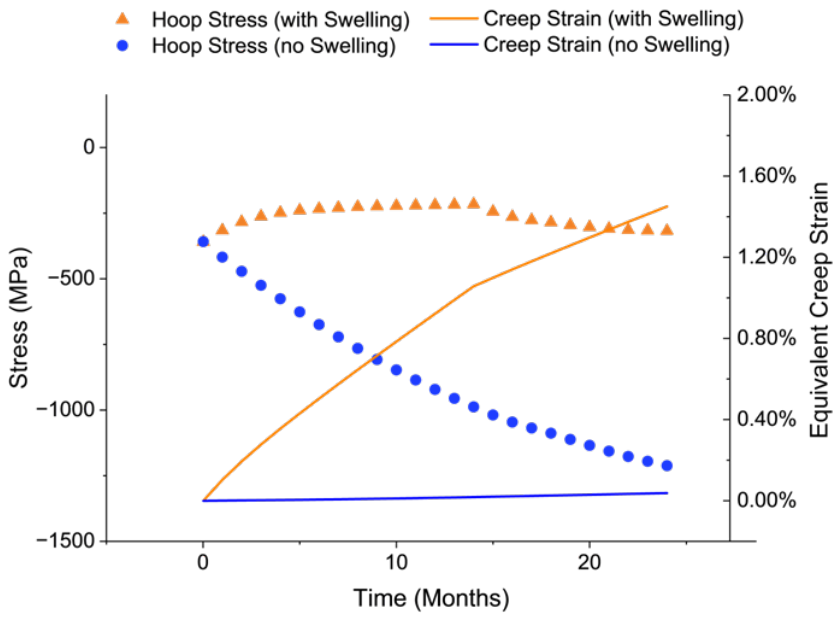

Figure 4.11: Stress and strain evolutions over 24 months of operation. The amount of potential compressive stress (blue curve) is relaxed during operation (orange curve), leading to permanent creep strain (orange data points).

stabilized compressive stress during operation, increasing the magnitude of the reversed tensile stress conditions during reactor shutdown or refueling cycles.

4.6 Conclusion

This study employed a multiscale approach by combining atomic-scale results from ion irradiation experiments to evaluate the macroscopic swelling behavior of Cr and coupled it with finite element analysis to model the stress evolution in Cr-coated fuel cladding. The modeling covers a two-year period, including two refueling shutdowns. The results highlighted the effects of irradiation-induced swelling and creep relaxation on stress evolution. Both mechanisms help reduce stress buildup during operation, which arises from the temperature and externally imposed stress gradients and the mismatch between the elastic modulus and thermal expansion coefficients of the Cr coating and Zircaloy cladding.

However, during the refueling stage at low temperatures, the permanent dimensional changes

caused by both swelling and creep lead to a significant tensile stress spike in the Cr film, especially at the interface, suggesting a potential risk of mechanical failure and/or debonding of the coating.

Additionally, significant permanent creep strains in the coating may reduce its resistance to buckling-driven fracture, presenting a critical risk that should be evaluated as a potential initial condition under large thermal gradients, such as those encountered during LOCA scenarios.

4.7 References

[1] S. J. Zinkle and L. L. Snead, "Opportunities and limitations for ion beams in radiation effects studies: Bridging critical gaps between charged particle and neutron irradiations," *Scripta Materialia*, vol. 143, pp. 154–160, 1 2018.

[2] G. S. Was, Z. Jiao, E. Getto, K. Sun, A. M. Monterrosa, S. A. Maloy, O. Anderoglu, B. H. Sencer, and M. Hackett, "Emulation of reactor irradiation damage using ion beams," *Scripta Materialia*, vol. 88, pp. 33–36, 10 2014.

[3] L. Shao, J. Gigax, D. Chen, H. Kim, F. A. Garner, J. Wang, and M. B. Toloczko, "Standardization of accelerator irradiation procedures for simulation of neutron induced damage in reactor structural materials," *Nuclear Instruments and Methods in Physics Research Section B: Beam Interactions with Materials and Atoms*, vol. 409, pp. 251–254, 10 2017.

[4] Y. Li, A. French, Z. Hu, A. Gabriel, L. R. Hawkins, F. A. Garner, and L. Shao, "A quantitative method to determine the region not influenced by injected interstitial and surface effects during void swelling in ion-irradiated metals," *Journal of Nuclear Materials*, vol. 573, p. 154140, 1 2023.

[5] E. Ryabikovskaya, A. French, A. Gabriel, H. Kim, T. Wang, K. Shirvan, F. A. Garner, and L. Shao, "Irradiation-induced swelling of pure chromium with 5 MeV Fe ions in the temperature range 450–650 °C," *Journal of Nuclear Materials*, vol. 543, p. 152585, 1 2021.

[6] A. Gabriel, L. Hawkins, A. French, Y. Li, Z. Hu, L. He, P. Xiu, M. Nastasi, F. A. Garner, and

L. Shao, “Effect of dpa rate on the temperature regime of void swelling in ion-irradiated pure chromium,” *Journal of Nuclear Materials*, vol. 561, p. 153519, 4 2022.

[7] *Ansys® Mechanical Workbench, Release 2023 R2*, ANSYS, Inc., https://www.ansys.com/.

[8] R. L. Williamson, “Enhancing the ABAQUS thermomechanics code to simulate multipellet steady and transient LWR fuel rod behavior,” *Journal of Nuclear Materials*, vol. 415, pp. 74–83, 8 2011.

[9] J. F. Ziegler, M. D. Ziegler, and J. P. Biersack, “SRIM – The stopping and range of ions in matter (2010),” *Nuclear Instruments and Methods in Physics Research Section B: Beam Interactions with Materials and Atoms*, vol. 268, pp. 1818–1823, 6 2010.

[10] A. Konobeyev, U. Fischer, Y. Korovin, and S. Simakov, “Evaluation of effective threshold displacement energies and other data required for the calculation of advanced atomic displacement cross-sections,” *Nuclear Energy and Technology*, vol. 3, pp. 169–175, 9 2017.

[11] J. G. Gigax, H. Kim, E. Aydogan, F. A. Garner, S. Maloy, and L. Shao, “Beam-contamination-induced compositional alteration and its neutron-atypical consequences in ion simulation of neutron-induced void swelling,” *Materials Research Letters*, vol. 5, pp. 478–485, 11 2017.

[12] J. G. Gigax, E. Aydogan, T. Chen, D. Chen, L. Shao, Y. Wu, W. Y. Lo, Y. Yang, and F. A. Garner, “The influence of ion beam rastering on the swelling of self-ion irradiated pure iron at 450 °C,” *Journal of Nuclear Materials*, vol. 465, pp. 343–348, 10 2015.

[13] C. A. Schneider, W. S. Rasband, and K. W. Eliceiri, “NIH Image to ImageJ: 25 years of image analysis,” *Nature Methods*, vol. 9, pp. 671–675, 2012. [Online]. Available: https://doi.org/10.1038/nmeth.2089

[14] Y. Lee and M. S. Kazimi, “A structural model for multi-layered ceramic cylinders and its application to silicon carbide cladding of light water reactor fuel,” *Journal of Nuclear Materials*, vol. 458, pp. 87–105, 3 2015.

[15] F. A. Garner, "Radiation-induced damage in austenitic structural steels used in nuclear reactors," *Comprehensive Nuclear Materials: Second Edition*, pp. 57–168, 1 2020.

[16] M. Zahoor, "Modeling primary creep for Zircaloy claddings during load reversals and drops in BISON," *Journal of Nuclear Materials*, vol. 511, pp. 212–219, 12 2018.

[17] R. Adamson, M. Griffiths, and C. Patterson, "Irradiation growth of zirconium alloys a review," 12 2017. [Online]. Available: https://www.antinternational.com/docs/samples/FM/04/ZIRAT22-IZNA17_Irradiation_Growth_of_Zirconium_Alloys_Sample.pdf

[18] F. Garzarolli, R. Adamson, and K. Coleman, "Microstructure of zirconium alloys and effects on performance," Advanced Nuclear Technology International, Tech. Rep., 11 2015. [Online]. Available: https://www.antinternational.com/docs/samples/FM/09/ZIRAT20_IZNA15_STR_Microstructure_sample.pdf

[19] K. J. Geelhood, L. Kyriazidis, J. Corson, W. G. Luscher, and C. E. Goodson, "Matlib-1.0: Nuclear material properties library," Pacific Northwest National Laboratory, Tech. Rep., 4 2021. [Online]. Available: https://www.nrc.gov/docs/ML2009/ML20099A090.pdf

[20] E. B. Schwenk, K. R. Wheeler, G. D. Shearer, and R. T. Webster, "Poisson's ratio in zircaloy-4 between 24° and 316°C," *Journal of Nuclear Materials*, vol. 73, pp. 129–131, 4 1978.

[21] U. Holzwarth and H. Stamm, "Mechanical and thermomechanical properties of commercially pure chromium and chromium alloys," *Journal of Nuclear Materials*, vol. 300, pp. 161–177, 2 2002.

[22] P. E. Armstrong and H. L. Brown, "Dynamic Young's modulus measurements above 1000 ºC on some pure polycrystalline metals and commercial graphites," *Trans. AIME*, vol. Vol: 230, 8 1964. [Online]. Available: https://www.osti.gov/biblio/4018502

[23] N. A. Dubrovinskaia, L. S. Dubrovinsky, S. K. Saxena, and B. Sundman, "Thermal expansion of Chromium (Cr) to melting temperature," *Calphad*, vol. 21, pp. 497–508, 12 1997.

[24] Y. Lee, J. I. Lee, and H. C. NO, "Mechanical analysis of surface-coated zircaloy cladding," *Nuclear Engineering and Technology*, vol. 49, pp. 1031–1043, 8 2017.

[25] J. Risner and A. Alpan, "Reactor Pressure Vessel Fluence, DPA, and Uncertainty Quantification in Extended Beltline Locations (TLR-RES/DE/CIB-2021-09)," 4 2021. [Online]. Available: https://www.nrc.gov/docs/ML2113/ML21137A310.pdf

[26] I. Pioro and R. Duffey, "Current and future nuclear power reactors and plants," *Managing Global Warming: An Interface of Technology and Human Issues*, pp. 117–197, 1 2019.

[27] M. D. Isnaini and M. Subekti, "Heat removal analysis in the AP1000 reactor's refueling process," *Journal of Physics: Conference Series*, vol. 1198, p. 022066, 4 2019.

[28] M. S. El-Genk, B. Su, and Z. Guo, "Experimental studies of forced, combined and natural convection of water in vertical nine-rod bundles with a square lattice," *International Journal of Heat and Mass Transfer*, vol. 36, pp. 2359–2374, 1 1993.

[29] International Atomic Energy Agency, "Development of radiation resistant reactor core structural materials, Annex VII, Nuclear Technology Review (IAEA/NTR)," p. 141, 8 2007. [Online]. Available: http://inis.iaea.org/search/search.aspx?orig_q=RN:43028599

[30] L. K. Mansur, "Correlation of neutron and heavy-ion damage: II. The predicted temperature shift if swelling with changes in radiation dose rate," *Journal of Nuclear Materials*, vol. 78, pp. 156–160, 11 1978.

[31] A. R. Shugurov and A. V. Panin, "Mechanisms of stress generation and relaxation," *AIP Conf. Proc.*, vol. 1623, pp. 575–578, 2014.

[32] C. L. Briant, K. S. Kumar, N. Rosenberg, and H. Tomioka, "The mechanical properties of high purity chromium," *International Journal of Refractory Metals and Hard Materials*, vol. 18, pp. 9–11, 1 2000.

[33] Y. F. Gu, H. Harada, and Y. Ro, "Chromium and chromium-based alloys: Problems and possibilities for high-temperature service," *JOM*, vol. 56, pp. 28–33, 2004. [Online]. Available: https://doi.org/10.1007/s11837-004-0197-0

[34] M. Rajput and R. Srinivasan, "Study of transmutation, gas production, and displacement damage in chromium for fusion neutron spectrum," *Annals of Nuclear Energy*, vol. 138, p. 107187, 4 2020.

[35] J. Yang, M. Steinbrück, C. Tang, M. Große, J. Liu, J. Zhang, D. Yun, and S. Wang, "Review on chromium coated zirconium alloy accident tolerant fuel cladding," *Journal of Alloys and Compounds*, vol. 895, p. 162450, 2 2022.

[36] I. B. Cheikh, G. Parry, D. Dalmas, R. Estevez, and J. Marthelot, "Analysis of the multi-cracking mechanism of brittle thin films on elastic-plastic substrates," *International Journal of Solids and Structures*, vol. 180-181, pp. 176–188, 12 2019.

[37] T. Graening, M. Ridley, J. Werden, K. Linton, and N. Capps, "Residual stress measurements of cr-coated cladding," Oak Ridge National Laboratory, Oak Ridge, TN, Tech. Rep. ORNL/SPR-2024/3218, January 2024, prepared for the U.S. Department of Energy. [Online]. Available: https://info.ornl.gov/sites/publications/Files/Pub208608.pdf

[38] J. Ribis, A. Wu, R. Guillou, J.-C. Brachet, C. Baumier, A. Gentils, and M. Loyer-Prost, "Radiation-induced sharpening in cr-coated zirconium alloy," *Materials*, vol. 15, 2022. [Online]. Available: https://www.mdpi.com/1996-1944/15/6/2322

5. CONCLUSION

One of the main concerns for licensing Cr-coated claddings lies in the limited understanding of irradiation effects, particularly how radiation damage may affect the coating-cladding system under operational and off-normal conditions. As discussed in Chapter 2, our project sought to address this gap by highlighting safety-relevant degradation mechanisms, with special emphasis on the role of ion irradiation in accelerating the qualification process for this promising ATF technology.

Understanding swelling behavior under irradiation is key to that goal. In Chapter 3, we demonstrated the effectiveness of ion irradiation as a tool to emulate neutron damage, systematically assess void swelling in pure Cr, and provide fast and reliable data to support material evaluation. Importantly, we observed the expected Cr's low incubation period and identified an atypical low steady-state swelling rate near 0.05%/dpa.

In Chapter 4, these experimental insights were incorporated into a finite element model that simulates PWR conditions and captures stress evolution in the coated-cladding system. The results raised two key issues: (1) the risk of cracking during refueling, when tensile stress spikes may act in combination with radiation-induced embrittlement; and (2) a progressive reduction in buckling resistance due to accumulated creep strain and geometric deformation in the thin coating layer.

Altogether, this thesis reinforces the need to consider swelling and irradiation creep when evaluating coated cladding performance. These effects may require revisiting traditional safety limits, such as strain, ballooning, and embrittlement thresholds, for licensing applications. They should also be incorporated into computational tools and qualification tests, whether through model-based analysis or irradiation of pre-irradiated samples.